The International Journal of Advanced Manufacturing Technology (2024) 131:999–1038
https://doi.org/10.1007/s00170-024-13126-5

CRITICAL REVIEW

Directed energy deposition + mechanical interlayer deformation additive manufacturing: a state-of-the-art literature review

Francisco Werley Cipriano Farias[1] · **Telmo Jorge Gomes dos Santos**[1,2] · **João Pedro Oliveira**[1,3]

Received: 20 October 2023 / Accepted: 23 January 2024 / Published online: 5 February 2024

Abstract

Directed energy deposition (DED) additive manufacturing systems have been developed and optimized for typical engineering materials and operational requirements. However, parts fabricated via DED often demonstrate a diminished material response, encompassing inferior mechanical properties and heat treatment outcomes compared to traditionally manufactured components (e.g., wrought and cast materials). As a result, parts produced by DED fail to meet stringent specifications and industry requirements, such as those in the nuclear, oil and gas, and aeronautics sectors, potentially limiting the industrial scalability of DED processes. To address these challenges, systems integrating DED with interlayer (cold or hot) mechanical deformation (e.g., rolling and hammering/peening, forging) have been developed. These systems refine the microstructure, mitigate the typical crystallographic texture through static and/or dynamic recrystallization, and enhance mechanical properties and heat treatment responses without altering material specifications. In this regard, the present state-of-the-art review reports the DED + interlayer mechanical deformation systems and their variants, and their potential and limitations, providing a critical analysis to support the development and adaptation of this technology to overcome the process and material limitations that currently prevent the large-scale industrial adoption of DED processes. Furthermore, a detailed description of the grain size refinement mechanisms induced by interlayer mechanical deformation and their respective effects on the mechanical properties of commonly used 3D-printed engineering alloys (e.g., Ti-6Al-4V, Inconel 718, various low-alloy steels, AISI 316L stainless steel, and Al-based series 2xxx) is comprehensively analyzed.

Keywords Additive manufacturing · Directed energy deposition · Mechanical properties · Grain size refinement · Hybrid deposition

1 Introduction

Additive manufacturing (AM), a layer-by-layer deposition process, increases design flexibility [1], reduces lead time and material waste (low buy-to-fly and topological optimization) [2], and enables the development of new components (e.g., one-piece parts and functionally graded materials) [3, 4]. It has been considered a promising technology in industry 4.0. The ASTM F3187–16 classifies the AM directed energy deposition (DED) processes according to the heat source (laser, electron beam, or arc plasma) used to melt and consolidate the feedstock material (powder and wire). Focused heat source (laser and electron beam) DED processes use a lower heat input and have a higher dimensional control [5]. However, the commonly used powder feedstock material is difficult to handle, causing high material wastage [6, 7], and is susceptible to defects (e.g., porous and lack of fusion) [8]. DED-arc processes use the arc plasma of typical welding processes as the heat source (i.e., gas tungsten arc (GTA), plasma transferred arc (PTA), and gas metal arc (GMA) welding), which significantly reduces the equipment and feedstock material costs (e.g., commercial wire spools) [1]. Besides, DED-arc processes have the highest deposition rate (2–10 kg/h), albeit at the expense of diminished dimensional accuracy and resolution [9].

✉ Francisco Werley Cipriano Farias
fw.farias@campus.fct.unl.pt

[1] UNIDEMI, Department of Mechanical and Industrial Engineering, NOVA School of Science and Technology, NOVA University of Lisbon, 2829-516 Caparica, Portugal

[2] Laboratório Associado de Sistemas Inteligentes, LASI, 4800-058 Guimarães, Portugal

[3] CENIMAT/I3N, Department of Materials Science, NOVA School of Science and Technology, Universidade NOVA de Lisboa, 2829-516 Caparica, Portugal

Despite the advantages of the DED processes in relation to the traditional (e.g., machining from a billet) manufacturing routes (e.g., lower lead time and supplier chain decentralization), the material properties and behavior of directed energy deposited (DEDed) parts have still not been optimized [10, 11], which can prevent their industrial scalability. Additionally, DEDed parts often do not meet the specifications and standards of the traditionally manufactured parts (e.g., wrought + machining) [12]. Furthermore, the higher residual stress developed necessitates post-deposition heat treatments [13], which are applicable even for non-heat-treatable alloys. The complex and multiple thermal cycles and non-equilibrium solidification conditions, combined with the higher heat input (e.g., DED-arc processes) or localized heat source (e.g., DED-laser), explain the relatively high residual stresses and distortions reported [14]. In addition, the epitaxial grain growth during the melting pool solidification usually generates a coarser and highly oriented microstructure, which results in anisotropic properties and inferior part performance [15–18].

To overcome the aforementioned material challenges, (cold or hot) plastic deformation, coupled with the feedstock material consolidation, has proven to be a promising alternative for controlling the microstructure, residual stresses, and mechanical properties of the DEDed parts [19–21]. Deposition + interlayer mechanical deformation (e.g., vibration, rolling, and hammer peening) was first applied in arc-welding [22] to relieve residual stresses and improve the fatigue life of the welded joints. However, due to the geometric aspects associated with additive manufacturing, DED processes face specific challenges, such as unrestricted deformation (i.e., absence of welding bevel groove), higher residual stresses, and complex path planning. In addition, commercial alloys (e.g., Ti- [23], Al- [24], Fe- [25], and Ni-based alloys [26]) exhibit good formability in the as-built (as-printed) condition [27], reinforcing the use of interlayer deformation during fusion-based additive manufacturing processes [28–30]. To the best of the authors' knowledge, Colegrove et al. [31] and Zhang et al. [32], in 2013, were the first groups to study the DED + interlayer deformation processes, which triggered the interest of the AM community and the subsequent technological development. Figure 1 details the evolution of peer-reviewed papers per year on the topic of DED + interlayer mechanical deformation.

Given the potential industrial scalability and advantages of the DED processes in relation to traditional manufacturing routes, the challenges related to performance of DEDed parts (e.g., inability to meet material standards and anisotropy), and the current interest in DED processes coupled with interlayer (cold or hot) mechanical deformation to overcome the abovementioned material limitations, the present work performed a comprehensive state-of-the-art review of the DED + interlayer mechanical deformation technologies

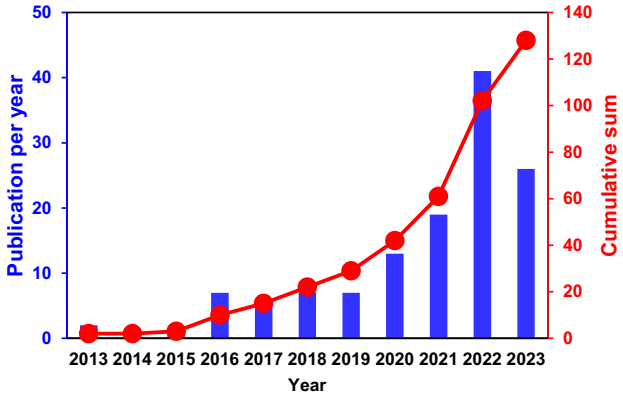

Fig. 1 Evolution of peer-reviewed papers on DED + deformation over time

(mechanical systems, advantages, and limitations), their grain size refinement mechanisms, and their effects on the quasi-static mechanical properties of common engineering alloys (e.g., Ti-6Al-4V, Inconel 718, high-strength low-alloy steels, AISI 316L stainless steel, and 2xxx series aluminum alloy).

1.1 Why deform the deposited layers?

Due to the almost unidirectional heat flux in AM processes [33], the remelting of the previously deposited layer (or substrate) [34], and the higher thermal gradient in the melting pool [35], epitaxial nucleation, and growth are promoted instead of heterogeneous nucleation. This results in coarse (millimeter sized) columnar grains with a preferential crystallography orientation (typically the cube texture, $\{100\}<100>$) [36], which can cause anisotropic properties [37] and lower fatigue resistance [38]. In addition, the numerous thermal cycles with steep thermal gradients can generate high residual stresses and subsequent distortions in the as-built part [39]. Solutions have been proposed to promote the columnar-to-equiaxed transition (CET) during solidification and generate a finer and non-oriented microstructure [40], such as the addition of inoculants [41–43], modification of alloy composition [44, 45], control of thermal cycles (thermal management) [46, 47], and vibration of the melting pool [48, 49].

The use of inoculants, as well as the modification of the feedstock material composition, can alter the material specifications (critical for high-responsibility applications, e.g., nuclear, oil and gas, and aeronautics industries), requiring several and costly tests (e.g., corrosion in operational environments, creep, wear, and fatigue) for feedstock material requalification and commercial adoption. Thermal management via an external cooling system (e.g., submersion in water and air jet) had limitations regarding parts size and

geometry, low heat transfer efficiency, and it was almost restricted to wire-based DED (laser and arc plasma) processes, because the use of powder is incompatible with water or air currents [50]. Further, external cooling systems tend to be less effective in inducing the CET because their effect on the thermal condition at the melting pool (solidification rate and thermal gradient) is approximately negligible [33]. Besides, for reactive materials (e.g., Al and Ti-based alloys), and specific feedstock material/coolant conditions, a surface reaction can occur, forming scales and increasing the minor harmful element content in as-built alloys (e.g., H, O, C, or N). The main advantage of thermal management via an external cooling system is the lesser idle time and higher productivity in low-scale production. By contrast, for mass part production, the external cooling system becomes redundant because the 3D printer can continue to fabricate other parts while the just deposited one cools to the specified interlayer temperature.

Vibration-assisted deposition has been shown to be an interesting alternative to induce CET without altering the material composition and affecting the deposition process (final layer geometry and process stability constant) [51, 52], exhibiting intense grain size refinement. However, vibration is limited by the part geometry and size (wave attenuation) and alloy type [53, 54]. In addition, a vibration stress relief procedure was initially used for welded joints that could not be post-weld heat treated [55]. Using arc-based welding, Munsi et al. [56] and Hsieh et al. [57] highlighted that vibration-assisted welding synergistically induced a finer microstructure and reduced the residual stress levels. However, in additive manufacturing, similar studies related to vibration-assisted deposition have focused only on the microstructure namely grain size, grain morphology, and texture [58, 59], and the effect of vibration on the residual stress and distortions has not been addressed. It is worth mentioning that vibration-assisted welding stress relief had no significant effect on the maximum developed residual stresses and did not significantly alter the residual stress profile [55, 56, 60]. Thus, considering the higher residual stresses developed in the parts fabricated via AM and their coarse and oriented microstructure, there is a technological demand for DED process variants and/or hybrid processes that simultaneously refine the microstructure and relieve residual stresses. This can minimize the material waste and machining time (near-net-shape primary part with minimal distortion) and reduce the number of manufacturing steps.

The application of interlayer mechanical deformation during deposition evolved into a promising technology to overcome the challenges associated with DED processes, including the coarse and oriented microstructure, lower mechanical properties, and the requirement of residual stress relief heat treatments. Multiple deformation-thermal cycle processes (e.g., forging and/or controlled rolling + heat treatment) can transform the microstructure of a billet (casting material with columnar grain morphology, such as materials fabricated via DED) into an equiaxial grain morphology via multiple cycles of dynamic/static recrystallization and reheating [61–64]. Thus, applying a similar principle to AM processes, the cold or hot deformation between the deposited layers can induce grain size refinement and alter the phase transformation kinetics [31], as well as relieve the residual stress via local yielding [65]. However, the fast DED thermal cycles in relation to conventional controlled rolling and the complex part geometry limit the use of non-adaptable routes (e.g., forging and rolling), requiring the development of dedicated DED + interlayer deformation systems. Typically, these are composed of a deposition unit (heat source and feeding system) and a deformation tool that can work at high (hot deformation to induce dynamic recrystallization) or at low temperatures (cold deformation to induce static recrystallization during reheating thermal cycle or heat treatment).

2 Deposition + interlayer deformation—systems and process aspects

2.1 Rolling

The use of cold or hot rolling coupled with deposition originated from arc-based welding processes, as demonstrated by Adams et al. [66] and Coules et al. [67], and was used to improve the mechanical properties and relieve residual stress. In addition, the rolling process can alter the bead geometry and morphology (e.g., flattening the weld bead surface). The development of DED + interlayer rolling, especially cold deformation, began at the Cranfield University WAAM® group [31].

Deposition + cold interlayer rolling systems (Fig. 2) are composed of two major components: a rigid moving system that supports a hydraulic pressure roller and a deposition system (welding torch + wire feeding and accessories). It is worth noting that the deposition system can use different welding processes (e.g., GMA and GTA), while the roller can have multiple profiles (flat and inverted, as detailed in Fig. 2c). In addition, due to the high material strength at low temperatures (< 200 °C), high rolling forces are used (up to 160 kN) [68], which requires the use of robust and rigid structures, such as hydraulic systems. The main disadvantage of this interlayer rolling system architecture is its low versatility, which limits the part geometry and path planning. For example, the roller is restricted to approximately linear path planning (e.g., back and forth), differing from the deposition system (welding machine coupled to a robot arm or CNC machine), which allows an almost free path planning. Thus, the roller limits the deposition path planning flexibility and deposition strategies of the DED systems [69, 70].

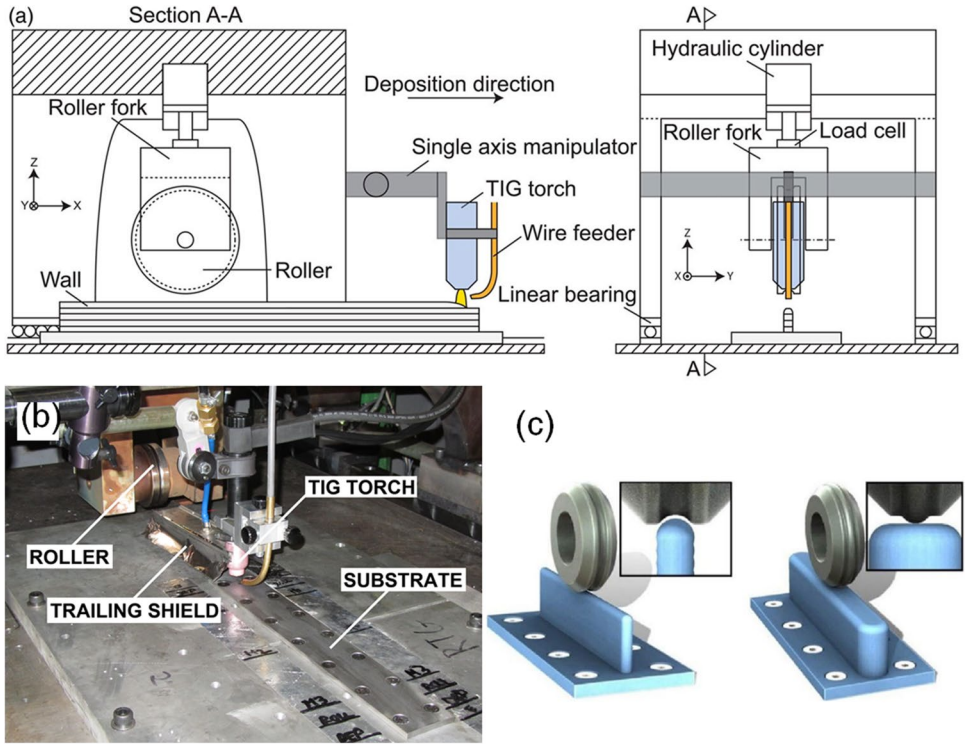

Fig. 2 Rolling + deposition experimental setup: **a** schematic representation, **b** real image, and **c** different roller profiles (adapted from [70, 169, 189])

Despite the abovementioned limitations, Hönnige et al. [71, 72] developed the side cold rolling technique, which applies a side surface rolling using a rigid support block. Figure 3 details the influence of the rolling force and rolling direction on the macroscopic aspect of the wall. Figure 3a–d demonstrates that when the rolling is applied in the top layer surface, a flat top layer is generated, followed by an increase on the layer width (volume conservation). Conversely, when rolling is applied to the side of the deposited part (Fig. 3e–h), a reduction in the part waviness and layer width is observed. Additionally, an increase in the rolling load results in greater deformation. Williams et al. [1] reported that the waviness of the DEDed-arc part surface limits its use in the as-built condition for structural applications due to the geometric stress concentration (i.e., reducing the fatigue resistance), requiring a post-deposition surface machine. Thus, as interlayer rolling reduces the waviness (Fig. 3), the machining time and tool-life can be improved [9, 73]. Also, according to Dirisu et al. [68], the interlayer cold rolling promoted residual stress relief, refined the microstructure, and enhanced fatigue resistance.

Gu et al. [74] reported that cold rolling also closed porosity during the deposition of aluminum alloys. The authors [74] showed that pore closure increased with the imposed rolling load. Figure 4 illustrates the inner morphologies of the flattened pores. In addition, the fraction of the smaller pores (radius lower than 2 mm) was reduced after rolling. However, pores with diameters greater than 5 mm and those located deeper in the solidified material, close to the fusion line, could only be closed with significantly higher rolling forces, resulting in considerable layer deformation. Additionally, as reported by Bercelli et al. [75], the presence of pores can drastically reduce the fatigue life of parts fabricated by DED-arc; these results were corroborated by Dirisu et al. [68], which observed that the fatigue life of the low-alloyed steel (AWS ER70S-6) fabricated via DED-arc + interlayer cold rolling increased with the interlayer rolling load, i.e., a higher rolling load reduces the pore volume, which increases the fatigue life.

Despite the effective grain size refinement and residual stress relief effects, the large equipment dimensions and limited path planning flexibility limited the interlayer cold rolling. In this context, other systems were developed, which considered the in situ deformation, i.e., immediately followed the feedstock material consolidation with the material still incandescent (i.e., hot deformation). Deforming the material at relatively elevated temperatures enables the use of lower rolling loads, simpler and less expensive systems, and increases process adaptability. However, other process challenges arise, such as the accurate rolling temperature control (distance between the heat source and the deformation tool), depth of recrystallized zone (ideally deeper than the penetration of subsequent layer), and the preservation of a flat and smooth layer surface.

Zhang et al. [32] developed a DED-arc + interlayer hot rolling system (Fig. 5a), which consisted of a heat source (GMAW) and a micro-roller coupled with a hydraulic cylinder, both fixed and connected to a three-axis computer

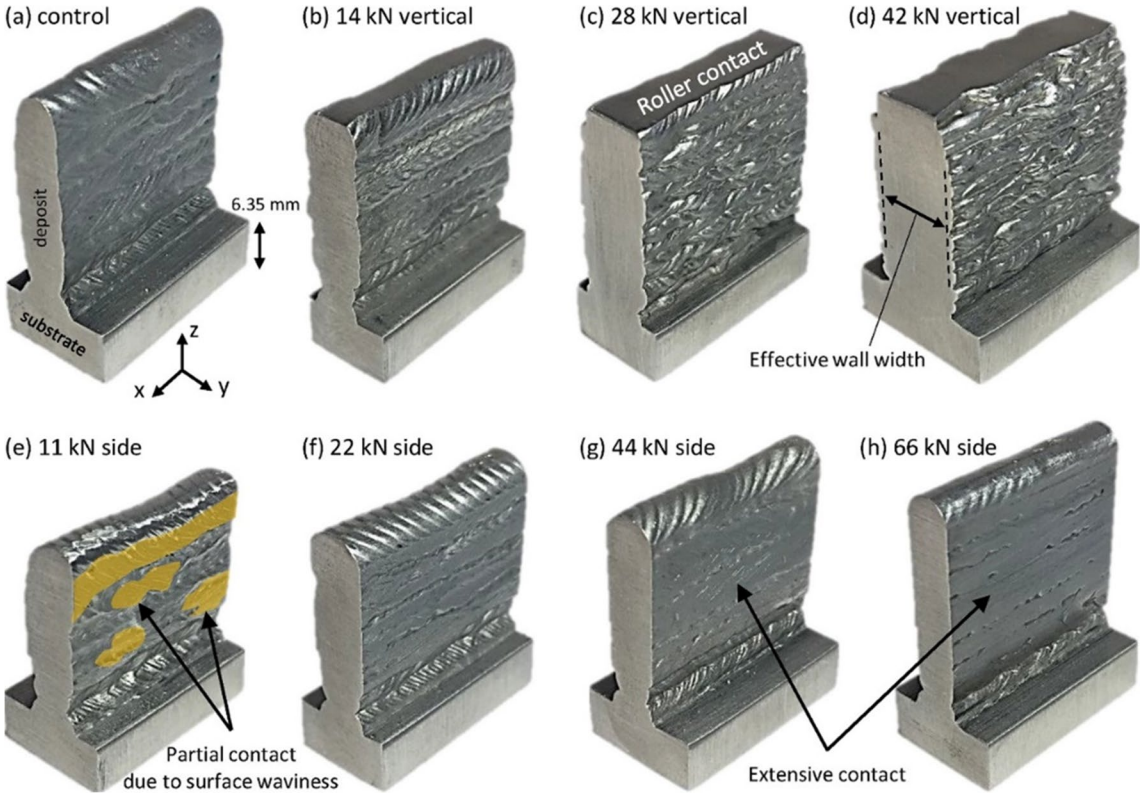

Fig. 3 Effect of rolling on part superficial aspect: **a** control sample, **b**–**d** vertical rolled, and **e**–**h** side rolled specimens (from [72])

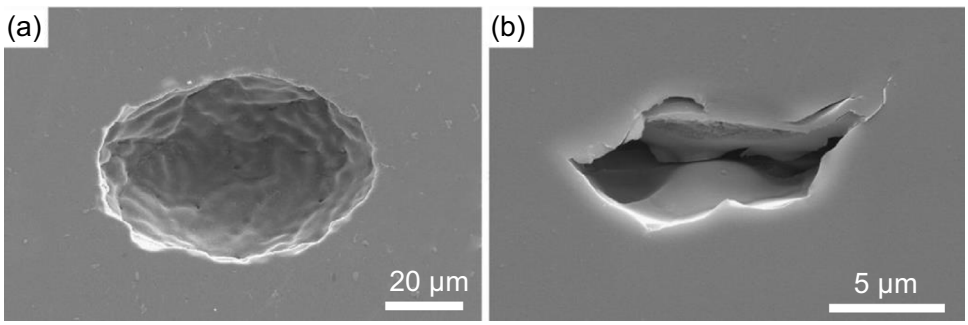

Fig. 4 Effect of rolling load on pore morphology: **a** 15 kN and **b** 30 kN (adapted from [74])

numerical control (CNC) machine. Therefore, deposition and subsequent deformation can follow the same path for simple curves trajectories (Fig. 5b) and ensuring a flat top surface. In addition, Zhang et al. [32] detailed the effects of the distance of the roller to the heat source (i.e., rolling temperature) on the final surface aspect (Fig. 6). For short distances (Fig. 6a), deformation occurs in or near the mushy zone (solid + liquid coexist), which can lead to material adherence (viscoplastic behavior) and potential fracture (elevated temperature ductility loss) at higher temperatures resulting in a poorer surface quality. By contrast, for longer distances (Fig. 6c), the total deformation may be insufficient due to the high cooling rate (the just consolidated material strengthens as the temperature drops) and lower hot rolling loads (~ 3 kN). Hence, achieving precise process optimization becomes imperative. This must consider each material/deposition parameter pair, as well as the precise adjustment of the distance between the heat source and deformation tool to effectively refine the microstructure [76].

Although the system developed by Zhang et al. [32] (Fig. 5) provided good results, the control of layer width throughout the printed part was not guaranteed by the interlayer hot rolling because the thermal conditions (e.g., heat accumulation and interlayer temperature [33]) changed during deposition. Xie et al. [77] improved the layer geometrical accuracy using a metamorphic rolling mechanism (Fig. 7),

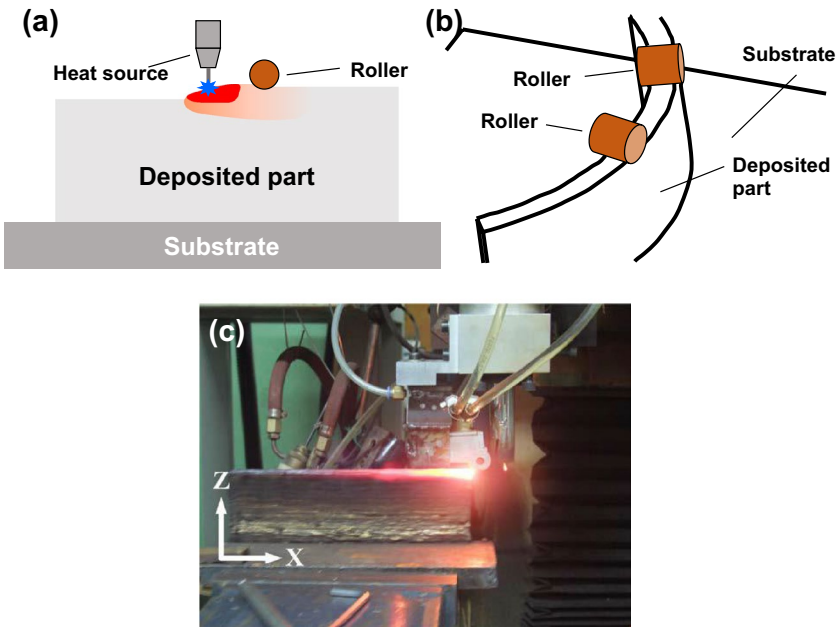

Fig. 5 **a** Deposition + interlayer hot rolling system, **b** similar path planning for both roller and heat source, and **c** system in operation (adapted from [32])

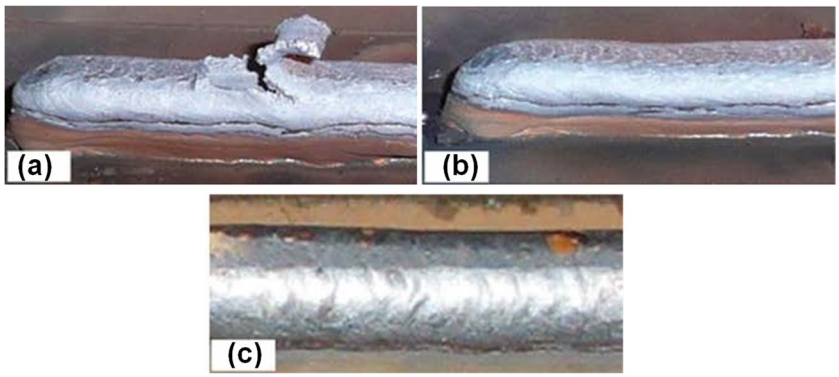

Fig. 6 Final surface aspect for different roller-heat source distances: **a** low, **b** appropriate, and **c** high (adapted from [32])

which consists of a system that is similar to that of Zhang et al. [32] (Fig. 6) with the addition of two exchangeable side rollers. These side rollers improve the layer geometrical accuracy for multi-layer single-bead and/or multi-bead DEDed parts. In addition, Xie et al. [77] reported that the absolute error in layer height remained constant during deposition, allowing an automatic correction of the contact-tip-to-work distance. Other authors [78–82] also developed deposition + interlayer hot rolling systems; however, the main idea and mechanism were similar to that originally proposed by Zhang et al. [32].

Zhao et al. [83] modeled the bead overlapping for Zhang et al. [32] system (Fig. 5) using the bead-on-plate geometric fitting (sine function bead approximation) [84] and flat-top overlapping models [85]. The results showed that the best overlapping had a second-order polynomial correlation with the rolling deformation. For a deformation of 36.6% (layer height reduction), the optimized overlap is 74.24%. This value aligns closely with the multi-bead tangent overlapping model (73.8%) proposed by Ding et al. [86]. In addition, Zhao et al. [83] demonstrated that the bead overlapping performance, specifically its susceptibility to lack of fusion, remained unchanged even after layer surface flattening through interlayer hot rolling, corroborating the observation made by Xie et al. [77] regarding the ability of interlayer hot rolling [32] to print thick-sectioned parts (Fig. 5).

The abovementioned deposition + interlayer (hot or cold) rolling systems used arc plasma as a heat source (i.e., typical welding machines). Li et al. [87] and Tain et al. [88] developed a deposition + hot rolling system (Fig. 8) using a laser and powder as the heat source and feedstock material (i.e., DED-laser), respectively. As opposed to the arc plasma-DED + interlayer rolling systems, in the systems proposed by Li et al. [87] and Tain et al. [88], the moving part was the substrate whose movement was controlled by three step motors (x, y, and z directions). The strain and strain rate were controlled via the z-axis movement (built direction) and the moving speed of the substrate, respectively. For

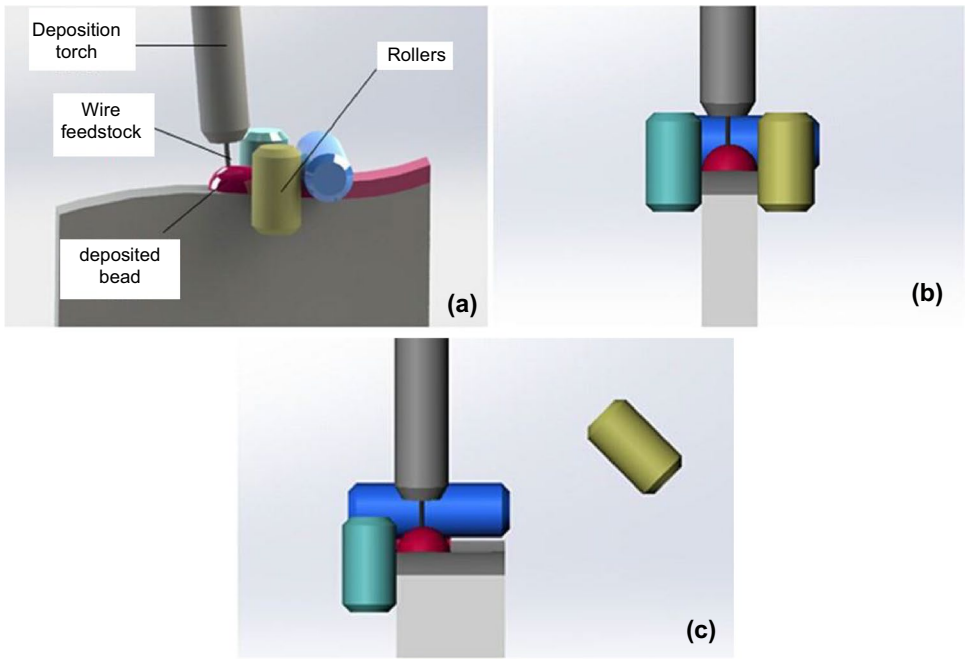

Fig. 7 **a** Schematic diagram of the metamorphic rolling mechanism, **b** deposition of the multi-layer single-bead (thin wall), and **c** metamorphic rolling mechanism applied to multi-layer multi-bead part deposition (adapted from [77])

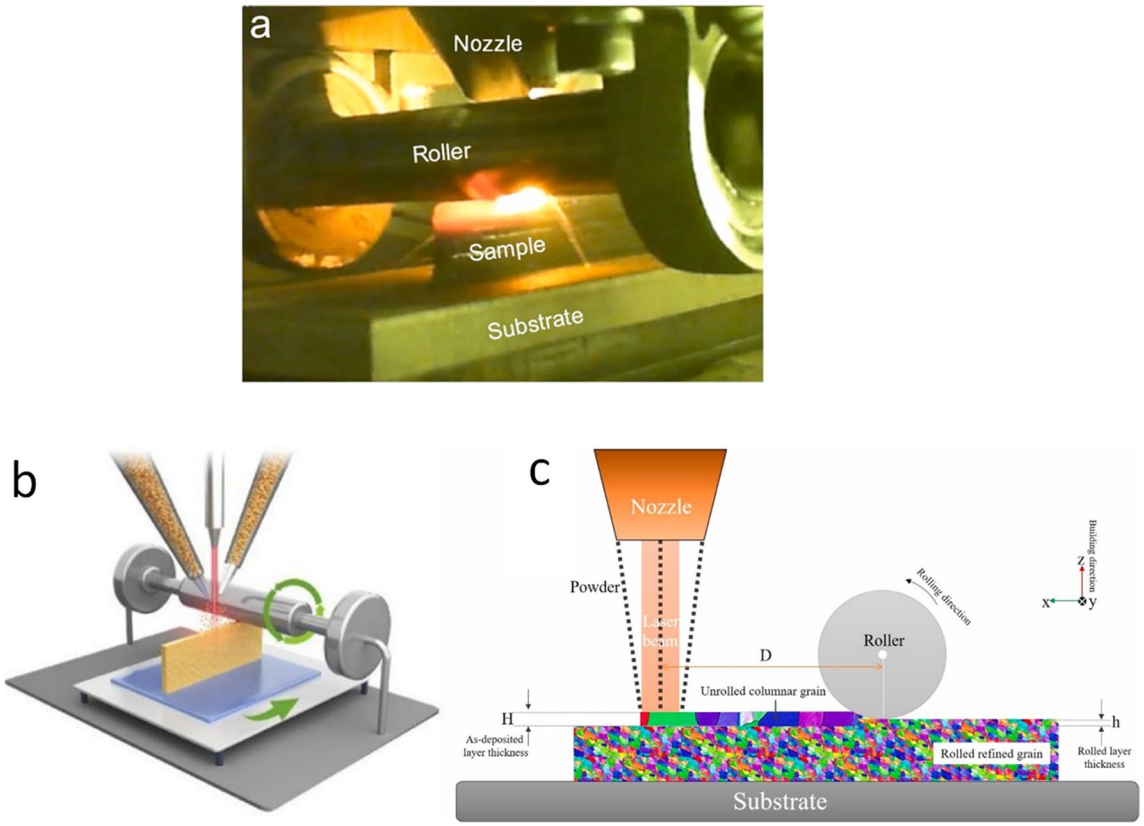

Fig. 8 **a** DED-laser + interlayer hot rolling, **b**, **c** schematic illustration (from [87, 88])

the deposition of Ti-6Al-4V alloy and Ni-based superalloy 718, the load cells registered a rolling load of 1.3 and 3 kN, respectively, which are significantly smaller than the rolling loads used during cold rolling (up to 160 kN) [31, 69, 89, 90] and similar to that reported by Kan et al. [91] and Zhang et al. [32] (Fig. 5). These rolling loads are even considerably

lower than warm (~450 °C) rolling (50 kN) [92], which reinforces the importance of a precise temperature (distance between the heat source and deformation tool) control.

Finally, both cold and hot interlayer rolling systems exhibited limitations in path planning, as the rolling system cannot rapidly alter the direction, thus constraining deposition freedom. However, due to its smaller equipment and lower rolling load, the interlayer hot rolling system could follow the heat source path along smooth curved trajectories (high radii of curvature). Conversely, the uncoupled characteristics of cold rolling system, where the heat source and deformation parameters are independent, did not restrict the process window, allowing an improved layer aspect (e.g., width and height) control. For instance, during part thickness transition, the deposition parameters can be adjusted without constraints. The precise control of the heat source-deformation tool distance in the interlayer hot rolling system restricts the deposition parameter window [93], making it difficult to control the geometric aspects of the layer during deposition. Thus, cold rolling had better deposition parameter control and limited path planning (almost restricted to linear deposition); by contrast, hot rolling showed more freedom in path planning and restrictive and difficult-to-control deposition parameters.

2.2 Hammering, peening, and forging

Similar to rolling, peening/hammering/forging coupled with deposition also originated from arc-based welding [94–96]. In addition, to the best of the authors' knowledge, the Cranfield University WAAM group pioneered the coupling cold peening/hammering with DED-arc. This innovation arose from the limitations of the aforementioned cold rolling system, specifically the heavy equipment and design constraints (Fig. 2). Hönnige et al. [97, 98] developed a DED-arc + interlayer cold hammer peening variant to reduce residual stresses through surface compression plastic deformation, a mechanism previously described by Kobayashi et al. [99]. Hammer peening works with the tool (hammer) mounted on a robot or CNC machine using a moderate pin oscillation frequency (~200 Hz), enhancing the flexibility of the process in relation to rolling. Figure 9 illustrates the equipment and the possibility of their use in distinct positions (vertical, horizontal, and inclined) with complex path planning. This tool was operated using an electromagnetic plunger coil (pneumatic system), delivering an impact energy of 750 mJ, thereby ensuring deep deformation zones [100]. Fang et al. [101] noted that coupling a pneumatic hammer with DED-arc can minimize porosity and alter pore shapes in Al alloys. In addition, Shchitsyn et al. [102] revealed that Ti-6Al-4V alloy deposited using the cold metal transfer (CMT) and interlayer cold hammered met the mechanical strength of wrought Ti-6Al-4V.

Similar to hammer peening, ultrasonic peening (Fig. 10) is also a traditional deformation method used to reduce residual stresses and improve the mechanical properties and fatigue life of the welded joints [103]. An ultrasonic probe with a power of 100 W working at a high frequency (~20 kHz) was commonly used. Aligned steel impact tools with a needle-like aspect (diameter of 3 mm and spaced 2 mm; Fig. 10b) deformed the bead surface. Gale and Achuhan [104] (AISI 316L stainless steel DEDed-laser) combined cycles of deposition and deformation. These authors deposited a specific sample height (2 layers) and subsequently conducted ultrasonic peening on the as-built material, observing a significant increase in the material hardness (from 2.4 to 4 GPa). Wang and Shi [105, 106] demonstrated that cold ultrasonic peening homogenized the residual stress distribution, altered the main residual stress component to a compressive state, and induced a finer microstructure of Inconel 718 DEDed-laser. Yi et al. [37] showed that even for the high penetration process (arc plasma-DED + interlayer ultrasonic peening—Fig. 12), the ultrasonic peening mechanically affected zone (deep deformation) could induce microstructural refinement. In addition, due to the small equipment size (Fig. 10b) and low peening load (e.g., operated manually in welding), ultrasonic peening can be integrated within a gas protection chamber, allowing it to be coupled with the powder bed fusion (PBF). Zhang et al. [107] verified that interlayer cold ultrasonic peening could reduce and close discontinuities (Fig. 11) by inducing top layer deformation, subsequently crushing and altering defects (e.g., porosity and lack of fusion) morphology, as observed by Gu et al. [74] (interlayer rolling—Fig. 4). In addition, it was verified that interlayer cold ultrasonic peening prevents epitaxial columnar grain growth (refining the microstructure) and reduces the residual stress levels for Ti-6Al-4V fabricated via PBF. Therefore, ultrasonic peening is also considered suitable for commercial alloys DEDed, similar to hammer peening.

Ye et al. [108] (DED-laser) and Li et al. [109] (DED-laser) developed a hot ultrasonic micro-forging system with an operating frequency of 20 kHz; Xiong et al. [110] (DED-arc), a hot hammer penning system with an operating frequency of 21 Hz. These systems [108–110] (Fig. 12) resemble the cold hammer previously shown in Fig. 10 b, where the main difference between them is the peening temperature. Deformation occurred immediately after deposition, when the deposited layer was still at a higher temperature, as with those for the hot rolling variants. The abovementioned systems involve a conventional welding torch coupled with a separated plastic deformation device, i.e., uncoupled deposition and deformation.

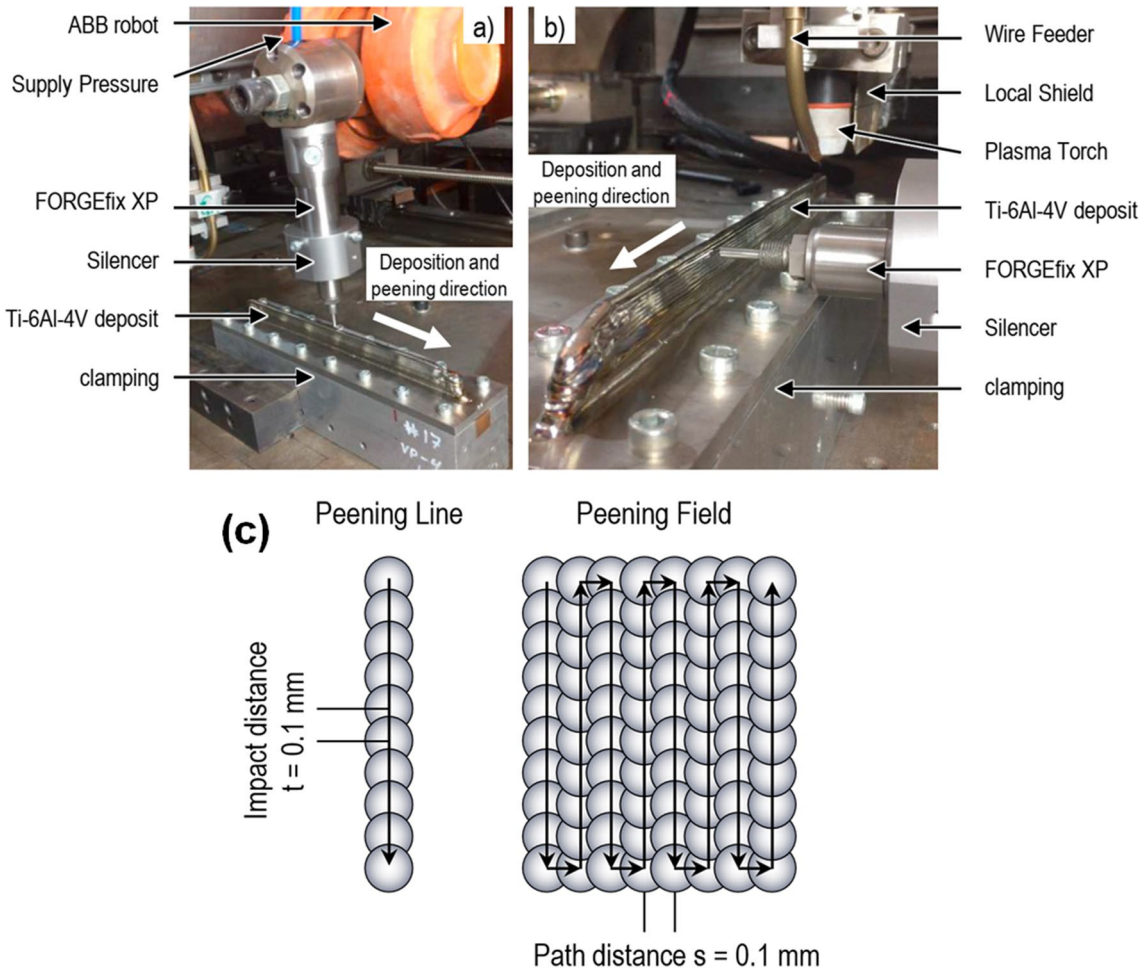

Fig. 9 Setup of machine hammer peening: **a** vertical peening, **b** horizontal, and **c** flexibility path planning (adapted from [97])

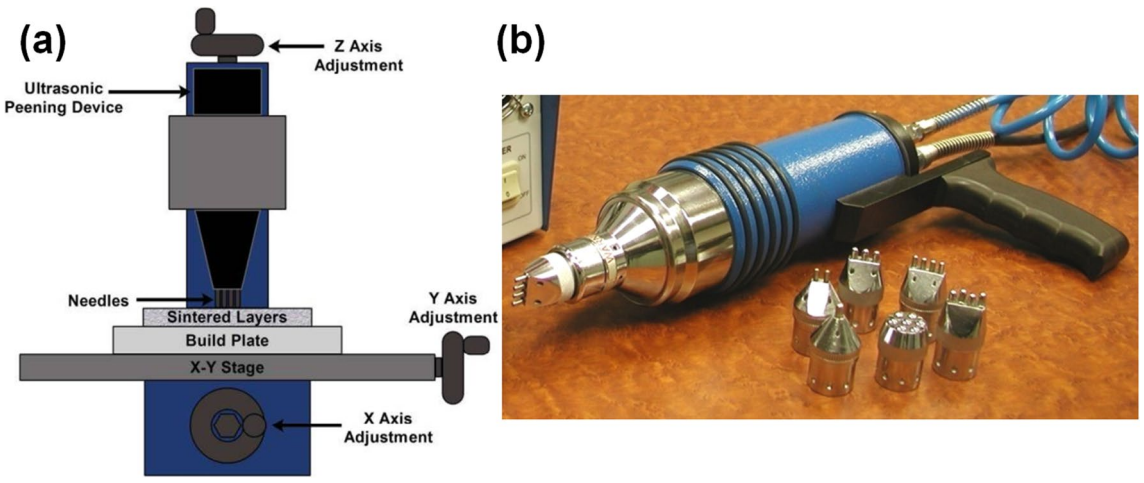

Fig. 10 **a** Schematic view of the ultrasonic peening setup (adapted from [104]) and **b** impact tools "needles" (adapted from [190])

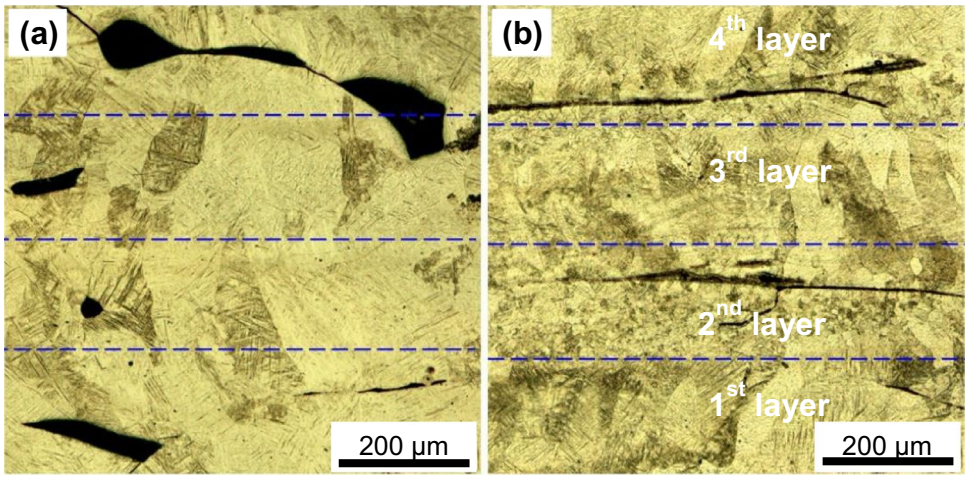

Fig. 11 Effect of ultrasonic peening on the PBF discontinuities: **a** without and **b** with ultrasonic peening (from [107])

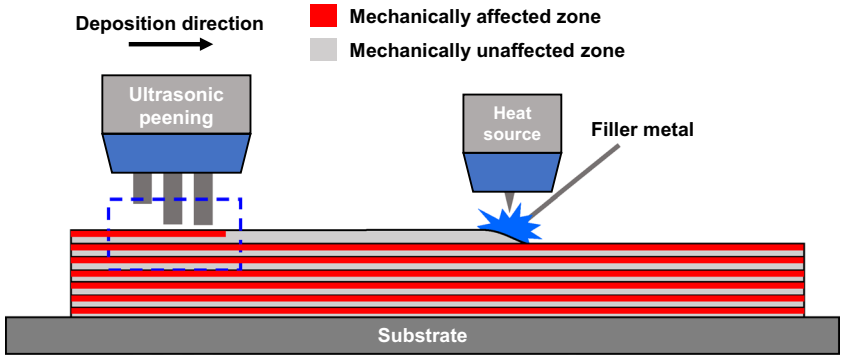

Fig. 12 Schematic representation of ultrasonic peening coupled with DED-arc (adapted from [37])

Duarte et al. [20, 21] developed a DED-arc + interlayer hot forging (Fig. 13a, b) variant, which consisted of a dedicated GMAW torch equipped with a hammer, activated by vibrating actuators (electromagnetic, solenoid, or pneumatic), which could operate at different frequencies (1–10 Hz) and loads (1.5–5 kN). The hammer path planning followed the torch, and the hammer size, and distance from the welding pool control the forging temperature. Duarte et al. [20] and Farias et al. [111, 112] showcased that hot forging could reduce pore size, alter its morphology, and improve the mechanical properties of 316L stainless steel and Inconel 625 DEDed-arc. In addition, Gao et al. [113] customized a machine that combined DED-arc and single-point incremental hot forming, which operated at a maximum load of 1.5 kN, refined the microstructure, and improved the mechanical properties of 316L stainless steel DEDed-arc.

Hammering, peening, and forging (cold and/or hot) showed advantages in relation to rolling, especially due to the lighter equipment, higher versatility and flexibility, lower loading forces, and freer path planning. However, the hot interlayer hammer peening and forging are limited to one-way deposition strategies, as they are challenging to use in oscillating (e.g., the deposition torch moves as a sine/square/triangle wave) and/or reversing deposition strategies [33], e.g., even layer number from right to left (→) and odd number layers with a reversed direction (←). In this sense, Duarte et al. [21] improved their previous interlayer hot forging system [20] by changing the configuration of the forging tool from a cylindrical hammer to a circular crown shape directly connected to the welding gas nozzle (Fig. 13c). Thus, the deposition and deformation became coaxial, thereby overcoming the path planning limitations, i.e., the forging region is independent of the direction of deposition (Fig. 13d). Finally, for the first time, Karunakaran et al. [114] and Gupta et al. [115] integrated an interlayer cold hammering/peening system into a hybrid 3D printing machine (DED cell–laser, GTA, and GMA–and machining setup). These authors noted that hammering/peening/forging could be directly integrated into the manufacturing setup without altering it significantly; i.e., they did not need a specific manufacturing setup. This differs from the other interlayer mechanical deformation systems, such as laser shock peening and hot/cold rolling, which demand a dedicated setup.

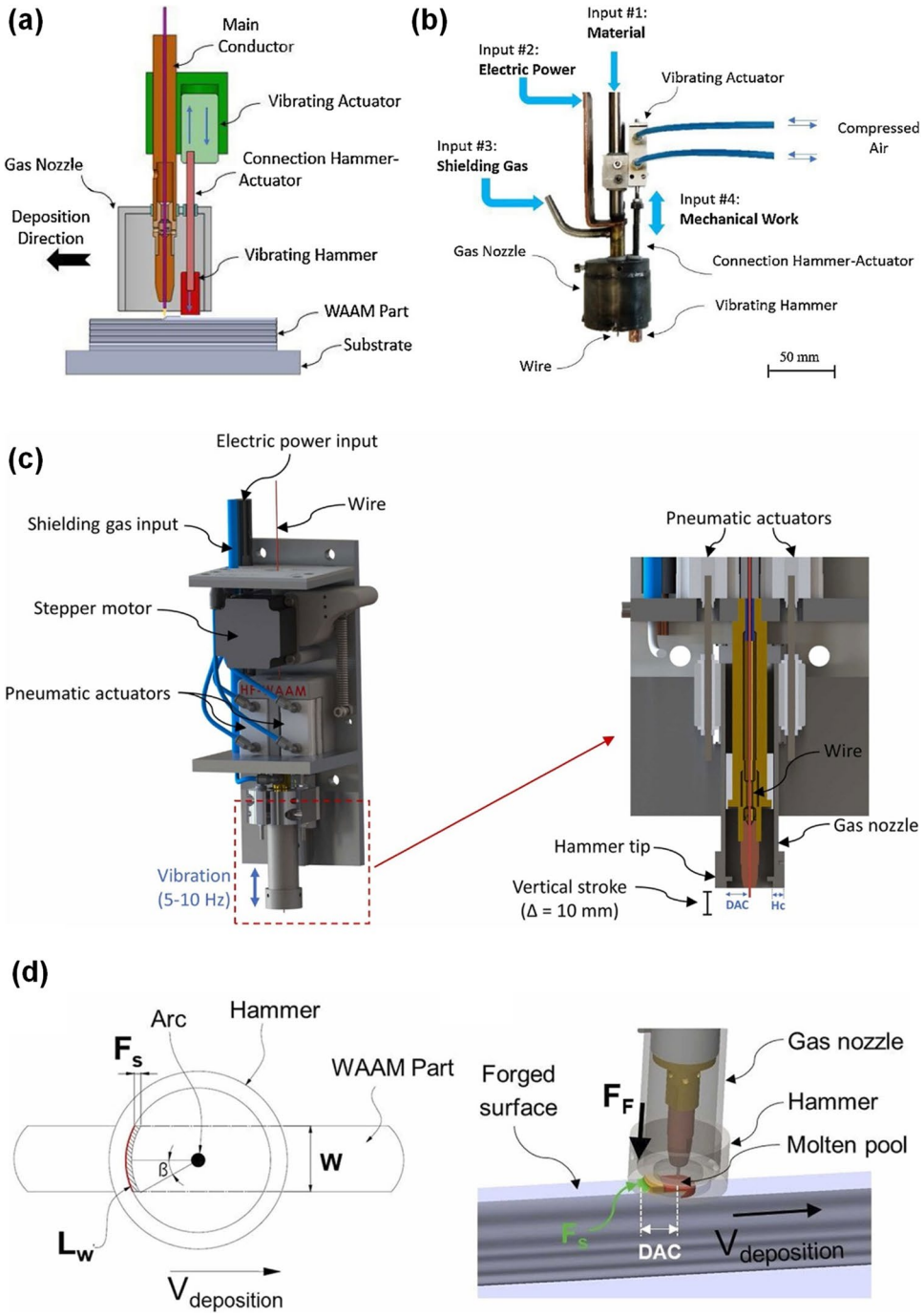

Fig. 13 DED-arc + interlayer hot forging: **a** schematic representation and **b** components (from [20]). **c** Developed of coaxial hot forging, and **d** details of the circular crown concentric with the welding nozzle (from [21])

2.3 Laser shock peening

Another deformation process that exhibits potential for integration with AM processes is laser shock peening (LSP). In this method, shockwaves are generated by localized laser heating, serving as the peening source [116]. Although LSP falls under the broader category of peening, it is regarded as a distinct class due to its unique peening source—shockwaves—and the growing interest in its application coupled with AM processes. LSP (Fig. 14) is characterized by local and fast heating by a pulsed laser, which generates a plasma that expands (material ablation) and creates a shockwave (high strain rate) at the material surface, which induces a compressive residual stress field and alters the material surface and microstructure (increasing the dislocation density and modification of the grain morphology) [117, 118].

Direct ablation, wherein LSP is applied directly to the material surface, is generally avoided due to its potential to alter the surface of the part. Instead, the process employs a protective coating (such as Al foil) along with

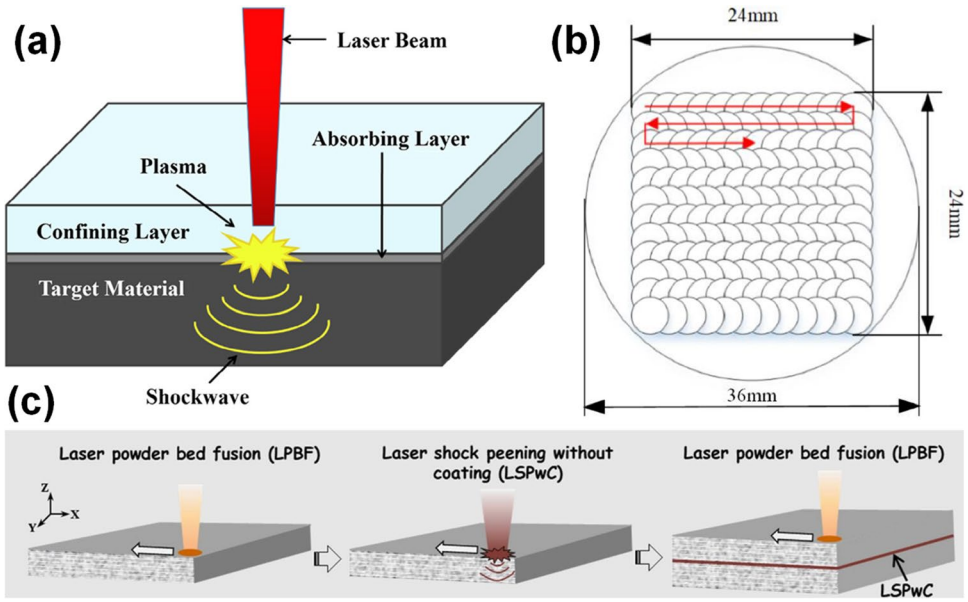

Fig. 14 **a** Laser shock peening (LSP) shockwaves generation [198], **b** free path planning [199], and **c** intermittent LSP process coupled to laser PBF [143]

a transparent confining layer (like a water film) to maintain a smooth surface. However, for interlayer LSP applications during AM deposition, as adopted by Sealy et al. [119] (laser-DED) and Zhou et al. [120] (laser-DED), LSP must be applied without the coating and transparent confining layer to ensure productivity without reducing material printability, i.e., directly on the just deposited material. The application of protective and transparent layers during the deposition of each layer reduces the process efficiency and may not be feasible. This concern is particularly relevant for processes that utilize powder as feedstock material, such as PBF and laser-DED. In such processes, any residual water from the transparent confining layer can interact with the feedstock material, leading to powder agglomeration and contamination. These interactions can introduce pores and compromise both the formability of the layers and the resulting material properties. Furthermore, based on the literature survey [121–136], it becomes clear that the LSP deformation zone penetration (measuring 0.7 ± 0.20 mm) is adequate to achieve grain size refinement in laser- and electron beam-based DED as well as PBF. However, its impact is significantly limited in arc plasma-based DED due to the extensive deposition penetration [137–139] since the previously deposited layer is almost entirely remelted. It is worth noting that, to the best of the authors' knowledge, the in situ interlayer LSP was not applied to DED-arc components; only Sun et al. [121] applied the LSP (post-deposition) to the side surface of 2319 aluminum DEDed-arc walls. The authors [121] reported an increase in the quasi-static mechanical properties due to induced work hardening. Similar to LSP, shot peening also has a limited in situ interlayer applicability because the peening media (e.g., cast steel, ceramics, glass, and sand) can contaminate the layer surface and powders and the limited depth of the deformation (~ 0.2–0.4 µm) [140–142].

Lu et al. [134] and Lu et al. [143] (Fig. 14c) deposited three consecutive layers of Ti-6Al-4V using PBF and performed the LSP. This process occurred in an intermittent mode (i.e., deposition stop to execute the LSP—coating and transparent confining layers) and serves as a showcase concept of AM + interlayer LSP. However, due to the intermittent aspect, the procedure developed by Lu et al. [134] and Lu et al. [143] had a low productivity. Lu et al. [134] verified that interlayer LSP refined the prior β grain size and induced an almost equiaxed grain morphology, which improved the quasi-static mechanical properties of Ti-6Al-4V PBFed + interlayer LSP, especially the yield and ultimate tensile strengths, in relation to Ti-6Al-4V PBFed. Zhou et al. [120] (AlSi10Mg alloy laser-DEDed) improved the experimental setup of Lu et al. [134], Lu et al. [143], and Sealy [119]. They introduced an in situ interlayer direct ablation LSP approach, eliminating the need for both the coating and transparent constraining layers. This modification induced a deformation penetration of 0.5 mm (measured via the residual stress profile), drove pore closure, and increased the quasi-static mechanical properties concerning the laser-DED. Furthermore, to the best of the authors' knowledge, those were the only works [119, 120, 134, 143] that coupled AM (DED and/or PBF) with LSP. Notably, the approach introduced by Zhou et al. [120] stands out as the sole method that integrates in situ LSP and part printing.

According to the literature surveyed [121–136], in most studies, the LSP was applied after part fabrication; i.e., as mechanical surface treatment, and its effect on fatigue life, quasi-static mechanical properties, corrosion resistance, and

residual stress relief was evaluated. In addition, it is worth mentioning that due to the use of a laser (shockwave generation) as the deformation tool, LSP can be readily integrated into laser- and electron beam-PBF (processes that require a chamber to powder handling and consolidation or control the atmosphere), which may expand the interlayer mechanical deformation for all metal AM processes, as reported recently by Sealy et al. [119], Lu et al. [134], and Lu et al. [143]. Furthermore, considering the scarce literature on DED + in situ interlayer LSP (at the moment there is only one publication [120]) and the shallow deformation depth (lower than peening/forging), the in situ LSP can be suited for low penetration processes (e.g., laser- and electron beam-based AM). Thus, the discussion on the effects of the in situ interlayer LSP on the microstructure (grain size refinement) and its comparation with the literature and other AM processes becomes impractical, not being addressed in Sect. 3.

3 Grain size refinement mechanisms

This section addresses the grain size refinement mechanisms of the interlayer (cold and hot) mechanical deformation systems (rolling and hammering, peening, and forging) previously described. The grain size refinement mechanisms were classified according to alloy type (transformable and non-transformable) and temperature of deformation (cold—below the recrystallization temperature—and hot—consolidated feedstock material still incandescent at a temperature higher than the recrystallization temperature). Transformable alloys (e.g., Ti-6Al-4V and low-alloy steels) are classified as alloys that undergo solid-state allotropic (e.g., from austenite to ferrite) transformations during the thermal cycle. Non-transformable alloys (e.g., Ni- and Al-based) do not undergo solid-state allotropic transformations during the thermal cycles, maintaining the primary microstructure during the thermal cycles and post-deposition heat treatments same matrix phase.

3.1 Rolling

3.1.1 Transformable solid-state alloys

The thermal conditions (intense thermal gradient and almost directional heat flux) and partially remelting of the substrate and/or previously deposited layer favor the epitaxial grain growth during DED deposition, which is commonly characterized by an oriented microstructure and anisotropic behavior, even for solid-state transformation alloys (e.g., Ti-6Al-4V). In this sense, the deposition + interlayer mechanical deformation can induce grain refinement (dynamic and/or static recrystallization), which can reduce the texture index (randomizing the microstructure) and homogenizes the properties throughout the part fabricated via DED.

Most studies on the effect of rolling on grain refinement focus on the Ti-6Al-4V alloy; however, the key grain refinement mechanism can be extended to other transformable alloys. The Ti-6Al-4V alloy solidifies as coarse and oriented β (body-centered cubic) grains, which during the cooling (~ 1000 °C; β *transus* temperature), partially transforms into

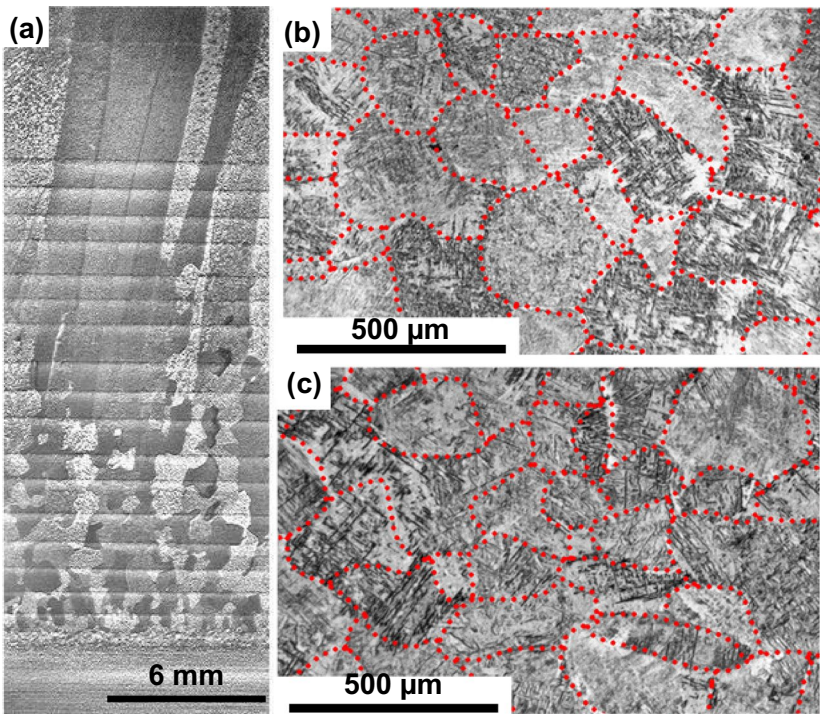

Fig. 15 Prior β grain morphology of the Ti-6Al-4V DEDed-arc: **a** unrolled condition, **b** 50 kN rolling force, and **c** 75 kN rolling force (from [90])

α (hexagonal close-packed) so that the final microstructure is composed of the α-phase (e.g., Widmanstaätten and grain boundary) and some retained prior β-phase. For more details regarding the welding metallurgy of α + β Ti alloys, readers are referred to Short [144]. Similar solid-state transformations are observed in materials such as low-alloy steel (austenite → ferrite) and Cu-Al8% (β → α) [21], for example.

Martina et al. [90] observed that the prior β grain size of the Ti-6Al-4V reduced significantly (Fig. 15) due to interlayer cold rolling. This grain refinement effect was notable when using a higher rolling load (75 kN). In addition, Martina et al. [90] tested the influence of the posterior layer on a previously rolled layer (Fig. 16), identifying three zones: (1) columnar grains, (2) recrystallized zone, and (3) previous unaffected layer. In Fig. 16, zone (1), closer to the top of the deposited layer, exhibited the columnar prior β grains aligned with the build direction. Zone (2) corresponds to the grains that grew epitaxially and were deformed (previous layer) and, in the subsequent layer deposition (reheating thermal cycle), statically recrystallized. Thus, despite zone (1) possessing a columnar aspect, the finer grains in the zone (2) inhibited prior β grains to cross several layers (some grains could reach up to 12 mm in the DED-arc condition—Fig. 15). The length of zone (3) depends on the deposition and deformation parameters since the recrystallization temperature is related to, in addition to other factors, the deformation stored energy, temperature, and time [145], where the first is a function of the rolling load and the others of the thermal cycle (i.e., deposition parameters). It is worth noting that, due to the higher cold rolling loads, the remaining deformation zone length—zone (3)—is superior to deposition penetration (Fig. 16), which ensures an effective prior β grain size refinement mechanism in the entire deposited layer.

McAndrew et al. [70] reported that, for multi-layer multi-bead DEDed-arc parts, the grain size refinement, as observed by Martina et al. [90] (multi-layer single-bead), effectively did not occur. This was attributed to the lateral geometrical restraint of the multi-bead multi-layer thick part; i.e., the adjacent layer previously deposited prevents the deformation of the most recently deposited layer, inducing an insufficient stored energy required for static recrystallization. However, using an inverted roller profile (Fig. 2c; deeper strained zone), enough stored energy to promote static recrystallization can be achieved, expanding the interlayer cold rolling grain size refinement in thicker parts. McAndrew et al. [70] mapped the deformation (Fig. 17) induced by rolling, showing that the maximum strain occurred at the edges of the rolled layer at a depth of 3 mm; close to the surface, the deformation was minimal due to friction between the roller and the surface, preventing material flow. Figure 17 also shows that the deformation penetration can extend up to 6 mm so that the deposition penetration (~ 1–2 mm) is always smaller than the deformation zone, which reinforced the results showed by Martina et al. [90]. The results of Donoghue et al. [146] corroborated with the McAndrew et al. [70]. Donoghue et al. [146] first observed that the electron backscatter diffraction (EBSD) band contrast (i.e., increase in the residual strain) reduces with local and posteriority increases and reaches a constant value, corresponding to the region unaffected by cold rolling. Figure 18 a and b evidence

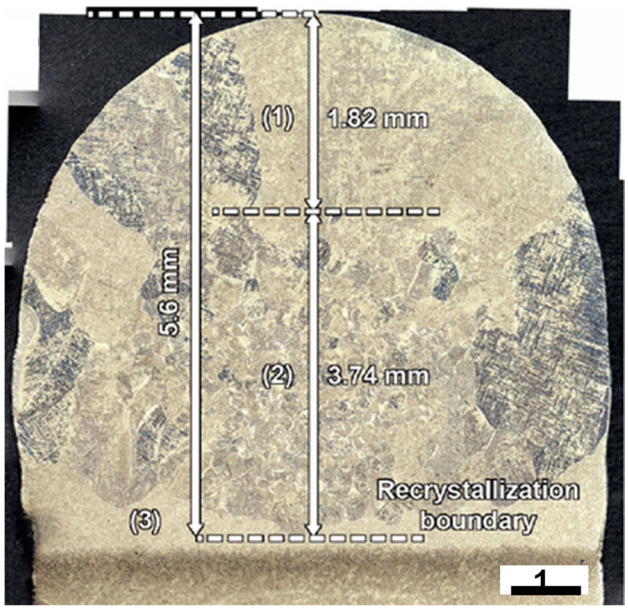

Fig. 16 Effect of the posterior deposition layer on the previous layer. (1) Columnar grains, (2) recrystallized zone, and (3) previous unaffected layer (from [90])

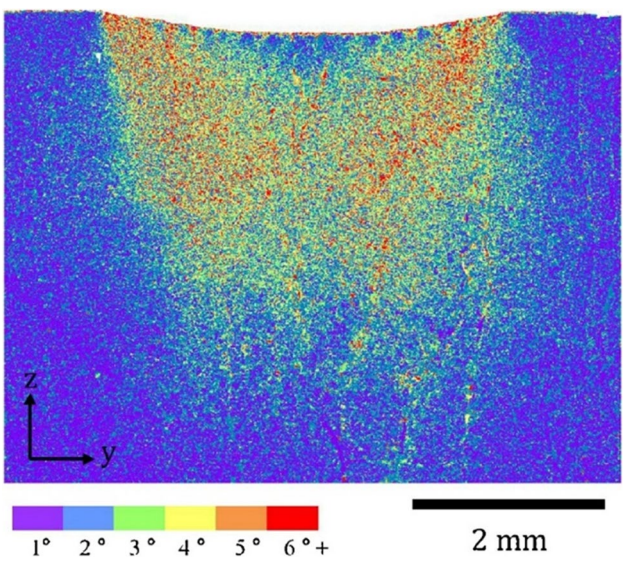

Fig. 17 EBSD map of the plastic strain of a Ti-6Al-4V DEDed-arc rolled (from [70])

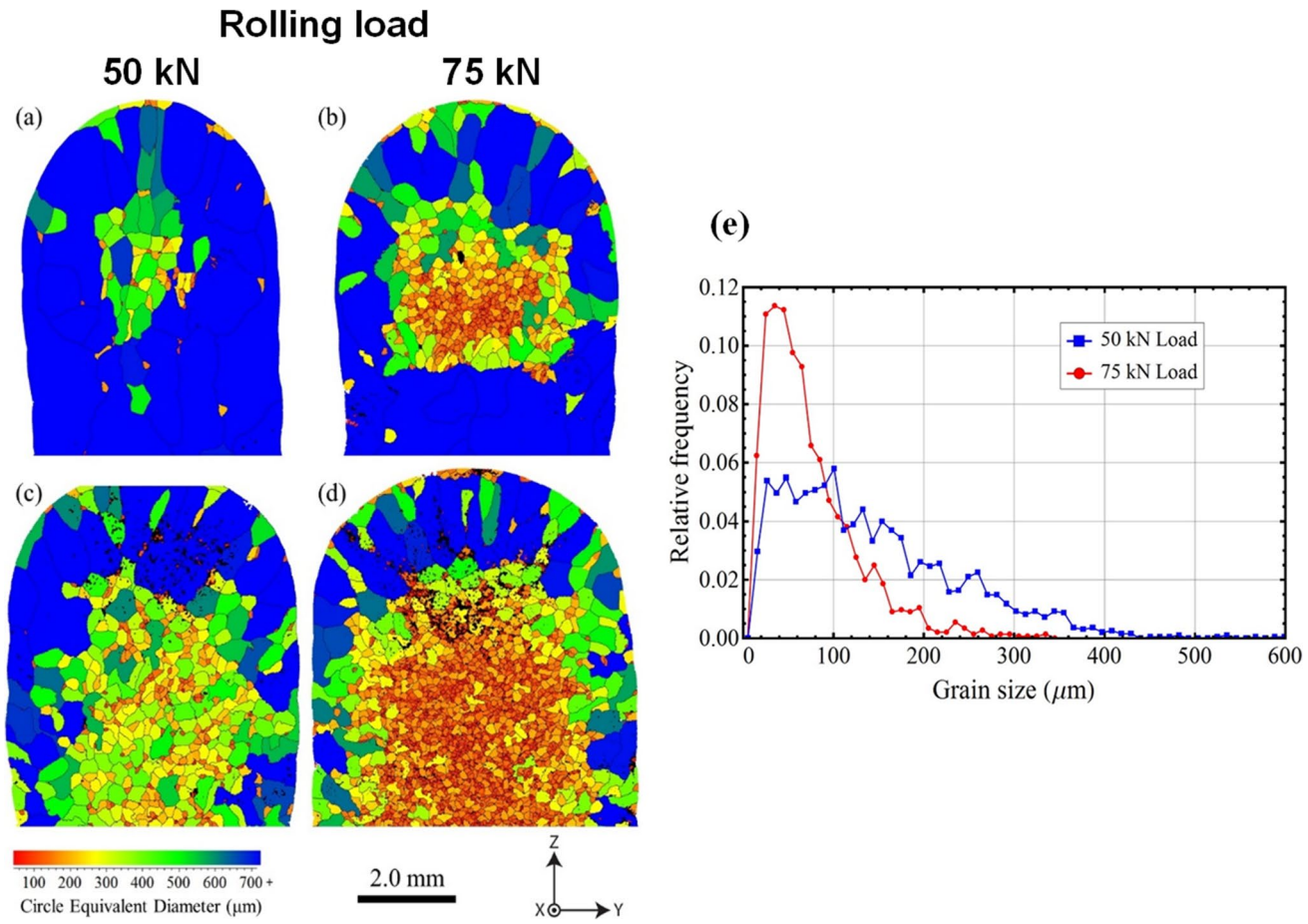

Fig. 18 Prior β grain size maps: **a**, **b** rolling applied in the penultimate layer; **c**, **d** rolling applied in the entire part; € grain size distribution (from [146])

that the maximum static prior β recrystallization coincides with the lowest band contrast region (highest deformation zone) and that the grain size refinement effect increases with the rolling load. Figure 18 c and d illustrate the effect of interlayer cold rolling in deposited layers, which indicated that the grain size was refined throughout the part. Moreover, the lower rolling load (50 kN) generated a higher and scattered grain size (Fig. 18e), i.e., it was less efficient.

According to Ding and Guo [147], the macroscopic compression (height reduction of 19% for 75 kN rolling load) observed by Donoghue et al. [146] is insufficient to induce the prior β grain refinement via static recrystallization during the reheating thermal cycle. In addition, β nucleation follows the Burgers orientation crystallographic relationship, which ensures that, during heating ($\alpha \rightarrow \beta$ allotropic transformation), the generated β grains have the same crystallographic orientation as those of the prior β during cooling ($\beta \rightarrow \alpha$). This allows the next deposited layer to have almost the same crystallographic orientation (epitaxial nucleation and growth) as the previously deposited one, resulting in a typical coarse and texturized prior β grain [144]. For effective prior β grain size refinement, the interlayer rolling strain must induce β nucleation without following Burger's orientation [148]. Donoghue et al. [149] and Davis et al. [150] reported that interlayer rolling can induced the twining of the prior β (β′, Fig. 19), which explains the prior β grain size refinement in DEDed-arc + interlayer cold rolling. Twinned β′ had a mobile grain boundary and an orientation different from the remaining β phase (Fig. 19c); i.e., it did not follow the Burgers orientation crystallographic relationship, consuming the prior β and α during the reheating thermal cycle. β′ continues to grow until it becomes impinged by other β′ grains (Fig. 19d), which results in a fine and aleatory microstructure. This proposed mechanism [149, 150] is in accordance with Martina et al.'s [90] results, which showed that a higher rolling load resulted in a finer β grain size, i.e., the higher rolling loads enhanced the twining process (β′ formation).

In addition to the Ti-6Al-4V alloy, Colegrove et al. [31] and Dirisu et al. [68] also observed refinement of the parent phase (prior austenite) as a result of interlayer cold rolling in low-alloyed steel fabricated using DED-arc. The

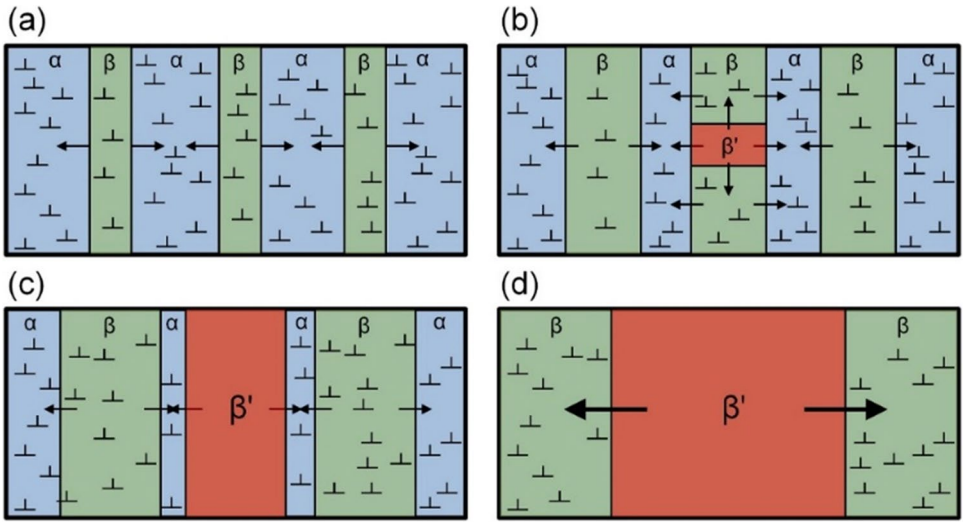

Fig. 19 β-grain refinement mechanism for Ti-6Al-4V DEDed-arc rolled: **a** stored dislocations due to cold rolling, **b** twinning β-grain (β′) during heating thermal cycle, **c** β′ grows into the neighboring deformed β phase, and **d** α → β solid-state phase transformation and β′ growing (from [149])

changes in the prior austenite grain size alter the kinetics of the austenite-ferrite phase transformation. With a finer grain size induced by interlayer cold rolling, diffusional transformations, such as ferrite formation (e.g., polygonal and acicular), is favored over adiffusional transformations (e.g., martensite). In other words, the finer prior austenite grain size reduces the hardenability of low-alloyed steel fabricated via DED-arc. In addition, as observed with Ti-6Al-4V (arc plasma DED + cold rolling), an increase in the rolling load also leads to finer prior austenite grain size. However, the thermal conditions during the thermal cycles were only slightly altered, which results in almost identical constituents (polygonal and acicular ferrites, low-alloy steel, and basketweave α, Ti-6Al-4V) for both conditions (interlayer rolled and unrolled); also, due to the finer austenite grain size, the rolled condition showed a finer ferrite grain in relation to unrolled (8.6 vs. 14.5 μm) [68]. Colegrove et al. [31] suggested that the refinement of austenite grain size resulted from a high nucleation rate induced by the residual deformation. However, this phenomenon has not been thoroughly studied and requires further clarification. Given the low deformation during cold rolling (similar to Ti-6Al-4V), the crystallographic relationship between austenite and ferrite (e.g., Kurdjumov–Sachs), and the presence of residual austenite at room temperature (as observed in martensite-austenite constituents in weld metals) [151], it is possible that similar behavior of the prior β grain (Fig. 19), i.e., retained austenite twinning, can occur. Thus, interlayer cold rolling may not induce a higher nucleation rate of austenite during the heating as indicated by Colegrove et al. [31] (recrystallization) but the twinning of the retained austenite, which will grow during reheating thermal cycle and consume the remaining microstructure without crystallographic correlation with the previous ferrite microstructure. Besides, Xu et al. [152] also observed a prior austenite grain refinement in a maraging steel DEDed-arc + interlayer cold rolling.

Tian et al. [88] (DED-laser) and Gao et al. [82] (DED-arc) observed (Fig. 20) a considerable prior β grain refinement, similar to cold rolling, using interlayer hot rolling, with a remarkable β phase texture intensity reduction (from 15.8 to 3.2). Gao et al. [82] explained the grain size refinement using the mechanisms proposed by cold rolling [149, 150] (Fig. 19). In addition, Gao et al. [82] reported that dislocations, twins, and stacking faults are introduced during interlayer hot rolling, which supplies sufficient driving force for dynamic recrystallization in regions with peak temperatures higher than β *transus* and supported the grain size refinement mechanism proposed by Donoghue et al. [149] and Davis et al. [150].

Fu et al. [78] studied the behavior of bainitic steel parts fabricated via DED-arc + interlayer hot rolling (see Fig. 5). Fu et al. [78] made an observation similar to Martina et al. [90] (interlayer cold rolling) regarding different deformation-affected zones by the interlayer hot rolling, i.e., a large deformation, small deformation, and undeformed zones. Furthermore, the selected roller-torch distance with a rolling temperature of 900 °C allows deformation but not austenite recrystallization (non-recrystallization temperature). This introduces deformation bands (austenite had a low SFE energy) that increase the ferrite nucleation kinetics during the cooling thermal cycle (similar to thermomechanical controlled rolling [153]), generating a homogenous fine ferrite grain size (~7 μm). Ma et al. [81] reinforced the above results; the authors indicated that the roller-torch distance controls the final microstructure. Ma et al. [81], using a concept similar to that applied to arc welding, redefined the zones affected by interlayer hot rolling as a function of the peak temperature, where, at the medium–high-temperature (non-recrystallization austenite temperature), maximum

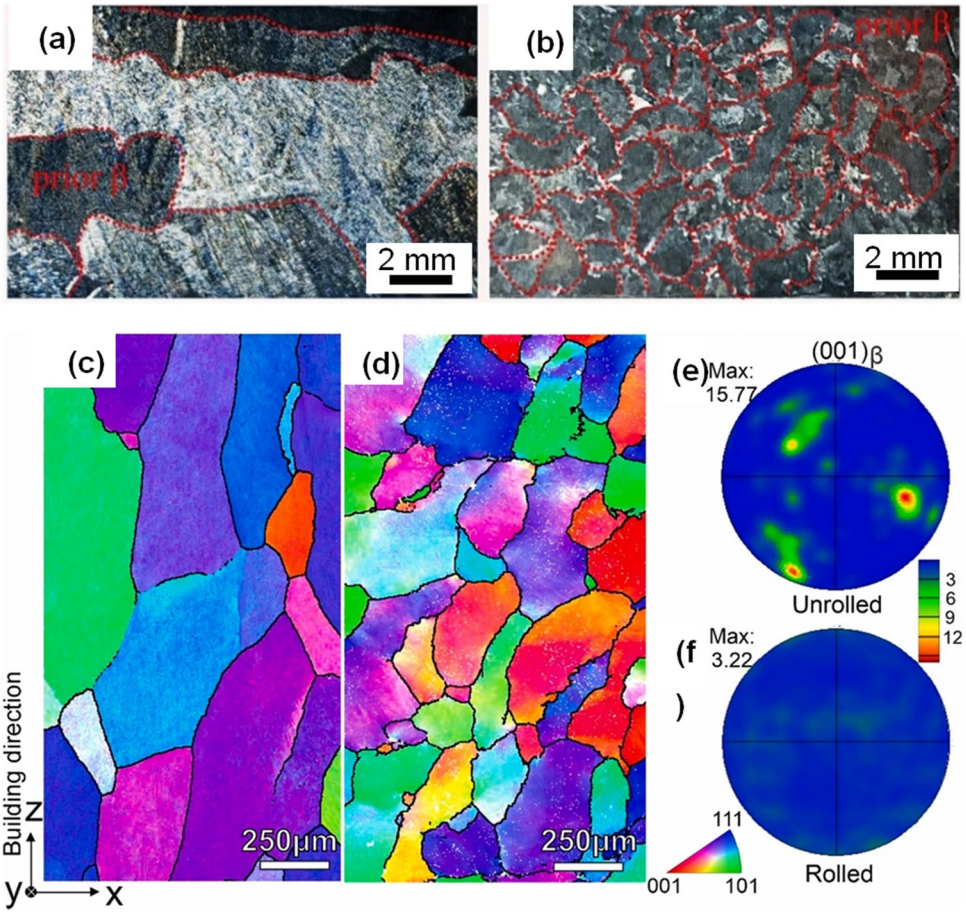

Fig. 20 Interlayer hot rolling grain refinement for the Ti-6Al-4V alloy: **a** DED-arc, **b** DED-arc + interlayer hot rolling (adapted from [82]), **c** DED-laser, DED-laser + interlayer hot rolling; **e** and **f** are the prior β pole figures referring to EBSD (**c**, **d**), respectively (adapted from [88])

prior austenite grain size refinement was observed due to the reheating thermal cycle (α → γ transformation) and intense γ nucleation rate (deformation bands) [154]. In addition, the residual stored deformation energy enhances the ferrite nucleation sites; therefore, the synergic effect of finer austenite grain size and higher ferrite nucleation rate allows the development of a finer ferrite microstructure for low-alloyed steels fabricated via DED-arc + interlayer hot rolling concerning DED-arc.

For the solid-state transformation materials, the final microstructure results from the solid-state transformations; thus, despite the interlayer deformation refining the prior microstructure (e.g., β and austenite, for Ti-6Al-4V and low-alloy steels, respectively), it is worth analyzing if the final microstructure is also affected (product phase morphology). In addition, for low-alloyed steels and Ti-6Al-4V, the solid-state transformation has a crystallographic orientation relationship between the parent (β and austenite) and product phases (ferrite—low-alloy steels—and α—Ti-6Al-4V) that is the Kurdjumov–Sachs and Burgers Orientation, respectively. Thus, the grain size and crystallography of the parent phase directly affect the final microstructure since the grain boundary area plays a role in the transformation kinetics (e.g., finer austenite grain size reduces the hardenability). Zhao et al. [155] (low-alloyed steels) reported that the fine austenite grain size and the remaining residual strain enhance the formation of acicular ferrite. This was corroborated by Colegrove et al. [31], who observed a finer ferrite grain size when increasing the rolling load, promoting acicular ferrite and decreasing the low toughness constituents, such as grain boundary ferrite. For a Ti-6Al-4V alloy, the prior β grain size refinement had a low influence on the α lath thickness [88]. However, the material at room temperature (α field) showed a low texture intensity, which approximately equalized the quasi-static mechanical properties (i.e., reduced the anisotropy). Gao et al. [82] (Ti-6Al-4V) observed microstructural changes due to interlayer hot rolling, where the common basketweave and α grain boundary microstructure (DED-arc) became majority α acicular (DED-arc + interlayer hot rolling), corroborating the results of Martina et al. [90] (finer α grain size due to cold rolling). These authors [82] attributed this behavior to the increase in the length of prior β grain boundary (fine grain size), which enhanced the intragranular α nucleation rate and reduced the overall α lamella size.

3.1.2 Non-transformable solid-state alloys

The coarse grain and texture problems become more pronounced in alloys that do not undergo allotropic transformations during the cooling thermal cycle, i.e., the primary microstructure (e.g., dendric, segregation, and coarse and oriented grains) remains at room temperature [156]. Thus, interlayer rolling can be an interesting alternative to inducing grain size refinement and overcoming the low performance of cast-like microstructures. Some examples of alloys with primary microstructures are Ni and Al-based alloys (e.g., Inconel 718 and Al-Mg4.5Mn alloy). The major grain size refinement mechanism for these alloys is the dynamic/static recrystallization induced by the deformation storage energy. In addition, two grain refinements can occur, static recrystallization during the heating thermal cycle (cold rolling) and in situ dynamic recrystallization (hot rolling) and subsequently static recrystallization during post-deposition heat treatment (both cold and hot rolling) [89, 157–160]. Xu et al. [89] observed (Fig. 21) these two grain refinement mechanisms for Inconel 718 DEDed-arc + interlayer cold rolled, which resulted in a significant grain size refinement (15.7 µm vs. 26.7 µm—wrought material). Zhang et al. [158] (Inconel 718 DEDed-arc) showed that a higher rolling force and high deformation depth resulted in finer grain size. Hönnige et al. [157] (Inconel 718 DEDed-arc) optimized the rolling load (50 kN) and the solution heat treatment condition (AMS 5662), obtaining an approximately fully recrystallized equiaxial microstructure. Additionally, Hönnige et al. [157] highlighted that the two static recrystallizations, namely reheating thermal cycle and heat treatment, have similar proportions, where the first refined the region close to the fusion line (higher temperatures and strain energy) and the second one refined the regions with lower strain energy (from the middle to the bottom of the layer height).

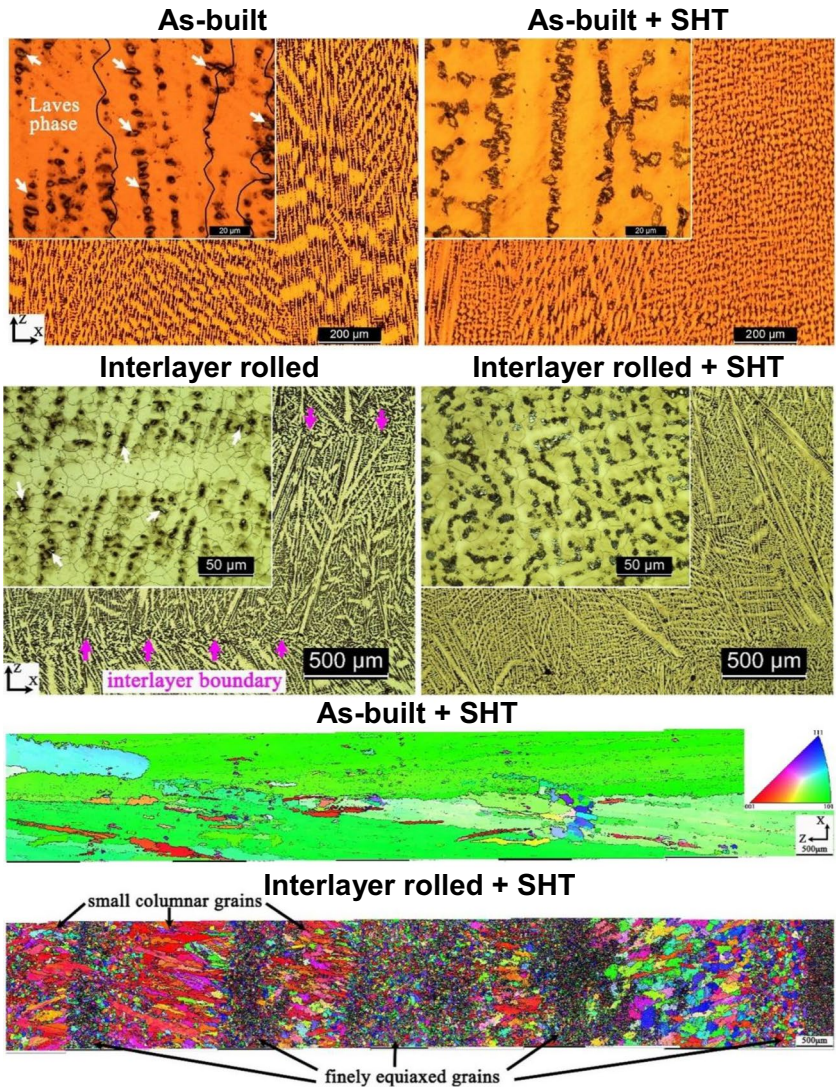

Fig. 21 Optical micrographs and EBSD orientation maps of Inconel 718 DEDed-arc with and without interlayer cold rolling (from [89]). SHT means solubilization heat treatment

Gu et al. [160] (DED-arc + cold rolling) reported that Al–6.3Cu alloy (2319; precipitation hardening) also showed the two grain size refinement mechanism mentioned above. Otherwise, the solid-solution strengthened Al-Mg4.5Mn alloy (DED-arc + cold rolling), unheated-treatable, showed, as the major grain size refinement mechanism, the static recrystallization during reheating thermal cycle due to the non-post-deposition heat treatment; in addition, the authors [159] indicated that due to high load rolling (45 kN; intense strain), some dynamic recrystallization can occur. Thus, for alloys that do not require post-deposition heat treatments (e.g., solid-solution strengthened—Inconel 625 and Al-based alloys series 5xxx), the interlayer cold deformation grain size refinement could be limited to the reheating zone, maintaining coarse and oriented grains, as showed in Fig. 21.

The hot rolling processes have a different grain refinement mechanism than cold rolling. In the first case, the rolling follows the deposition with the consolidated feedstock material still hot, leading to dynamic recrystallization. Furthermore, residual deformation where the region is hot deformed but not dynamically recrystallized can drive static recrystallization during the reheating thermal cycle and post-deposition heat treatments (similar to cold rolling). Zhang et al. [32], Hai-ou et al. [161], and Xi et al. [77] observed a change from the columnar and oriented grains to homogeneous equiaxial

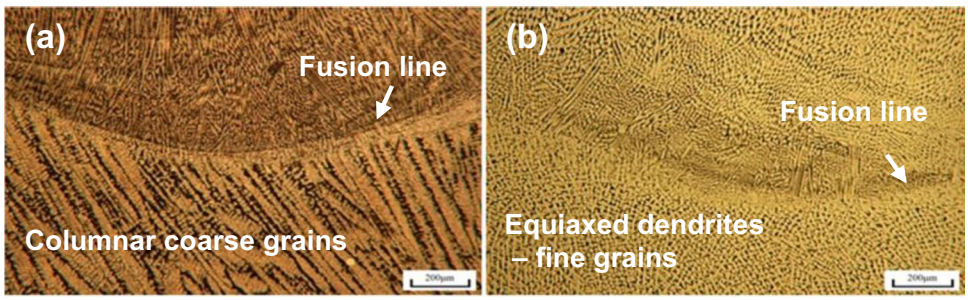

Fig. 22 **a** Microstructures of the 304 stainless DEDed-arc and **b** DEDed-arc + interlayer hot rolled (adapted from [77])

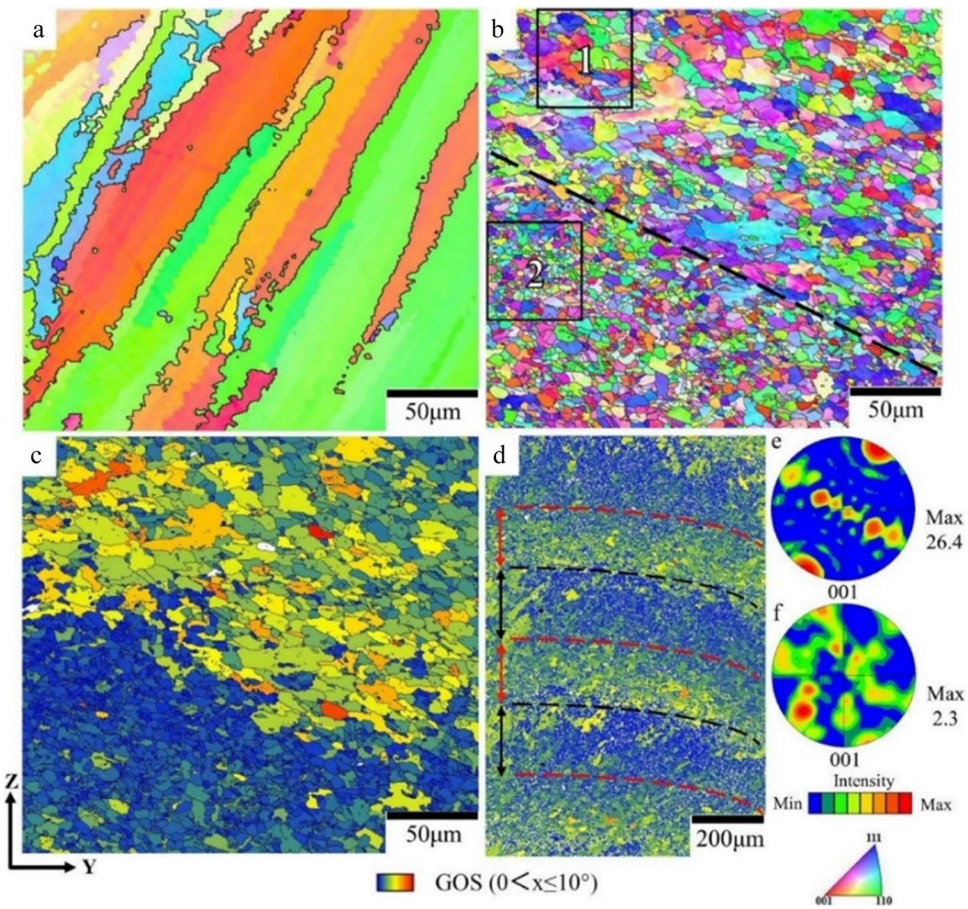

Fig. 23 EBSD maps of the Inconel 718 DEDed-laser: **a** as-built, **b** interlayer hot rolling grain refinement, **c** grain orientation spread (GOS), alternating bands of recrystallized and deformed grains, **e** (001) pole figure for as-built, and **f** (001) pole figure for interlayer hot rolled (from [87])

grains (passing through more than one layer; Fig. 22) for the 304 stainless steel DEDed-arc + interlayer hot rolling (Figs. 6 and 7). These authors attributed the grain size refinement to static recrystallization of dendrites' microstructure, which was driven by the energy storage of plastic deformation and the reheating thermal cycles. This resembles the previously discussed cold rolling grain size refinement for primary (non-transformable) microstructure alloys.

Li et al. [87], DED-laser + interlayer hot rolling (Fig. 8), observed an intense grain size refinement for the Inconel 718 (Fig. 23). The as-built sample had coarse (~ 113 μm) columnar and oriented grains with a typical cubic texture ({100} < 100 >). In comparison, interlayer hot rolling changed the grain morphology drastically to a fine (~8 μm) equiaxed grain structure. In interlayer hot rolling, it was reported both the dynamic (in situ) and static (reheating thermal cycle) recrystallizations, which refined and randomized the microstructure. Li et al. [87], Fig. 23 b, reveals two regions with different grain sizes (grains in region 1 are larger than those in region 2). In addition, the grain orientation spread (GOS; Fig. 23c) depicted that the grains in region 2 were fresh recrystallized. The grains that formed a layer (i.e., the columnar microstructure) were deformed by interlayer hot rolling. However, the deformation intensity was not homogeneous across the entire layer, where only the top layer surface region was dynamically recrystallized; the remaining grains continues to have stored strain energy that can drive static recrystallization during reheating thermal cycles or heat treatments.

Xie et al. [80] and Liao et al. [162], Al-Mg4.5Mn DEDed-arc, and Zhou et al. [120], AlSi10Mg alloy laser-DEDed, reported that interlayer hot rolling (Fig. 8) and in situ LSP had a lower grain size refinement (from 59 to 23 μm and from 9.8 to 8.6 μm, respectively) effect when compared to Inconel 718 (from 113 to 4.1 μm). Al alloys have a high stacking fault energy (SFE) [163], requiring high deformation to dynamically recrystallize since dislocations can easily reorganize and recovery at elevated temperatures. Therefore, it is expected that high SFE alloys have a lower response to interlayer hot rolling than low SFE alloys due to the low macroscopic deformation and recover processes, which are confirmed by the grain size refinement observed for low SFE alloys (e.g., Inconel 718—grain size from 113 to 4.1 μm, ~ 27 ×) and high SFE ones (e.g., Al-Mg4.5Mn—grain size from 59 to 23 μm, ~ 3 ×). These results indicate that the interlayer hot deformation could be used for specific alloy classes namely solid-state transformable alloys and medium/low SFE non-transformable alloys despite their operational and path planning advantages (see Sect. 2).

3.2 Hammering, peening, and forging

Similar to rolling, the other deposition + interlayer mechanical deformation systems also have their own grain size refinement mechanisms and process characteristics due to the different loading forces and deformation modes. It is important to note that topics addressed in Sect. 3.1 will not be revisited in Sect. 3.2. Instead, they will be referenced.

3.2.1 Transformable solid-state alloys

Hönnige et al. [97], Ti-6Al-4V DEDed-arc, first described the effect of interlayer cold hammer peening on the prior β grain size refinement (Fig. 24). The interlayer hammer

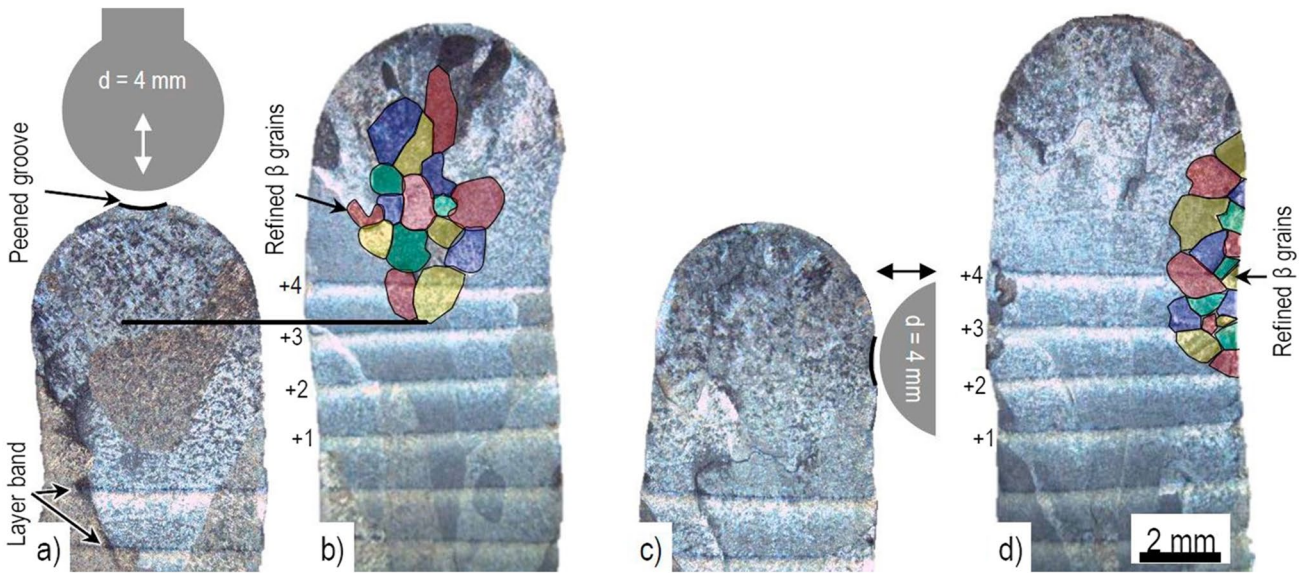

Fig. 24 β grain refinement of interlayer cold hammer peened Ti-6Al-4V WAAM walls (from [97])

peening achieves a pronounced prior β grain size refinement (from ~ 12 to 0.5 mm, ~ 24 ×). In addition, the authors claimed that the refined region is higher than the penetration deformation zone, which indicates that the prior β grains could continue to grow during subsequent thermal cycles. This aligns with the previously observed β grain size refinement mechanisms illustrated in Fig. 19 and reinforces the idea that the new β (β′) consumed the oriented prior β. Furthermore, despite the observed grain size refinement (Fig. 24), the Ti-6Al-4V DEDed-arc + hammer peening grain size is larger than interlayer cold (~ 90 µm) and hot (~ 130 µm) rolled. Hönnige et al. [98] posteriorly detailed the hammer peening grain size refinement mechanism. The depth and distribution of the deformation zone (Fig. 25a) have a steep strain gradient and depth of 2 mm. However, the effective deformation (> 8%) for β refinement is reached only at 0.5 mm, which is lower than the deposition penetration (0.7 mm). These results suggested that the remaining deformed region (dotted black line in Fig. 25a) can also generate β′, which grows during the reheating thermal cycle (Fig. 25b). However, the refined prior β grain layer extends through the remaining deformation and solidification zones, suggesting that the refined prior β grain can grow upwards (epitaxial solidification) and downwards (recrystallization and grain growth into the remaining low deformation region). Thus, recrystallization takes place prior to solidification, i.e., during the heating cycle of the next deposited layer, so that the deposited layer grows epitaxially from these just recrystallized prior β grains.

Hu et al. [164] reported that the α dimensions were similar for DEDed-arc with and without interlayer cold hammer peening, which can be related to the larger prior β grain size compared to cold and hot rolling. However, Yi et al. [37] and Shchitsyn et al. [102] (Fig. 12) observed that the interlayer cold hammer peening reduced the α grain boundary content and α lath size, which proves to be a topic that demands more investigation for a complete consolidation and comprehension. Finally, the hammer peening grain size refinement mechanism is almost similar to cold rolling (twinned β′ growth [149, 150]; Fig. 19), diverging by the presence of a solidification process and lower deformation zone depth, which results in larger grain size in relation to interlayer cold and hot rolling.

The use of interlayer hot peening/forging for solid-state transformation alloys is still scarce due to its dynamic and localized energy characteristic, which can fracture the just deposited layer (hot material). Ye et al. [108], Ti-4Al-6V DEDed-laser + interlayer hot ultrasonic micro-forging (Fig. 28), observed a slight prior β grain size refinement (from ~ 400 to ~ 320 µm); however, these data are statistically equal (large standard error). As proposed by Li et al. [109], the prior β grain size refinement was attributed to the synergistic effect of vibration inducing CET and some dynamic recrystallized β grains (bead surface). Ye et al. [108] verified the dynamic recrystallization by the serrated grain boundaries (strain gradient) and the new β grains formed at a triple junction (high local strain regions). In addition, these new β grains can grow down and consume

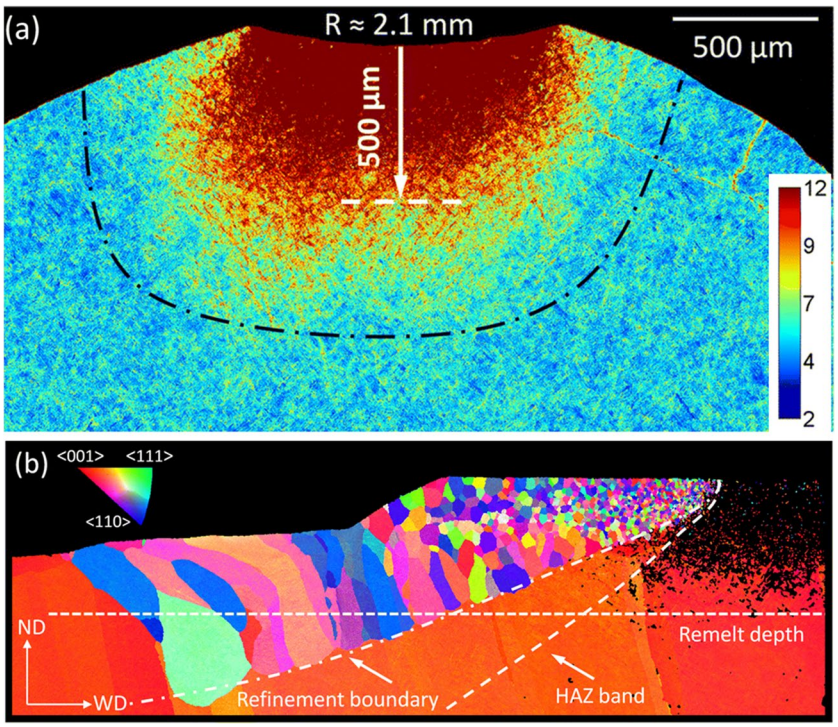

Fig. 25 **a** Strain distribution map and **b** an β grain reconstruction EBSD map and interaction of thermal cycle with the deformed region (from [98])

the columnar β grains, similar to that observed for cold hammer peening [98]. Xiong et al. [110], low-alloy steel (AWS ER70S-6) DEDed-laser + interlayer hot hammer peening, also observed the parent phase (γ) dynamic recrystallization at the layer surface; however, due to the γ → α transformation, the final microstructure is not significantly affected. Although the prior γ grain size affects material hardenability and α formation/morphology, the mandatory effect on the final microstructure is governed by the cooling rates [165], which is almost insensible to the interlayer hot hammer (low effect on geometric aspects of the deposited layer) [110]. Thus, the interlayer hot hammer peening for transformable alloys showed insufficient grain refinement that justified its use.

3.2.2 Non-transformable solid-state alloys

Wang and Shi [105, 106], Inconel 718 DEDed-laser + interlayer cold hammer peening, highlighted that the major effect of interlayer cold hammer occurred on the interlayer regions (fusion line) and was related to an equiaxed dendrite zone (~ 200 µm) between the previously interlayer deformed and subsequently deposited layers (Fig. 26). Inconel 718 DEDed-laser microstructure had typical coarse and oriented

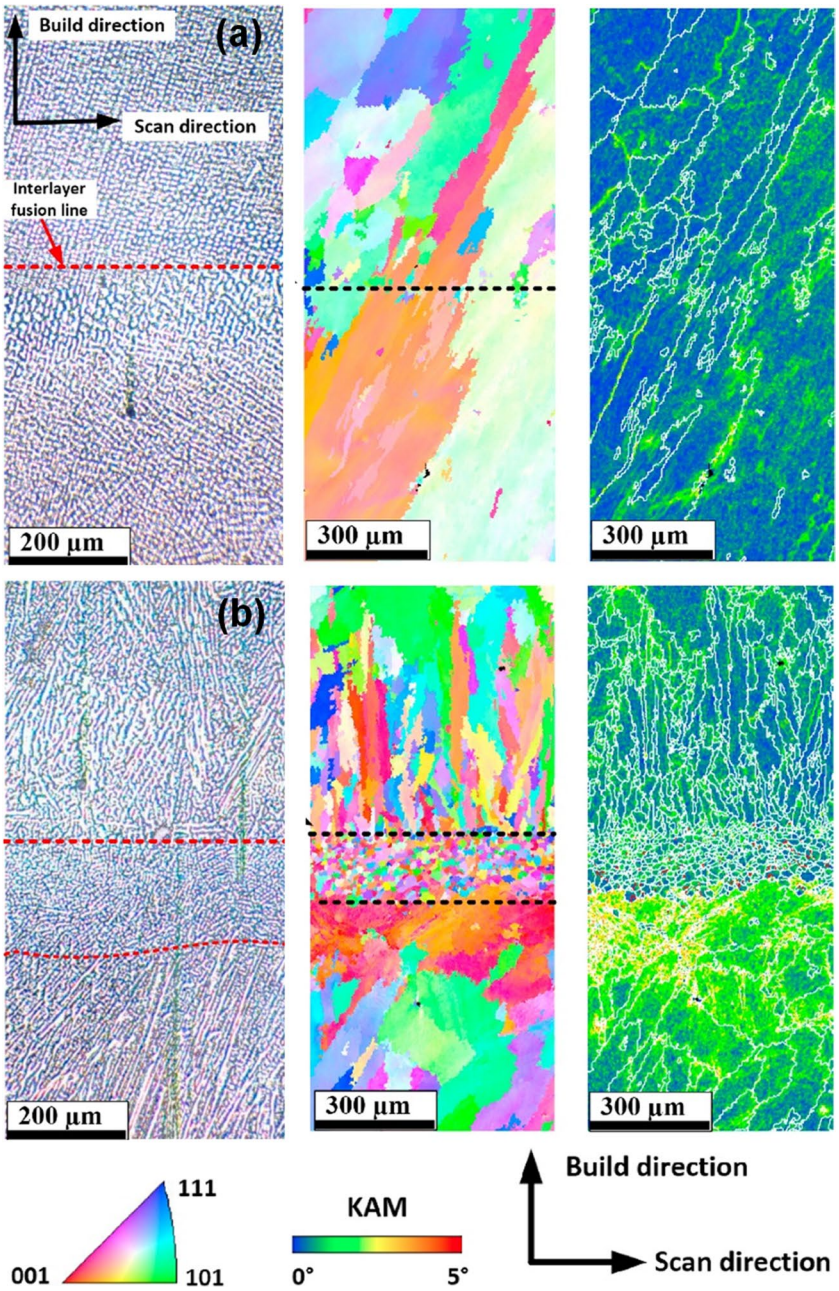

Fig. 26 Optical microscopy, orientation map, and kernel average misorientation (KAM) map: **a** Inconel 718 DEDed-laser and **b** Inconel 718 DEDed-laser + interlayer cold hammer peening (adapted from [106])

primary grains. Interlayer cold deformation generated a fine equiaxed grain size (~ 10 µm) band, which prevents continuous primary grains across several layers (Fig. 26); however, the epitaxy persisted. Thus, the next layer will use the previously refined grains as a nucleation site, as suggested by Hönnige et al. [98] for DEDed-arc Ti-6Al-4V + interlayer cold hammer peened. Besides, the deformed region (intense kernel average orientation—KAM), which must be higher than the melting pool penetration (0.1–0.5 mm for laser-based DED), can drive static recrystallization during post-deposition heat treatment (e.g., mandatory for Inconel 718) or reheating thermal cycles. Thus, similar to observed in cold rolling, non-transformable medium/low SFE alloys can undergo two grain refinement mechanisms when interlayer cold hammered: static recrystallization during deposition and subsequent heat treatment. In addition, Parvaresh et al. [166] observed grain refinement due to interlayer cold hammer peening for an AISI 347 stainless steel, which aligns with the findings proposed by Wang and Shi [105, 106].

As opposed to Wang and Shi [105, 106] (DED-laser), Fang et al. [101] (DED-arc + interlayer cold hammering) deposited the 2319 Al alloy, which required an intense and deeper deformation (high SFE alloy and arc-based process) to induce static recrystallization by the reheating thermal cycle. The primary grains of the 2319 Al alloy are mostly equiaxed, with a small number of columnar grains close to the substrate (high thermal gradient; Fig. 27). As detailed in Fig. 27, region A shows an intense deformation after hammering and had a fine grain size (1.3 µm), which transformed into region B (reheating thermal cycle), characterized by static recrystallization and grain growth (~ 9 µm). Region C depicts the deformation depth of hammering (~ 2 mm), which was also characterized by static recrystallization; the other regions, closer to the substrate, were not affected by the hammering. Thus, the subsequent deposition + deformation cycles will reproduce this refined microstructure throughout, which proves the efficiency of hammering to refine the as-built microstructure of high SFE alloys (e.g., Al-based).

Duarte et al. [20] (AISI 316L stainless steel) demonstrated the grain size refinement of the DEDed-arc + interlayer hot forging (Fig. 13) using 2D Debbye-Scherrer diffraction patterns obtained via synchrotron X-ray diffraction; however, the authors did not investigate the phenomena that governed the grain size refinement. In addition, Duarte et al. [20] observed the increase in the cooling rate due to the higher bead width after the hot deformation, which promoted a finer primary microstructure (e.g., cellular and dendritic). Farias et al. [111, 112] clarified the grain refinement mechanisms of the DEDed-arc + interlayer hot forging (Fig. 13). The authors [111, 112], using in situ electron X-ray diffraction, reported that interlayer hot forging could generate enough crystal defects to induce static recrystallization during subsequent thermal cycles and post-deposition heat

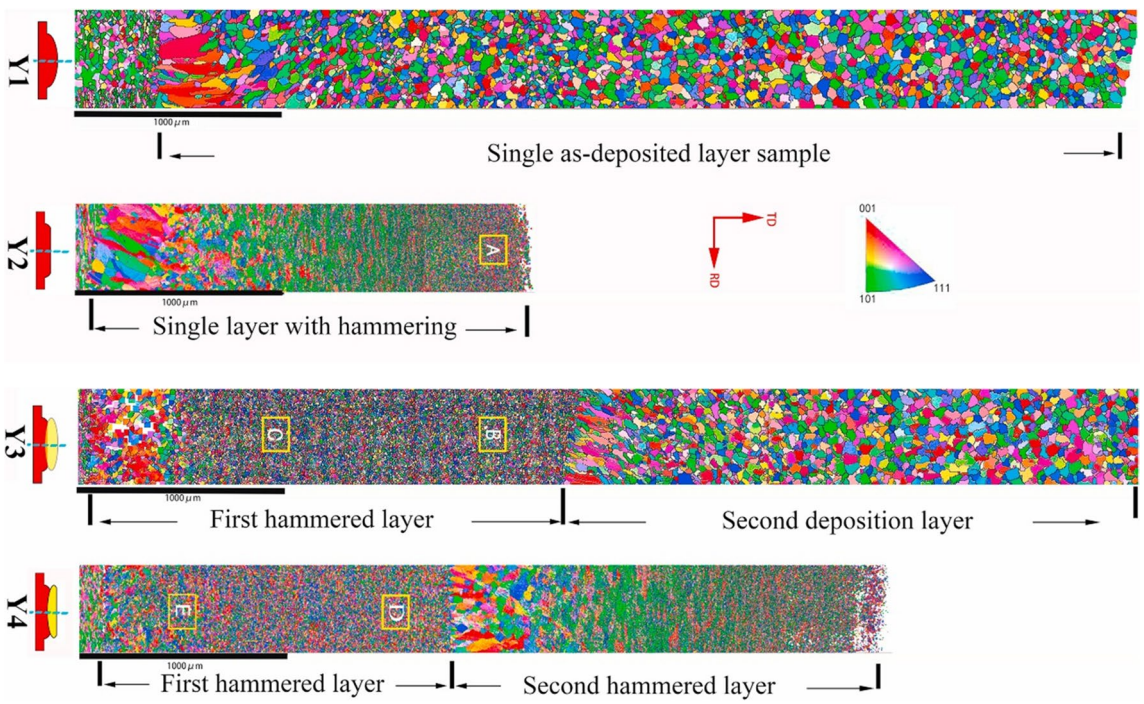

Fig. 27 Microstructure evolution of 2319 Al DEDed-arc + interlayer cold hammering. Single-layer + hammering; two-layers + hammering on the first layer. (a), (b), (c) IPF-EBSD maps of the areas A, B, and C, respectively (adapted from [101])

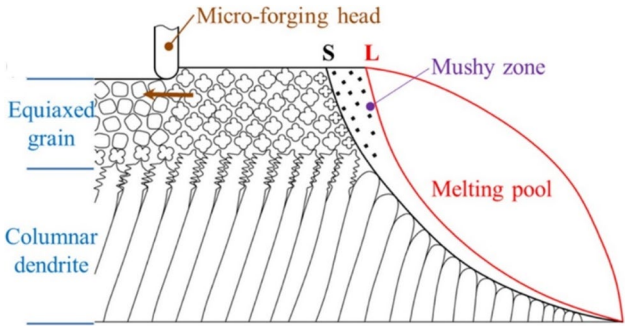

Fig. 28 Schematic illustration of the effect of DED-laser + interlayer hot deformation on microstructure (from [109])

treatments. Li et al. [109], Ni-based superalloy (GH3039) DEDed-laser, reported that the interlayer hot ultrasonic micro-forging did not alter the typical columnar and oriented grains, which is mainly controlled by heat transfer aspects during part building. Additionally, Li et al. [109] highlighted that the CET depth, which is related to dynamic recrystallization, increased from 440 to 840 µm, which indicates that the interlayer hot ultrasonic micro-forging recrystallized the CET grains (Fig. 28). In addition, the vibrations (forging strokes) also enhance the CET length [167]. Thus, hot forging can have two simultaneous grain refinements: enhancing the CET due to its dynamic aspect (inducing vibration on the liquid) and dynamic and static recrystallization (solid-state).

Figure 28 also indicates that the heat source-deformation distance could be a limiting factor since some materials can lose the ductility at higher temperatures, leading to cracking due to the intense and localized hot forging deformation, which explains the major use of the hammer and ultrasonic peening in cold conditions or with high heat source-deformation distance (far from the mushy zone). Hence, there is a minimum distance that is sufficient to stay out of the brittle temperature range [168] and a maximum distance (minimum temperature to drive dynamic recrystallization—hot deformation—or minimum temperature to ensure sufficient deformation for static recrystallization—cold deformation). For solid-state transformable alloys, the hot deformation must occur at a temperature superior to the transition temperature (e.g., β *transus* and austenite decomposition) to induce an effective dynamic recrystallization of the parent phase (grain size refinement), establishing a minimum deformation temperature. Additionally, each alloy possesses specific physical properties (e.g., thermal conductivity and density) and metallurgical behavior (e.g., recrystallization temperature and strength at elevated temperatures). Consequently, the combination of each material, DED process, and deformation system is almost unique. Therefore, parameter optimization should consider the stability of the deposition process, layer geometrical aspects (particularly penetration and width), and deformation parameters (heat source-deformation tool distance and deformation zone depth). This ensures that deposition + interlayer deformation effectively promotes grain size refinement and improves material behavior without compromising printability (e.g., instability, layer malformation, hot cracks, and lack of fusion).

4 Effects of deposition + interlayer deformation on material mechanical behavior

A critical problem that can prevent the industrial scalability of DED processes relates to the poor mechanical properties of the part 3D printed. This included the inability to meet material specifications (e.g., API 20S and AMS 5662) and inferior performance compared to conventional manufacturing routes (e.g., wrought). In this context, Sect. 4 evaluates the effect of interlayer mechanical deformation on the mechanical properties of typical commercial alloys deposited via DED, comparing them with the standard industrial requirements and discussing the changes in mechanical properties based on Sect. 3 (grain size refinement mechanisms).

4.1 Ti-based alloys

Martina et al. [169] (Ti-6Al-4V) first showed that the DED-arc + interlayer cold rolling improved both the yield strength (σ_{YS}) and ultimate tensile strength (σ_{UTS}) in both deposition (heat source path planning) and building (perpendicular to heat source path planning) directions; however, a slight drop in ductility was observed in relation to DEDed-arc. Further, Colegrove et al. [19] highlighted that Ti6Al4V DEDed-arc anisotropy, especially concerning the material ductility, was virtually eliminated by interlayer cold rolling. Figure 29 depicts the influence of interlayer mechanical deformation on the quasi-static mechanical properties of the Ti6Al4V DEDed, comparing the data from literature and ASTM B265 requirements. It is worth noting that the interlayer deformation systems (hot and cold rolling and cold peening) did meet the ASTM B265 (wrought Ti-6Al-4V) and AMS 4999 (additive manufactured Ti-6Al-4V) requirements, which was not observed for the DEDed condition.

Yang et al. [170] (Ti6Al4V DEDed-arc) and Chi et al. [171] (Ti17 alloy DEDed-arc) showed that the interlayer cold ultrasonic and LSP, respectively, can improve both σ_{YS} and σ_{UTS} without affecting the ductility. Further, Huang et al. [172] highlighted that the finer prior β grain size reduced the allotriomorphic α content at the grain boundary, which can even increase the Ti-6Al-4V DEDed-arc ductility. These results are contrary to Yi et al. [37] and Martina et al. [169], both Ti6Al4V DEDed-arc, which observed an increase in the obtained σ_{YS} and σ_{UTS} and a reduction in ductility due to the interlayer mechanical deformation. Besides, Tian et al. [88]

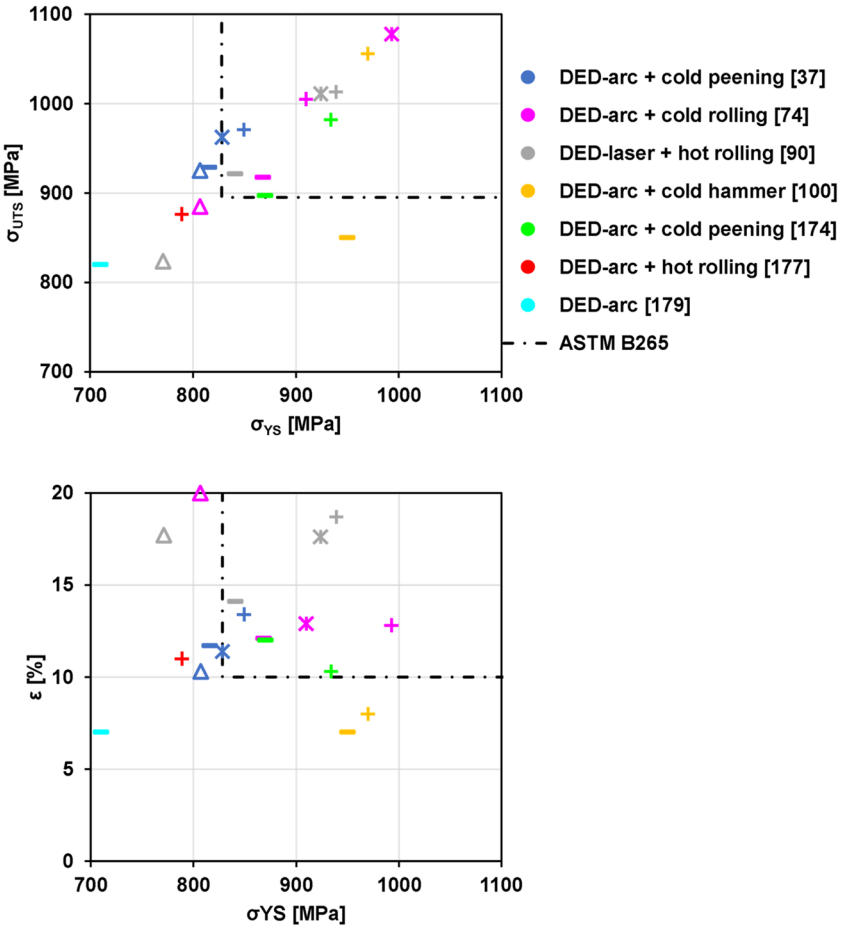

Fig. 29 Tensile properties of Ti-6Al-4V deposited by DED-arc + interlayer mechanical deformation. The symbols ▬, ▲, +, and ∗ mean that the tensile specimens were taken from the DEDed part in the deposition direction (heat source path), built direction (90° from heat source path), interlayer mechanically deformed DEDed deposition direction, and interlayer mechanically deformed DEDed built direction, respectively

and Hu et al. [173], Ti6Al4V DEDed-laser and DEDed-arc, respectively, reported that the interlayer hot rolling induced an isotropic behavior and increased σ_{YS}, σ_{UTS}, and ductility.

Colegrove et al. [19] pointed out that the coarse and oriented prior β grain (DEDed-arc condition) induced the formation of aligned allotriomorph α-phase (soft region) at the prior β grain boundary, which had faster loading damage (i.e., strain accumulation and crack nucleation) than the Widmanstaätten interlocked α-phase matrix [174]. Thus, it is expected that the prior β grain refinement induced by the interlayer mechanical deformation enhanced the ductility; however, as depicted in Fig. 30, Yi et al. [37] and Martina et al. [169] observed a decrease in ductility even considering the β grain refinement, which was associated with remaining deformation (higher dislocation density and increased work hardening). In addition, Bermingham et al. [175] reported that the smaller α colony size (i.e., basketweave microstructure), due to refined prior β grain, can reduce material ductility due to the difference in mechanical properties of the prior β grain (α colonies) and grain

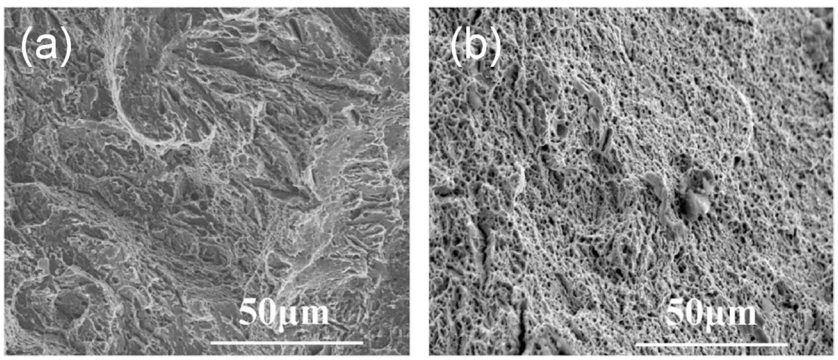

Fig. 30 Fracture surface of a bainitic still deposited by DED-arc: **a** without and **b** with interlayer hot rolling (adapted from [78])

boundary (allotriomorph α-phase). Hu et al. [173] correlated the lower ductility with the increase in the work hardening exponent due to the smaller prior β grain. Thus, considering that cold and hot interlayer deformation induced a finer prior β grain and smaller α colony size, the main difference between them is the remaining deformation (especially associated with deformation depth), which induced a lower ductility for DEDed + interlayer cold deformation concerning DEDed + interlayer hot deformation. This statement is corroborated by Tian et al. [88], who calculated the dislocation density for Ti-6Al-4V DED-laser and DED-laser hot rolling conditions, concluding that, due to the high-temperature deformation, these conditions had similar dislocation densities. In addition, the higher hardness and σ_{UTS} of the cold deformed condition reinforce the conclusion that its low ductility arose from the remaining deformation. Despite the lower ductility, cold deformation still ensures that the Ti-6Al-4V DEDed meets the standards and code requirements.

The increase in σ_{YS} and σ_{UTS} was usually associated with a finer α lath size; however, most of the literature [19, 88, 102, 170, 173] indicated that the interlayer deformation had a low effect on α lath size. Tian et al. [88] stated that the predominant factors for the increase in σ_{YS} and σ_{UTS} were related to the randomization and refinement of the prior β grain (from coarser and aligned to equiaxial), which also reduce the variant selection in the $\beta \rightarrow \alpha$ phase transformation and α phase texture index. Lütjering [176] reported that, for (α + β) titanium alloys, the α colony and α lath size dictated the slip length. Thus, as the α lath size is less affected by the interlayer deformation, the α colony size was mainly responsible for the increase in σ_{YS} and σ_{UTS} in relation to DEDed. Finally, the literature data converge (Fig. 30) on the conclusion that both cold and hot deformation systems improved the σ_{YS} and σ_{UTS} of the Ti-6Al-4V DEDed, enabling it to meet the material specifications.

4.2 Low-alloy steels

Colegrove et al. [31] first studied the effect of interlayer cold rolling on low-alloy steel (AWS A5.18 ER70S-6) DEDed-arc. The authors showed that the final microstructure (e.g., grain boundary ferrite and acicular ferrite) was not strongly influenced by the cold rolling. However, the remaining deformation (Taylor hardening) increased and homogenized the hardness profile so that a higher load rolling induced a higher hardness, which also converged to the Ti6Al4V alloy DEDed + interlayer mechanical deformation results [19, 88, 102, 170, 173]. Posteriorly, Dirisu et al. [68] carried out tensile tests (Table 1) that corroborated Colegrove et al. [31], showing that the σ_{UTS} and σ_{YS} were improved with the rolling load. Thus, for low-alloy steel DEDed + interlayer cold deformation, the major hardening mechanism was attributed to the increase in dislocation density (Taylor hardening), which was confirmed by Dirisu et al. [68] via transmission electron microscopy. In addition, the authors observed a finer ferrite grain size for a higher load rolling (160 kN; 14.5 vs. 8.6 µm), which improved the total strengthen (Hall–Petch). Similar to Ti-6Al-4V, the final microstructure of low-alloy steels arise from solid-state transformation so that the product phase (ferrite) and its constituents are less affected by the interlayer deformation, reinforcing the results of Colegrove et al. [31]. Ma et al. [81] (DED-arc + interlayer hot rolling) and Xiong et al. [177] (DED-arc + interlayer hot forging) also observed (Table 2) an improvement in mechanical properties with an almost isotropic behavior, which met the ASTM A182-19 standard. It is worth noting that both Dirisu et al. [68] and Ma et al. [81] (Table 2) observed a significant prior austenite grain size refinement and an increase in σ_{UTS} and σ_{YS}. However, due to the higher remaining deformation (high dislocation density), DEDed + interlayer cold rolling (160 kN) [68] induced a drop in ductility, which was associated with work hardening.

Table 1 Static tensile properties of a low-alloy steel (AWS A5.18 ER70S-6) DEDed-arc (adapted from [68])

Rolling load [kN]	σ_{UTS} [MPa]	σ_{YS} [MPa]	Hardness $HV_{0.2}$	Ductility [%]
0	402 ± 2.0	300 ± 1.5	186 ± 2.0	28 ± 1
50	552 ± 1.0	498 ± 5.0	225 ± 1.0	25 ± 2
75	546 ± 3.0	486 ± 2.6	219 ± 1.5	32 ± 2
160	600 ± 3.0	574 ± 2.6	233 ± 1.5	22 ± 2

Fu et al. [78] (Fig. 7) verified the increase in ductility due to hot rolling for bainite steel (Table 2). In addition, these authors addressed the Charpy V-notch (CVN) impact energy absorbed. The interlayer hot rolling strongly increased the CVN impact energy (99 J/cm^2—three times higher than DEDed-arc) in relation to both DEDed-arc and wrought material; the CVN impact energy had an isotropic behavior. Figure 30 shows that the interlayer hot forging induced a change in fracture mechanism from almost cleavage (brittle) to fine dimples (ductile) aspect. This behavior was directly related to the finer prior austenite grain size developed during hot rolling, which induced a finer sub-structure (packet and blocks) and effective grain size [178] (similar to α colony size in Ti-6Al-4V) and reduced the grain boundary ferrite and martensite-austenite microconstituent (both brittle) [179], which enhanced the CVN impact energy.

4.3 Stainless steels

The AISI 316 L stainless steel DEDed (both laser and arc) usually met the materials' specification (ASTM A240) in the as-built condition; however, as pointed out by Wang et al.

Table 2 Effect of the interlayer deformation on low-alloy steel DEDed quasi-static mechanical properties

DED	Deformation		Feedstock material	σ_{YS} [MPa]	σ_{UTS} [MPa]	ε [%]	References
	Process	Temperature					
Arc	Rolling	Cold	ER70s-6	574 ± 2.6	600 ± 3.0	22 ± 2	[68]
	—	—		300 ± 1.5	402 ± 2.0	28 ± 1	
Arc	Rolling	Hot	ER70s-6	387.8	530.9	36.9	[81]
	—	—		365.1	509.3	37.3	
Arc	Forging	Hot	ER70s-6	641.9	529.3	37.3	[177]
	—	—		297.4	469.6	42.2	
Arc	Rolling	Hot	Bainitic steel	1259.1	—	17.0	[78]
	—	—		1275.3	—	10.8	

Table 3 Tensile properties of AISI 316L stainless steel DEDed + interlayer deformation

DED process	Deformation		σ_{YS} [MPa]	σ_{UTS} [MPa]	Ductility [%]	References
	Process	Temperature				
arc	Forging	Hot	450	622	27.9	[20]
	—	—	360	574	32.5	
laser	Forming	Hot	254	597	65.2	[113]
	—	—	279	611	59	
arc	Rolling	Hot	340 ± 3	591 ± 4	38 ± 5	[181]
	—	—	265 ± 11	534 ± 4	49 ± 4	
ASTM A240			170	485	40	
ASTM A666 1/16 hard hot finished			310	585	35	
ASTM A666 1/8 hard cold finished			380	690	25	

[180], the as-built columnar microstructure results in an anisotropic behavior. In this sense, Duarte et al. [20] (DED-arc), Gao et al. [113] (DED-laser), and Kan et al. [181] (DED-arc) reported (Table 3) an improvement in the mechanical properties and an isotropic behavior due to the interlayer hot deformation. Duarte et al. [20] and Kan et al. [181] observed that the hot forging and rolling, respectively, increased both σ_{YS} and σ_{UTS} (meet the ASTM A240 and ASTM A666 1/16 hard), which was associated with the finer grain size and the increase in the work hardening; in addition, these authors [20, 181] associated the drop in ductility with the finer grain size, not meeting the ductility requirements (ASTM A240 and ASTM A666).

Parvaresh et al. [166] imposed a macroscopic interlayer cold deformation (similar to the pressing process) to the AISI 347 stainless steel DED-arc. As in the case of hot deformation systems [20, 113, 181], Parvaresh et al. [166] reported an increase in material strength (σ_{UTS}, from 576 to 803 MPa and σ_{YS}, from 395 to 697 MPa) at the expense of ductility (from 58 to 30%). Diao et al. [182], AISI 321 stainless steel DEDed-arc, verified that interlayer ultrasonic peening induced a finer γ grain size, which increased the σ_{YS} (from ~ 390 to ~ 425 MPa) and did not alter ductility. Finally, although the interlayer deformation improved the strength of stainless steel, the low ductility problem persists, which is aggravated by the interlayer deformation. Thus, for alloys fabricated via DED that typically meet the strength requirements and fail in plasticity ones, interlayer deformation can be inefficient since the grain size refinement increases the work hardening exponent (Hollomon's equation).

Xu et al. [183] reported that the maraging steel (AISI Grade 18Ni 250) DEDed-arc had an inadequate heat treatment response, resulting in an inferior σ_{YS} (1270 MPa vs. 1720 MPa) concerning wrought material, which makes its industrial adoption unfeasible. Posteriorly, the same research group (Xu et al. [152]) observed that interlayer cold rolling (50 and 75 kN) promoted a significant improvement in the heat treatment response, which resulted in a substantial increase in σ_{YS} and σ_{UTS} (Fig. 31) concerning DEDed-arc condition (σ_{UTS} from 1735 to 1345); however, the material requirements (ASTM A579) were also not met. Xu et al. [152] pointed out that the interlayer rolling induced an intense prior austenite grain size refinement (from primary microstructure—~ 200 µm—to equiaxed—40 µm), enhancing the length of high-angle grain boundaries and increasing the dislocation density, which strongly increases the atomic mobility during solubilization heat treatment (i.e., more solute is supersaturated in the martensite matrix). In addition, the higher dislocation density acts as precipitate nucleation site; thus, during aging, a higher content of hardening phase precipitated (1.4 vs. 2.2%), which explained the significant

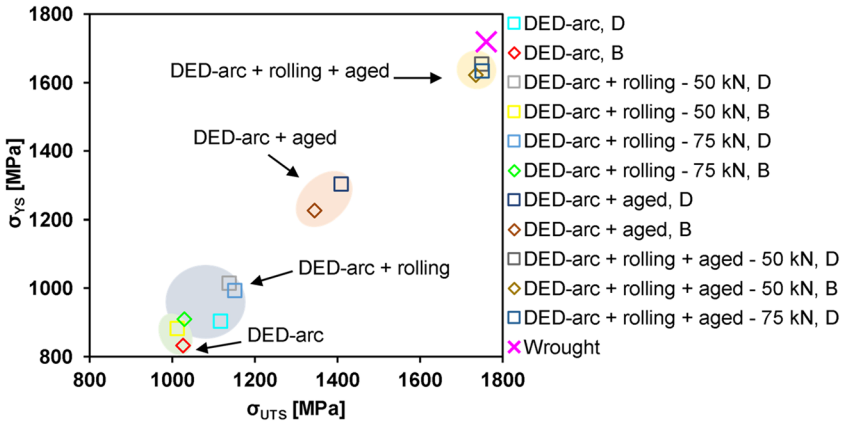

Fig. 31 Mechanical properties of the maraging steel DEDed (from Xu et al. [152]). B and D are the building and deposition directions, respectively

improvement in the heat treatment response due to the interlayer cold rolling.

4.4 Ni-based alloys

Ni-based superalloys (non-transformable solid-states) fabricated via arc plasma DED typically did not meet the material specification (e.g., AMS 5662 and ASTM B670 standards) in the as-built and post-deposition heat-treated conditions, especially the Inconel 718 (a high-responsibility alloy used in the aerospace industry). This behavior was primarily related to coarse microstructure, intense interdendritic segregation (e.g., Nb and Mo), and deleterious eutectics precipitation (e.g., Laves phase and MC-type carbides), which reduced the material response to heat treatment (e.g., precipitation of γ″ and γ′ phases) [156]. In this sense, Xu et al. [89] observed (Table 4) that the interlayer cold rolling can satisfactorily enhance the mechanical properties of the Inconel 718 DEDed-arc, meeting, for the first time, the AMS 5662 requirements. Given that the Laves phase consumes the Nb and reduces the γ″ and γ′ content and that the interlayer rolling has a low influence on solidification conditions, the solution heat treatment (~980 °C) is not able to increase the γ″ and γ′ content (Laves phase dissolution temperature—1146 °C), explaining the almost similar aging response of the DEDed and DEDed interlayer rolled samples (321 and 391 MPa, respectively). Thus, the main difference between the rolled and unrolled DEDed-arc Inconel 718 mechanical properties rise from the grain size (1200 vs. 15.7 µm; Fig. 20) strengthening mechanism. The difference in σ_{UTS} (295 MPa), 225 MPa (76%) is attributed to grain size refinement; 70 MPa (24%) is related to improvement in the material response to heat treatment. Therefore, the grain size refinement of Inconel 718 DEDed was critical for the material to meet the AMS 5662 requirements. Similar results were posteriorly obtained by Zhang et al. [158], which verified that the rolling force (50 and 75 kN) did not influence the quasi-static properties since the final grain size is almost similar (26.5 and 14.7 µm, respectively).

A similar tendency (increase the rolling temperature to improve the grain size refinement) was also observed by Chen et al. [184] and Li et al. [87], DED + interlayer hot rolling (Figs. 5 and 8, respectively), who obtained a finer grain size (~25 µm [184] and 8 µm [87]). Besides, Chen et al. [184] reported that the obtained mechanical properties met the AMS 5662 standard requirements in deposition and building directions. Wang and Shi [106], DED-laser, also pointed out better properties due to interlayer deformation (cold ultrasonic harmer peening); besides, the material (σ_{YS} and σ_{UTS} of 1037 and 1276 MPa, respectively) met the AMS 5662 requirements. Figure 32 summarizes the abovementioned works and compares them with the material specification, where it is possible to infer that the interlayer deformation can significantly increase

Table 4 Mechanical testing results of the DEDed-arc interlayer cold (un)rolled Inconel 718 (adapted from [89]). AD and SA correspond to as-deposited and solution + aging heat-treated, respectively

Condition		σ_{UTS} [MPa]			σ_{YS} [MPa]		Ductility [%]		AMS 5662
		H	*V*	Average	*H*	*V*	*H*	*V*	
AD	Unrolled	818 ± 13	756 ± 7	793 ± 32	525 ± 7	506 ± 2	33.3 ± 2.5	27.9 ± 1.3	×
	rolled	1082 ± 13	1072 ± 6	1078 ± 12	763 ± 8	687 ± 1	26.2 ± 2.2	26.6 ± 1.3	×
SA	Unrolled	1102 ± 78	988 ± 6	1056 ± 82	790 ± 9	791 ± 14	14.7 ± 1.3	12.8 ± 1.2	×
	rolled	1348 ± 10	1356 ± 10	1351 ± 11	1057 ± 19	1035 ± 20	15.1 ± 3.3	17.4 ± 1.1	✓

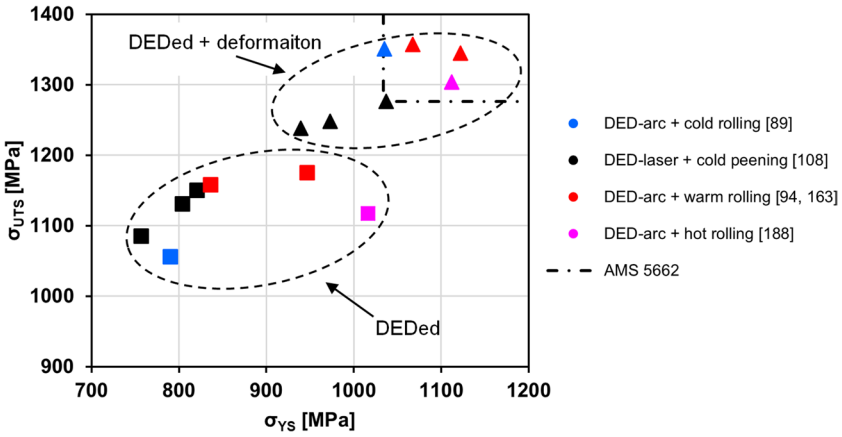

Fig. 32 Effect of the interlayer deformation on Inconel 718 DEDed yield (σ_{YS}) and ultimate tensile (σ_{UTS}) strength. Materials after post-deposition heat treatment

the performance of the Inconel 718 DEDed. In addition, the tensile properties of Inconel 718 at elevated temperatures (649 °C) must also be considered for high-temperature applications, such as jet turbine blades and the nuclear industry [157]. In this scenario, only the warm rolling material [92, 158, 185] met the AMS 5662 requirements despite all DED + deformation conditions also improving the material properties concerning DED.

Zhao et al. [79] (Ni60 alloy) and Li et al. [109] (GH3039 alloy) deposited solid-solution strengthened Ni-based alloys and observed the effects of interlayer hot deformation (rolling and forging, respectively) on the hardness profile (Fig. 33). The authors pointed out a banded hardness pattern related to the fine cellular microstructure close to the fusion line (peak hardness) and the coarse columnar dendritic (lower hardness) far from the fusion line. Using the deposition + interlayer mechanical deformation, the hardness profile became more homogeneous and average hardness increase. Zhao et al. [79] and Li et al. [109] associated the hardness increase with grain size refinement (Hall–Petch) and higher dislocation density (Taylor hardening).

4.5 Al-based alloys

Fang et al. [101], Gu et al. [160], and Wang et al. [186] evaluated the effect of the interlayer cold deformation (hammering and rolling) on quasi-static mechanical properties of the 2319 Al DEDed-arc (Table 5). Fang et al. [101] reported that interlayer hammering increased the σ_{YS} and σ_{UTS} by 50.8% and 16.0% (238.9 and 332.8 MPa, respectively) in comparison to the un-hammered DEDed-arc in the as-built condition, which is followed by a reduction in ductility (from 18.1 to 13%), i.e., there is a trade-off between the increase in σ_{YS} and σ_{UTS} and the reduction in ductility, which was also observed by Gu et al. [160]. Further, despite the grain refinement (~9 µm vs. 89 µm [101] and 26.7 µm and 7.7 µm [160]) induced by the reheating static recrystallization, the authors [101, 160] reported that the grain boundary strengthening (~5 MPa) was negligible compared to the actual increase in material strength (~100 MPa). Thus, the

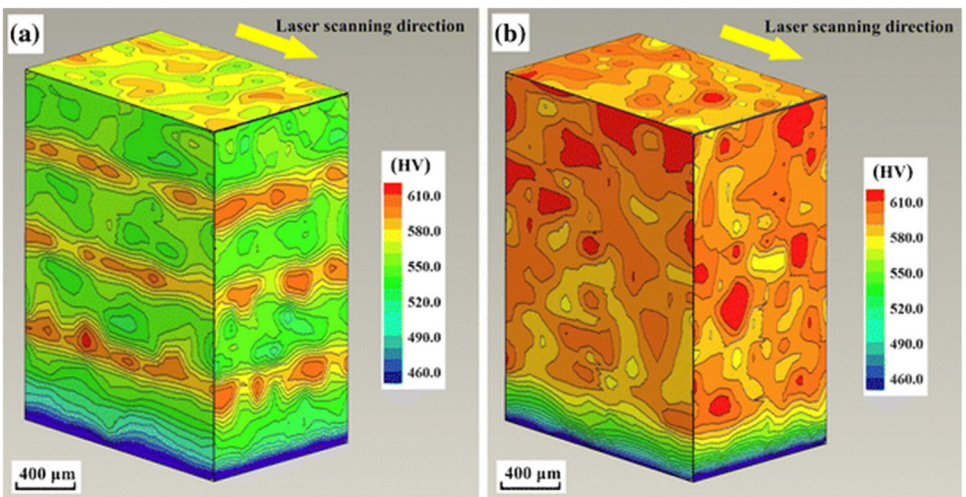

Fig. 33 Vickers microhardness contour maps of Ni60 alloy **a** unrolled and **b** rolled DED-laser (from [79])

Table 5 Effect of interlayer mechanical deformation on the 2319 Al alloy DEDed quasi-static mechanical properties

DED	Deformation		Condition	σ_{YS} [MPa]	σ_{UTS} [MPa]	ε [%]	References
Process	Process	Temperature					
Arc	Hammer	Cold	As-built	238.9	332.8	13	[101]
	—	—		148.5	289.2	18.1	
Arc	Ultrasonic peening	Cold	As-built	114	255	5.6	[186]
				64	224.5	8.1	
Arc	Rolling	Cold	As-built	247.5	319.8	8.5	[160]
	—	—		133.3	261.6	18.4	
	Rolling	Cold	T62	321.2	458.1	17.0	
	—	—		333.9	461.2	14	
Wrought material				290	415	10	[197]

major strengthening (~ 95 MPa) mechanism was associated with the Taylor hardening. However, 2319 Al alloy requires a post-deposition heat treatment to meet the full strength (solution + artificial aging heat treatment; T62) [187]. Gu et al. [160] reported that T62 heat-treated conditions (unrolled and rolled) met the ASTM B 247 requirements and no significant differences are observed among them (e.g., 142 vs. 144 HV, respectively). This behavior arose from the precipitation hardening (main strengthening mechanism) on mechanical properties. As mentioned, the grain size had no significant effect; also, due to the solution heat treatment (535 °C/1.5 h), the Taylor hardening (an increase in the dislocation density) was negligible (recovering and static recrystallization). Therefore, the interlayer mechanical deformation had limitation effect of age-hardened Al alloys fabricated via DED.

Xie et al. [80], Gu et al. [159], and Liao et al. [162] evaluated the behavior of the 5xxx series Al alloy (solid-solution strengthened—not indicated post-deposition heat treatment). Gu et al. [159] reported that the high-density dislocations (sub-structures and low-angle grain boundaries) and the finer grain size are the main strengthening mechanisms of the 5087 aluminum alloy DEDed-arc + interlayer cold rolling. Furthermore, the material strength (σ_{YS}, σ_{UTS}, and hardness) increased almost linearly with the rolling load, which is related to the final grain size and work hardening (Hall–Petch relation; Fig. 34a). Xie et al. [80] and Liao et al. [162] (Fig. 34b) pointed out that the effect of interlayer hot rolling on the 5087 aluminum alloy DEDed-arc strength (σ_{YS} and σ_{UTS}) is almost insignificant; however, an increase in ductility (from 17 to 22%) was observed due to the finer grain size (59 vs. 23 µm) and pore closure effect [120]. As previously mentioned, Al alloys had a high SFE energy, which is favorable for recovery during high-temperature deformation; thus, the deposition + hot deformation did not show appreciable improvement in the quasi-static mechanical properties of 5xxx series aluminum alloy, despite inducing a fine grain size. In addition, for interlayer cold rolling, material strength increases due to high-density dislocation, a common mechanism of work-hardened alloys (e.g., 5xxx Al) [188]. Therefore, considering the results of the 2xxx ([101, 160]) and 5xxx [80, 159, 162] series aluminum alloys, the

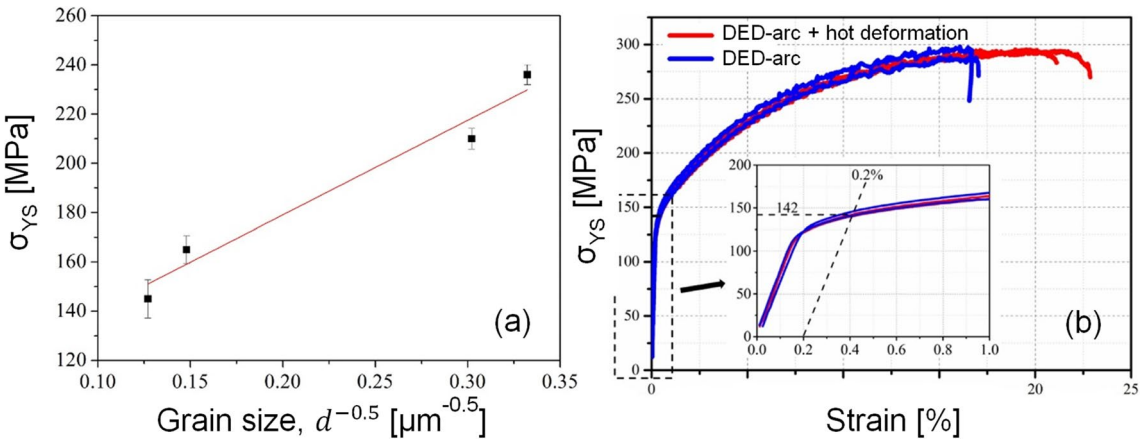

Fig. 34 **a** Hall–Petch relationship between the yield stress and the grain size ($d^{-0.5}$ [µm$^{-.0.5}$]; adapted from [159]) and **b** stress–strain curve for the aluminum alloy 5087 (hot rolled and unrolled; adapted from [80])

interlayer mechanical deformation did not show significant results and efficiency.

5 Summary and outlooks

The present study described the coupled deposition and interlayer mechanical deformation systems and its effects on the microstructure (grain refining mechanism) and mechanical properties of commercial alloys typically additively manufactured. Figure 35 depicts the main interlayer deformation systems, which can be classified by the deformation temperature (cold and hot) and the deformation type (rolling and peening/hammering/forging). It is worth noting that rolling is a unique deformation process executed under a wide range of temperatures, as indicated by Martina et al. [169] (cold, 25–150 °C), Zhang et al. [92, 158, 185] (warm, ~ 450 °C), and Zhang et al. [32] (hot, > 900 °C). Peening and hammering were adopted in the vast majority of cases in cold deformation conditions, while forging is commonly used in a hot deformation condition [111]. The deformation temperature was directly related to the interlayer deformation system; for example, rolling can use higher loading forces (up to 160 kN) [68], which allowed it to be used at different temperatures (hot, warm, and cold). In addition, interlayer rolling can deform the deposited layer without making it unfeasible for the deposition of the subsequent layer due to its quasi-static and unlocalized deformation behavior, i.e., interlayer rolling did not drastically alter the layer geometry and induce defects. Peening and hammering, due to their dynamic characteristics (high frequency and localized energy) and local deformation [37, 107], were preferred for cold conditions because the intense localized deformation can induce, in hot deformation conditions, material spatter, cracks, and/or drastically alter the layer surface. Forging also had these dynamics characteristics; however, it used low frequencies and had a high deformation zone [21], which allowed it to be used in hot conditions.

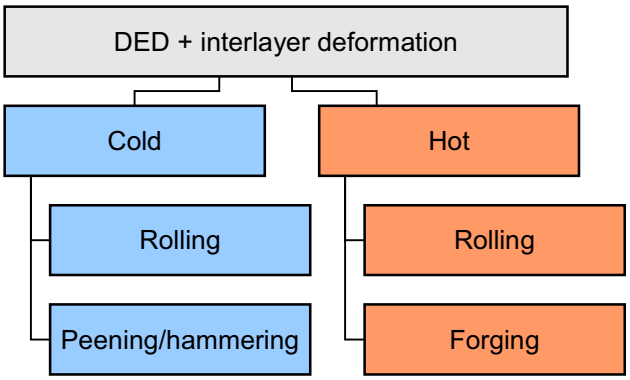

Fig. 35 Interlayer mechanical deformation systems classification

The cold or hot interlayer mechanical deformation systems had advantages and limitations (Fig. 36) that could hinder industrial adoption. As previously announced, cold rolling requires higher rolling loads, demanding robust equipment [169, 189]. Cold peening and hammering, due to their dynamic character, do not require massive and dedicated equipment, being, for instance, manually operated for multi-pass arc-welded joints [190], which also allows their robotization (free path planning). In addition, cold deformation systems are uncoupled to deposition; i.e., the deformation did not directly interfere with deposition parameters and process stability (uncoupled heat source and deformation system). Additionally, cold deformation systems, especially rolling, have enough deformation depth, which prevents the total melting of the deformed zone, promoting intense grain size refinement and stress relief for typical commercial alloys fabricated via DED processes [70]. Despite the operational advantages of cold deformation systems, productivity can be low, especially for low-scale production, due to the high idle time necessary for part cooling.

The hot rolling and forging occur immediately after layer deposition (feedstock material consolidation), reducing idle time (part cooling) and increasing productivity. However, hot deformation is coupled with deposition, which restricts the deposition process window and requires careful control of melting pool size and temperature distribution (macroscopically expressed by the heat source-deformation tool distance) [78]. In addition, given the drop in material strength in high temperatures, the loading force of hot deformation

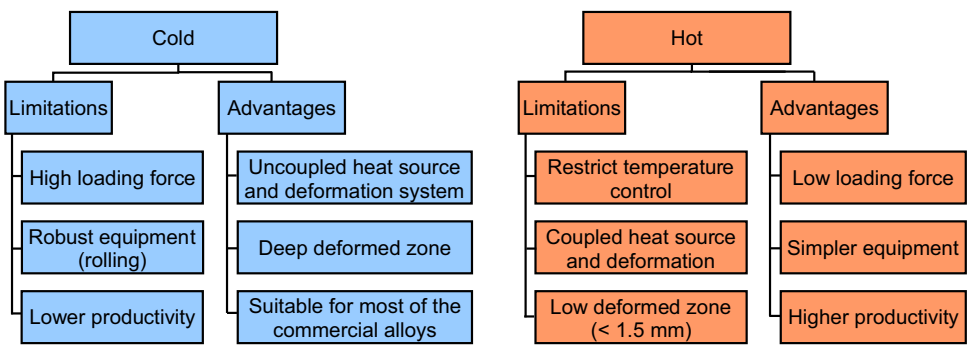

Fig. 36 Advantages and limitations of cold and hot interlayer mechanical deformation systems

is considerably less than cold deformation, requiring less robust equipment [87, 88]. However, because of the inferior loading forces, its deformed zone depth tends to be less than that of cold deformation. Figure 36 summarizes the main limitations and advantages of the deposition coupled with hot and cold interlayer mechanical deformation.

From the materials point of view, the cold deformation system (especially rolling) showed impressive results for commercial 3D printed alloys, meeting the material specifications and promoting quasi-state mechanical properties comparable to traditional thermo-mechanically processed materials (e.g., wrought material). This improvement in mechanical properties was attributed mainly to finer grain size (comparable to wrought) and better heat treatment response. The hot deformation system also showed an appreciable grain size refinement effect and improved mechanical properties; however, for high SFE alloys (e.g., Al-based), its effect was almost insignificant [159, 162]. The cold and hot deformation systems also had different grain size refinement mechanisms for each alloy type namely transformable and non-transformable solid-state alloys. The cold deformation systems induced an intense and deep deformation on the layer surface, which drove the static recrystallization during the reheating thermal cycles (subsequent layer deposition). Thus, given that the recrystallization temperature is inferior to the melting temperature, the new and refined grains can also act as nucleation sites during solidification (like the substrate), which prevent the epitaxial grain growth throughout several layers and refine the microstructure [149]. For hot interlayer deformation, the grain size refinement occurs during (in situ) the deformation (dynamic recrystallization), which must be superior to penetration to induce a finer solidification microstructure. In addition, cold and hot deformation systems can cause, during post-deposition heat treatment and reheating thermal cycles, static recrystallization (grain refinement) since the deformed zone still has stored strain energy [87]. This double grain refinement is especially interesting for alloys that undergo mandatory post-deposition heat treatment, such as non-transformable and precipitation-strengthened alloys (e.g., Inconel 718), which showed an impressive improvement in the quasi-static properties [152].

Despite the significant effect of the cold rolling interlayer deformation on microstructure and quasi-static mechanical properties, its path planning is almost limited to linear path planning (design freedom constraints), which can prevent its use for complex geometry parts (e.g., flanges and bosses) [69]. However, as shown by Zhang et al. [32] and Xie et al. [77], hot rolling interlayer deformation is more flexible (e.g., allowing non-linear deposition) in relation to path planning, increasing its potential applicability. The great advantage of the hammer/peening/forging is their ability to be coupled to a robot arm or CNC machine, allowing almost unrestricted path planning and deposition strategy selection [97]. Therefore, considering the ability to be coupled to a robotic arm, the proven effect on the microstructure refinement and the improvement in the quasi-static mechanical properties, and the previous practical knowledge and performance in arc-welding, the interlayer hammer/peening/forging processes show better industrial scalability indicators, as indicated by Karunakaran et al. [114] and Gupta et al. [115].

5.1 Outlooks

The interlayer (hot and cold) mechanical deformation systems must be expanded to other commercial alloys, which also have the problems related to coarse and oriented microstructure, low response to heat treatment, and anisotropic behavior. In addition, the grain size refinements' mechanisms for the transformable alloys must be clarified (e.g., low-alloy steels and CuAl8 alloy) [21, 31]. Furthermore, employing interlayer deformation with other grain size refinement techniques, notably vibration-assisted methods, has the potential to achieve a finer grain size. This approach can also mitigate residual stress, deformation, and pore issues. However, it does introduce increased process complexity, necessitating the optimization of multiple processes. Also, forced cooling can be used to reduce the idle time of the interlayer cold deformation system [191]. In addition, the impact of primary microstructure (post-solidification grain size), i.e., the DED process (e.g., GMA and laser) and feedstock material type (wire and powder), on the grain size refinement mechanism has not been addressed and compared.

From an industrial adoption perspective, the deposition + interlayer deformation system reliability, reproducibility, and suitability for different deposition strategies and part geometries must be tested, validated, and documented [161, 192, 193]. In addition to quasi-static mechanical properties (Sect. 4), DEDed + interlayer deformed part requirements in under operational conditions must be fulfilled (e.g., fatigue [68, 80, 82], creep, and corrosion [194]), where the literature available is quite scarce. Finally, the improvement of current technology (overcome the mentioned limitations), e.g., the development of a temperature control system that ensures a stable hot deformation temperature and new interlayer deformation variants (e.g., interlayer friction stir processing [195, 196] and interlayer laser shock peening without protective and transparent constraining layers [120, 134]), offers promising avenues. These innovations, drawing inspiration from established welding and casting processes, can be adapted effectively for DED.

6 Conclusions

The present state-of-the-art literature review describes, in detail, the coupled directed energy deposition (DED) processes with interlayer mechanical (cold or hot) deformation systems, their improvements, advantages, limitations, and potential for industrial adoption. Additionally, the grain size refinement mechanisms and interlayer deformation effects on the quasi-static mechanical properties of commercial alloys were comprehensively discussed. In this sense, the following conclusions were drawn:

- The cold rolling system operates with the highest loads (< 160 kN), requiring a large and rigid structure, which restricts it to linear path planning. However, the high-loading force confers an intense grain size refinement and residual stress relief. The hot rolling systems use lower rolling loads (~ 3 kN), have a higher path planning flexibility (allowing curved trajectory), and show similar grain size refinement.
- The hammering, peening, and forging (cold or hot) systems are more flexible than the rolling ones, use less robust and more adjustable equipment, and have almost free path planning (allowing robotization). However, the low-depth deformation zone can induce a lower grain size refinement in relation to rolling, especially for DED-arc (high penetration).
- The interlayer cold deformation system had uncoupled deposition and deformation processes, allowing better control and reproducibility. The hot deformation system must control the distance between the heat source and deformation tool, which restricted the process window.
- For the cold interlayer deformation, the grain size refinement occurred by the accumulation of strain deformation and static recrystallization during the subsequent deposition thermal cycle and post-deposition heat treatment. The interlayer hot deformation can drive in situ dynamic recrystallization and refine the top layer surface grains, which can also function as nucleation sites during the solidification of the next layer. In addition, the remaining deformed zone can also induce static recrystallizing during post-deposition heat treatment.
- Ti-based alloys and high-strength low-alloy steels (solid-state transformable alloys) showed suitable responses to deposition + interlayer mechanical deformation processes with appreciable parent phases (prior β and austenite, respectively) refinement with a non-oriented primary microstructure, which resulted in almost isotropic quasi-static mechanical properties.
- DED + (cold and hot) deformation had lesser effect on the high stacking faults energy (SFE) alloys, where 2xxx and 5xxx series aluminum alloys did not show significant changes in mechanical properties and microstructure aspects.
- Low to medium SFE alloys (e.g., AISI 316 stainless and Inconel 718) had the best response to interlayer (cold and hot) mechanical deformation. Arc plasma and laser DED + interlayer cold/warm deformation increased the Inconel 718 heat treatment response and reduced the anisotropy and texture index, meeting the requirements of the AMS 5662 standard.

Author contribution Francisco Werley Cipriano Farias—conceptualization, data curation, formal analysis, investigation, methodology, validation, writing. Telmo Jorge Gomes dos Santos—conceptualization, data curation, formal analysis, funding acquisition, investigation, methodology, project administration, resources, supervision, visualization, writing—review and editing. João Pedro Oliveira—conceptualization, data curation, formal analysis, funding acquisition, investigation, methodology, project administration, resources, supervision, visualization, writing review and editing.

Funding Open access funding provided by FCT|FCCN (b-on). The authors acknowledge the Portuguese Fundação para a Ciência e a Tecnologia (FCT–MCTES) for its financial support via the project UID/EMS/00667/2019 (UNIDEMI). Funding by national funds from FCT-Fundação para a Ciência e a Tecnologia, I.P., in the scope of the projects LA/P/0037/2020, UIDP/50025/2020, and UIDB/50025/2020 of the Associate Laboratory Institute of Nanostructures, Nanomodelling, and Nanofabrication–i3N is also acknowledged. FWCF acknowledges Fundação para a Ciência e a Tecnologia (FCT-MCTES) for funding the Ph.D. Grant 2022.13870.BD. This activity has received funding from the European Institute of Innovation and Technology (EIT) Raw Materials through the project Smart WAAM: Microstructural Engineering and Integrated Non-Destructive Testing.

Declarations

Ethics approval Not applicable.

Consent to participate Not applicable.

Consent for publication Not applicable.

Competing interests The authors declare no competing interests.

References

1. Williams SW, Martina F, Addison AC, Ding J, Pardal G, Colegrove P (2016) Wire + arc additive manufacturing. Mater Sci Technol 32:641–647. https://doi.org/10.1179/1743284715Y.0000000073
2. Sirichakwal I, Conner B (2016) Implications of additive manufacturing for spare parts inventory, 3D Print. Addit Manuf 3:56–63. https://doi.org/10.1089/3dp.2015.0035
3. Xu B, Han Y, Zhao L, Xie YM (2020) Topological optimization of continuum structures for additive manufacturing considering thin feature and support structure constraints. Eng Optim 53:2122–2143. https://doi.org/10.1080/0305215X.2020.1849170
4. Rodrigues TA, Bairrão N, Farias FWC, Shamsolhodaei A, Shen J, Zhou N, Maawad E, Schell N, Santos TG, Oliveira JP (2022) Steel-copper functionally graded material produced by twin-wire and arc additive manufacturing (T-WAAM). Mater Des 213:110270. https://doi.org/10.1016/J.MATDES.2021.110270
5. Kladovasilakis N, Charalampous P, Kostavelis I, Tzetzis D, Tzovaras D (2021) Impact of metal additive manufacturing parameters on the powder bed fusion and direct energy deposition processes: a comprehensive review. Prog Addit Manuf 6:349–365. https://doi.org/10.1007/s40964-021-00180-8
6. Gorji NE, O'Connor R, Mussatto A, Snelgrove M, González PGM, Brabazon D (2019) Recyclability of stainless steel (316 L) powder within the additive manufacturing process. Materialia 8:100489. https://doi.org/10.1016/J.MTLA.2019.100489
7. Anderson IE, White EMH, Dehoff R (2018) Feedstock powder processing research needs for additive manufacturing development. Curr Opin Solid State Mater Sci 22:8–15. https://doi.org/10.1016/J.COSSMS.2018.01.002
8. Mostafaei A, Zhao C, He Y, Reza Ghiaasiaan S, Shi B, Shao S, Shamsaei N, Wu Z, Kouraytem N, Sun T, Pauza J, Gordon JV, Webler B, Parab ND, Asherloo M, Guo Q, Chen L, Rollett AD (2022) Defects and anomalies in powder bed fusion metal additive manufacturing. Curr Opin Solid State Mater Sci 26:100974. https://doi.org/10.1016/J.COSSMS.2021.100974
9. Fonseca PP, Vidal C, Ferreira F, Duarte VR, Rodrigues TA, Santos TG, Machado CM (2022) Orthogonal cutting of wire and arc additive manufactured parts. Int J Adv Manuf Technol 119:4439–4459. https://doi.org/10.1007/s00170-022-08678-3
10. Singh S, Ramakrishna S, Singh R (2017) Material issues in additive manufacturing: a review. J Manuf Process 25:185–200. https://doi.org/10.1016/J.JMAPRO.2016.11.006
11. Le VT, Mai DS, Doan TK, Paris H (2021) Wire and arc additive manufacturing of 308L stainless steel components: optimization of processing parameters and material properties. Eng Sci Technol an Int J 24:1015–1026. https://doi.org/10.1016/J.JESTCH.2021.01.009
12. Kindermann RMM, Roy MJJ, Morana R, Francis JAA (2022) Effects of microstructural heterogeneity and structural defects on the mechanical behaviour of wire + arc additively manufactured Inconel 718 components. Mater Sci Eng A 839:142826. https://doi.org/10.1016/J.MSEA.2022.142826
13. Sunny S, Mathews R, Gleason G, Malik A, Halley J (2021) Effect of metal additive manufacturing residual stress on post-process machining-induced stress and distortion. Int J Mech Sci 202–203:106534. https://doi.org/10.1016/J.IJMECSCI.2021.106534
14. Fergani O, Berto F, Welo T, Liang SY (2017) Analytical modelling of residual stress in additive manufacturing. Fatigue Fract Eng Mater Struct 40:971–978. https://doi.org/10.1111/FFE.12560
15. Zhang C, Li Y, Gao M, Zeng X (2018) Wire arc additive manufacturing of Al-6Mg alloy using variable polarity cold metal transfer arc as power source. Mater Sci Eng A 711:415–423. https://doi.org/10.1016/J.MSEA.2017.11.084
16. Xu PG, Yin F, Nagai K (2006) Solidification cooling rate and as-cast textures of low-carbon steel strips. Mater Sci Eng A 441:157–166. https://doi.org/10.1016/J.MSEA.2006.09.001
17. Dirisu P, Ganguly S, Mehmanparast A, Martina F, Williams S (2019) Analysis of fracture toughness properties of wire + arc additive manufactured high strength low alloy structural steel components. Mater Sci Eng A 765:138285. https://doi.org/10.1016/j.msea.2019.138285
18. Farias FWC, Duarte VR, da Payão Filho JC, Schell N, Maawad E, Bordas-Czaplicki M, da Fonseca FMA, Cormier J, dos Santos TJG, Oliveira JP (2024) Arc-based directed energy deposited Inconel 718: role of heat treatments on high-temperature tensile behavior. Mater Res Lett 12:97–107. https://doi.org/10.1080/21663831.2023.2297734
19. Colegrove PA, Donoghue J, Martina F, Gu J, Prangnell P, Hönnige J (2017) Application of bulk deformation methods for microstructural and material property improvement and residual stress and distortion control in additively manufactured components. Scr Mater 135:111–118. https://doi.org/10.1016/j.scriptamat.2016.10.031
20. Duarte VR, Rodrigues TA, Schell N, Miranda RM, Oliveira JP, Santos TG (2020) Hot forging wire and arc additive manufacturing (HF-WAAM). Addit Manuf 35:101193. https://doi.org/10.1016/j.addma.2020.101193
21. Duarte VR, Rodrigues TA, Schell N, Miranda RM, Oliveira JP, Santos TG (2022) In-situ hot forging direct energy deposition-arc of CuAl8 alloy. Addit Manuf 102847. https://doi.org/10.1016/j.addma.2022.102847
22. Coules HE, Colegrove P, Cozzolino LD, Wen SW, Kelleher JF (2012) High pressure rolling of low carbon steel weld seams: Part 2 - Roller geometry and residual stress. Sci Technol Weld Join 18:84–90. https://doi.org/10.1179/1362171812Y.0000000080
23. Maurya AK, Yeom JT, Kang SW, Park CH, Hong JK, Reddy NS (2022) Optimization of hybrid manufacturing process combining forging and wire-arc additive manufactured Ti-6Al-4V through hot deformation characterization. J Alloys Compd 894:162453. https://doi.org/10.1016/J.JALLCOM.2021.162453
24. Zhou Y, Lin X, Kang N, Wang Z, Tan H, Huang W (2021) Hot deformation induced microstructural evolution in local-heterogeneous wire + arc additive manufactured 2219 Al alloy. J Alloys Compd 865:158949. https://doi.org/10.1016/j.jallcom.2021.158949
25. Chen J, Wei H, Zhang X, Peng Y, Kong J, Wang K (2021) Flow behavior and microstructure evolution during dynamic deformation of 316 L stainless steel fabricated by wire and arc additive manufacturing. Mater Des 198:109325. https://doi.org/10.1016/j.matdes.2020.109325
26. Lan B, Wang Y, Liu Y, Hooper P, Hopper C, Zhang G, Zhang X, Jiang J (2021) The influence of microstructural anisotropy on the hot deformation of wire arc additive manufactured (WAAM) Inconel 718. Mater Sci Eng A 823:141733. https://doi.org/10.1016/j.msea.2021.141733
27. Motallebi R, Savaedi Z, Mirzadeh H (2022) Additive manufacturing – a review of hot deformation behavior and constitutive modeling of flow stress. Curr Opin Solid State Mater Sci 26:100992. https://doi.org/10.1016/j.cossms.2022.100992
28. Parvaresh B, Salehan R, Miresmaeili R (2021) Investigating isotropy of mechanical and wear properties in As-deposited and inter-layer cold worked specimens manufactured by wire arc additive manufacturing. Met Mater Int 27:92–105. https://doi.org/10.1007/s12540-020-00793-8
29. Shakil SI, Smith NR, Yoder SP, Ross BE, Alvarado DJ, Hadadzadeh A, Haghshenas M (2022) Post fabrication thermomechanical

processing of additive manufactured metals: a review. J Manuf Process 73:757–790. https://doi.org/10.1016/J.JMAPRO.2021.11.047
30. Sunny S, Mathews R, Yu H, Malik A (2022) Effects of microstructure and inherent stress on residual stress induced during powder bed fusion with roller burnishing. Int J Mech Sci 219:107092. https://doi.org/10.1016/j.ijmecsci.2022.107092
31. Colegrove PA, Coules HE, Fairman J, Martina F, Kashoob T, Mamash H, Cozzolino LD (2013) Microstructure and residual stress improvement in wire and arc additively manufactured parts through high-pressure rolling. J Mater Process Technol 213:1782–1791. https://doi.org/10.1016/j.jmatprotec.2013.04.012
32. Zhang H, Wang X, Wang G, Zhang Y (2013) Hybrid direct manufacturing method of metallic parts using deposition and micro continuous rolling. Rapid Prototyp J 19:387–394. https://doi.org/10.1108/RPJ-01-2012-0006
33. Farias FWC, da Payão Filho JC, Moraes e Oliveira VHP (2021) Prediction of the interpass temperature of a wire arc additive manufactured wall: FEM simulations and artificial neural network. Addit Manuf 48:102387. https://doi.org/10.1016/j.addma.2021.102387
34. Paul S, Liu J, Strayer ST, Zhao Y, Sridar S, Klecka MA, Xiong W, To AC (2020) A discrete dendrite dynamics model for epitaxial columnar grain growth in metal additive manufacturing with application to Inconel. Addit Manuf 36:101611. https://doi.org/10.1016/j.addma.2020.101611
35. Rodrigues TA, Duarte V, Avila JA, Santos TG, Miranda RM, Oliveira JP (2019) Wire and arc additive manufacturing of HSLA steel: effect of thermal cycles on microstructure and mechanical properties. Addit Manuf 27:440–450. https://doi.org/10.1016/J.ADDMA.2019.03.029
36. Wang J, Lin X, Wang J, Yang H, Zhou Y, Wang C, Li Q, Huang W (2018) Grain morphology evolution and texture characterization of wire and arc additive manufactured Ti-6Al-4V. J Alloys Compd 768:97–113. https://doi.org/10.1016/j.jallcom.2018.07.235
37. Yi HJ, Kim JW, Kim YL, Shin S (2021) Improving mechanical properties of wire arc additively manufactured Ti-6Al-4V alloy by ultrasonic needle peening treatment, Korean. J Mater Res 31:245–254. https://doi.org/10.3740/MRSK.2021.31.5.245
38. Gordon JV, Haden CV, Nied HF, Vinci RP, Harlow DG (2018) Fatigue crack growth anisotropy, texture and residual stress in austenitic steel made by wire and arc additive manufacturing. Mater Sci Eng A 724:431–438. https://doi.org/10.1016/J.MSEA.2018.03.075
39. Wang J, Zhang J, Liu G, Liang L, Yang G, Huang A, Pang S (2022) Effects of scanning strategies on residual stress and deformation by high-power direct energy deposition: Island size and laser jump strategy between islands. J Manuf Process 75:23–40. https://doi.org/10.1016/J.JMAPRO.2021.12.054
40. Liu P, Wang Z, Xiao Y, Horstemeyer MF, Cui X, Chen L (2019) Insight into the mechanisms of columnar to equiaxed grain transition during metallic additive manufacturing. Addit Manuf 26:22–29. https://doi.org/10.1016/J.ADDMA.2018.12.019
41. Bermingham MJ, McDonald SD, Dargusch MS (2018) Effect of trace lanthanum hexaboride and boron additions on microstructure, tensile properties and anisotropy of Ti-6Al-4V produced by additive manufacturing. Mater Sci Eng A 719:1–11. https://doi.org/10.1016/j.msea.2018.02.012
42. Kennedy JR, Davis AE, Caballero AE, Williams S, Pickering EJ, Prangnell PB (2021) The potential for grain refinement of wire-arc additive manufactured (WAAM) Ti-6Al-4V by ZrN and TiN inoculation. Addit Manuf 40:101928. https://doi.org/10.1016/j.addma.2021.101928
43. Rodrigues TA, Duarte VR, Tomás D, Avila JA, Escobar JD, Rossinyol E, Schell N, Santos TG, Oliveira JP (2020) In-situ strengthening of a high strength low alloy steel during wire and arc additive manufacturing (WAAM). Addit Manuf 34:101200. https://doi.org/10.1016/j.addma.2020.101200
44. Bermingham MJ, McDonald SD, StJohn DH, Dargusch MS (2009) Beryllium as a grain refiner in titanium alloys. J Alloys Compd 481:20–23. https://doi.org/10.1016/j.jallcom.2009.03.016
45. Zhuo Y, Yang C, Fan C, Lin S (2021) Effects of trace Sn and Cr addition on microstructure and mechanical properties of TC17 titanium alloy repaired by wire arc additive manufacturing. J Alloys Compd 888:161473. https://doi.org/10.1016/j.jallcom.2021.161473
46. da Silva LJ, Souza DM, de Araújo DB, Reis RP, Scotti A (2020) Concept and validation of an active cooling technique to mitigate heat accumulation in WAAM. Int J Adv Manuf Technol 107:2513–2523. https://doi.org/10.1007/s00170-020-05201-4
47. Hackenhaar W, Mazzaferro JAE, Montevecchi F, Campatelli G (2020) An experimental-numerical study of active cooling in wire arc additive manufacturing. J Manuf Process 52:58–65. https://doi.org/10.1016/j.jmapro.2020.01.051
48. Zhang C, Gao M, Zeng X (2019) Workpiece vibration augmented wire arc additive manufacturing of high strength aluminum alloy. J Mater Process Technol 271:85–92. https://doi.org/10.1016/j.jmatprotec.2019.03.028
49. Li C, Sun S, Liu C, Lu Q, Ma P, Wang Y (2019) Microstructure and mechanical properties of TiC/AlSi10Mg alloy fabricated by laser additive manufacturing under high-frequency microvibration. J Alloys Compd 794:236–246. https://doi.org/10.1016/J.JALLCOM.2019.04.287
50. Scotti FM, Teixeira FR, da Silva LJ, de Araújo DB, Reis RP, Scotti A (2020) Thermal management in WAAM through the CMT Advanced process and an active cooling technique. J Manuf Process 57:23–35. https://doi.org/10.1016/j.jmapro.2020.06.007
51. Chen Y, Xu M, Zhang T, Xie J, Wei K, Wang S, Yin L, He P (2022) Grain refinement and mechanical properties improvement of Inconel 625 alloy fabricated by ultrasonic-assisted wire and arc additive manufacturing. J Alloys Compd 910:164957. https://doi.org/10.1016/j.jallcom.2022.164957
52. Ji F, Qin X, Hu Z, Xiong X, Ni M, Wu M (2022) Influence of ultrasonic vibration on molten pool behavior and deposition layer forming morphology for wire and arc additive manufacturing, Int. Commun. Heat Mass Transf 130. https://doi.org/10.1016/J.ICHEATMASSTRANSFER.2021.105789
53. Todaro CJJ, Easton MAA, Qiu D, Zhang D, Bermingham MJJ, Lui EWW, Brandt M, StJohn DHH, Qian M (2020) Grain structure control during metal 3D printing by high-intensity ultrasound. Nat Commun 11:1–9. https://doi.org/10.1038/s41467-019-13874-z
54. Elmadih W, Chronopoulos D, Syam WP, Maskery I, Meng H, Leach RK (2019) Three-dimensional resonating metamaterials for low-frequency vibration attenuation. Sci Rep 9:1–8. https://doi.org/10.1038/s41598-019-47644-0
55. Xu JJ, Chen L, Ni C (2007) Effect of vibratory weld conditioning on the residual stresses and distortion in multipass girth-butt welded pipes. Int J Press Vessel Pip 84:298–303. https://doi.org/10.1016/J.IJPVP.2006.11.004
56. Munsi ASMY, Waddell AJ, Walker CA (2001) The effect of vibratory stress on the welding microstructure and residual stress distribution. J Mater Des Appl 215:99–111. https://doi.org/10.1177/146442070121500204
57. Hsieh CC, Wang PS, Wang JS, Wu W (2014) Evolution of microstructure and residual stress under various vibration

modes in 304 stainless steel welds. Sci World J 2014:9. https://doi.org/10.1155/2014/895790
58. Todaro CJ, Easton MA, Qiu D, Brandt M, StJohn DH, Qian M (2021) Grain refinement of stainless steel in ultrasound-assisted additive manufacturing. Addit Manuf 37. https://doi.org/10.1016/J.ADDMA.2020.101632
59. Zhang X, Kang J, Wang S, Ma J, Huang T (2015) The effect of ultrasonic processing on solidification microstructure and heat transfer in stainless steel melt. Ultrason Sonochem 27:307–315. https://doi.org/10.1016/J.ULTSONCH.2015.05.041
60. Xu JJ, Chen LG, Ni CZ (2013) Effects of vibratory weld conditioning on residual stresses and transverse contraction distortions in multipass welding. Sci Technol Weld Join 11:374–378. https://doi.org/10.1179/174329306X113325
61. Li X, Wang M, Du F (2005) A coupling thermal mechanical and microstructural FE model for hot strip continuous rolling process and verification. Mater Sci Eng A 408:33–41. https://doi.org/10.1016/J.MSEA.2005.04.065
62. Ataka M (2015) Rolling technology and theory for the last 100 years: the contribution of theory to innovation in strip rolling technology. ISIJ Int 55:94–107. https://doi.org/10.2355/isijinternational.55.89
63. Lee YS, Lee SU, Van Tyne CJ, Joo BD, Moon YH (2011) Internal void closure during the forging of large cast ingots using a simulation approach. J Mater Process Technol 211:1136–1145. https://doi.org/10.1016/J.JMATPROTEC.2011.01.017
64. Toscano D, Shaha SK, Behravesh B, Jahed H, Williams B (2017) Effect of forging on microstructure, texture, and uniaxial properties of cast AZ31B alloy. J Mater Eng Perform 26:3090–3103. https://doi.org/10.1007/s11665-017-2743-2
65. Abbaszadeh M, Hönnige JR, Martina F, Neto L, Kashaev N, Colegrove P, Williams S, Klusemann B (2019) Numerical investigation of the effect of rolling on the localized stress and strain induction for wire + arc additive manufactured structures. J Mater Eng Perform 28:4931–4942. https://doi.org/10.1007/s11665-019-04249-y
66. Adams TE, Härtel S, Hälsig A, Awiszus B, Mayr P (2020) Weld-Forming: a new inline process combination to improve weld seam properties. Weld World 64:601–610. https://doi.org/10.1007/s40194-020-00856-9
67. Coules HE, Colegrove P, Cozzolino LD, Wen SW, Ganguly S, Pirling T (2012) Effect of high pressure rolling on weld-induced residual stresses. Sci Technol Weld Join 17:394–401. https://doi.org/10.1179/1362171812Y.0000000021
68. Dirisu P, Supriyo G, Martina F, Xu X, Williams S (2020) Wire plus arc additive manufactured functional steel surfaces enhanced by rolling. Int J Fatigue 130:105237. https://doi.org/10.1016/j.ijfatigue.2019.105237
69. Hönnige JR, Colegrove PA, Ahmad B, Fitzpatrick ME, Ganguly S, Lee TL, Williams SW (2018) Residual stress and texture control in Ti-6Al-4V wire + arc additively manufactured intersections by stress relief and rolling. Mater Des 150:193–205. https://doi.org/10.1016/j.matdes.2018.03.065
70. McAndrew AR, Alvarez Rosales M, Colegrove PA, Hönnige JR, Ho A, Fayolle R, Eyitayo K, Stan I, Sukrongpang P, Crochemore A, Pinter Z (2018) Interpass rolling of Ti-6Al-4V wire + arc additively manufactured features for microstructural refinement. Addit Manuf 21:340–349. https://doi.org/10.1016/j.addma.2018.03.006
71. Hönnige JR, Williams S, Roy MJ, Colegrove P, Ganguly S (2016) Residual stress characterization and control in the additive manufacture of large scale metal structures, in: Residual Stress., Materials Research Forum LLC, pp 455–460. https://doi.org/10.21741/9781945291173-77
72. Hönnige JR, Colegrove PA, Ganguly S, Eimer E, Kabra S, Williams S (2018) Control of residual stress and distortion in aluminium wire + arc additive manufacture with rolling. Addit Manuf 22:775–783. https://doi.org/10.1016/j.addma.2018.06.015
73. Geng H, Li J, Xiong J, Lin X, Huang D, Zhang F (2018) Formation and improvement of surface waviness for additive manufacturing 5A06 aluminium alloy component with GTAW system. Rapid Prototyp J 24:342–350. https://doi.org/10.1108/RPJ-04-2016-0064
74. Gu J, Ding J, Williams SW, Gu H, Ma P, Zhai Y (2016) The effect of inter-layer cold working and post-deposition heat treatment on porosity in additively manufactured aluminum alloys. J Mater Process Technol 230:26–34. https://doi.org/10.1016/j.jmatprotec.2015.11.006
75. Bercelli L, Moyne S, Dhondt M, Doudard C, Calloch S, Beaudet J (2021) A probabilistic approach for high cycle fatigue of wire and arc additive manufactured parts taking into account process-induced pores. Addit Manuf 42:101989. https://doi.org/10.1016/J.ADDMA.2021.101989
76. Zong N, Zhang M, Liang X, Jing T (2021) Optimizing distance between laser and ultrasonic vibration points for additive manufacturing of HG785 steel with the assistance of ultrasonic vibration. J Brazilian Soc Mech Sci Eng 43:1–9. https://doi.org/10.1007/s40430-021-03133-y
77. Xie Y, Zhang H, Zhou F (2016) Improvement in geometrical accuracy and mechanical property for arc-based additive manufacturing using metamorphic rolling mechanism. J Manuf Sci Eng Trans ASME 138:1–8. https://doi.org/10.1115/1.4032079
78. Fu Y, Zhang H, Wang G, Wang H (2017) Investigation of mechanical properties for hybrid deposition and micro-rolling of bainite steel. J Mater Process Technol 250:220–227. https://doi.org/10.1016/j.jmatprotec.2017.07.023
79. Zhao W, Zha GC, Xi MZ, Gao SY (2018) Effects of synchronous rolling on microstructure, hardness, and wear resistance of laser multilayer cladding. J Mater Eng Perform 27:1746–1752. https://doi.org/10.1007/s11665-018-3286-x
80. Xie C, Wu S, Yu Y, Zhang H, Hu Y, Zhang M, Wang G (2021) Defect-correlated fatigue resistance of additively manufactured Al-Mg4.5Mn alloy with in situ micro-rolling. J Mater Process Technol. 291:117039. https://doi.org/10.1016/j.jmatprotec.2020.117039
81. Ma C, Liu Y, Li C, Dong H, Li D, Wu X, Liu P, Sun Q, Jin H, Zhang F (2020) Mechanical properties of carbon steel by compound arc and vibration shock forging-rolling. J Manuf Process 60:11–22. https://doi.org/10.1016/j.jmapro.2020.10.005
82. Gao Y, Wu C, Peng K, Song X, Fu Y, Chen Q, Zhang M, Wang G, Liu J (2021) Towards superior fatigue crack growth resistance of TC4-DT alloy by in-situ rolled wire-arc additive manufacturing. J Mater Res Technol 15:1395–1407. https://doi.org/10.1016/j.jmrt.2021.08.152
83. Zhao X, Wang Y, Zhang H, Li R, Chen X, Fu Y (2022) Overlapping optimization of hybrid deposited and micro-rolling additive manufacturing. Rapid Prototyp J 28:1086–1096. https://doi.org/10.1108/RPJ-03-2021-0061
84. Cao Y, Zhu S, Liang X, Wang W (2011) Overlapping model of beads and curve fitting of bead section for rapid manufacturing by robotic MAG welding process. Robot Comput Integr Manuf 27:641–645. https://doi.org/10.1016/J.RCIM.2010.11.002
85. Xiong J, Zhang G, Gao H, Wu L (2013) Modeling of bead section profile and overlapping beads with experimental validation for robotic GMAW-based rapid manufacturing. Robot Comput Integr Manuf 29:417–423. https://doi.org/10.1016/J.RCIM.2012.09.011
86. Ding D, Pan Z, Cuiuri D, Li H (2015) A multi-bead overlapping model for robotic wire and arc additive manufacturing (WAAM). Robot Comput Integr Manuf 31:101–110. https://doi.org/10.1016/J.RCIM.2014.08.008

87. Li C, Tian Y, Chen Y, Hodgson P, Wu X, Zhu Y, Huang A (2021) Hierarchical layered and refined grain structure of Inconel 718 superalloy produced by rolling-assisted directed energy deposition. Addit Manuf Lett 1:100009. https://doi.org/10.1016/j.addlet.2021.100009
88. Tian X, Zhu Y, Lim CVS, Williams J, Boyer R, Wu X, Zhang K, Huang A (2021) Isotropic and improved tensile properties of Ti-6Al-4V achieved by in-situ rolling in direct energy deposition. Addit Manuf 46. https://doi.org/10.1016/j.addma.2021.102151
89. Xu X, Ganguly S, Ding J, Seow CE, Williams S (2018) Enhancing mechanical properties of wire + arc additively manufactured INCONEL 718 superalloy through in-process thermomechanical processing. Mater Des 160:1042–1051. https://doi.org/10.1016/j.matdes.2018.10.038
90. Martina F, Colegrove PA, Williams SW, Meyer J (2015) Microstructure of interpass rolled wire + arc additive manufacturing Ti-6Al-4V components. Metall Mater Trans A Phys Metall Mater Sci 46:6103–6118. https://doi.org/10.1007/s11661-015-3172-1
91. Kan WH, Jiang D, Humbert M, Gao X, Bhatia VK, Proust G, Zhu Y, Hodgson P, Huang A (2022) Effect of in-situ layer-by-layer rolling on the microstructure, mechanical properties, and corrosion resistance of a directed energy deposited 316 L stainless steel. Addit Manuf 55:102863. https://doi.org/10.1016/J.ADDMA.2022.102863
92. Zhang T, Li H, Gong H, Ding J, Wu Y, Diao C, Zhang X, Williams S (2022) Hybrid wire - arc additive manufacture and effect of rolling process on microstructure and tensile properties of Inconel 718. J Mater Process Technol 299:117361. https://doi.org/10.1016/j.jmatprotec.2021.117361
93. Huang J, Yuan W, Yu S, Zhang L, Yu X, Fan D (2020) Droplet transfer behavior in bypass-coupled wire arc additive manufacturing. J Manuf Process 49:397–412. https://doi.org/10.1016/J.JMAPRO.2019.12.002
94. Abdullah A, Malaki M, Eskandari A (2012) Strength enhancement of the welded structures by ultrasonic peening. Mater Des 38:7–18. https://doi.org/10.1016/J.MATDES.2012.01.040
95. Nasiłowska B, Bogdanowicz Z, Wojucki M (2015) Shot peening effect on 904 L welds corrosion resistance. J Constr Steel Res 115:276–282. https://doi.org/10.1016/J.JCSR.2015.08.041
96. Liu C, Yang J, Ge Q, Gao F, Zou J (2018) Mechanical properties improvement of thick multi-pass weld by layered ultrasonic impact treatment. Sci Technol Weld Join 23:95–104. https://doi.org/10.1080/13621718.2017.1327201
97. Hönnige JR, Colegrove P, Williams S (2017) Improvement of microstructure and mechanical properties in Wire + Arc Additively Manufactured Ti-6Al-4V with Machine Hammer Peening. Procedia Eng 216:8–17. https://doi.org/10.1016/j.proeng.2018.02.083
98. Hönnige JR, Davis AE, Ho A, Kennedy JR, Neto L, Prangnell P, Williams S (2020) The effectiveness of grain refinement by machine hammer peening in high deposition rate wire-arc AM Ti-6Al-4V. Metall Mater Trans A 51:3692–3703. https://doi.org/10.1007/s11661-020-05781-6
99. Kobayashi M, Matsui T, Murakami Y (1998) Mechanism of creation of compressive residual stress by shot peening. Int J Fatigue 20:351–357. https://doi.org/10.1016/S0142-1123(98)00002-4
100. Davis AE, Caballero AE, Biswal R, Williams S, Prangnell PB (2022) Comparison of microstructure refinement in wire-arc additively manufactured Ti–6Al–2Sn–4Zr–2Mo–0.1Si and Ti–6Al–4V built with inter-pass deformation. Metall Mater Trans A 53:3833–3852. https://doi.org/10.1007/s11661-022-06811-1
101. Fang X, Zhang L, Chen G, Huang K, Xue F, Wang L, Zhao J, Lu B (2021) Microstructure evolution of wire-arc additively manufactured 2319 aluminum alloy with interlayer hammering. Mater Sci Eng A 800:140168. https://doi.org/10.1016/j.msea.2020.140168
102. Shchitsyn Y, Kartashev M, Krivonosova E, Olshanskaya T, Trushnikov D (2021) Formation of structure and properties of two-phase ti-6al-4v alloy during cold metal transfer additive deposition with interpass forging. Materials (Basel) 14:4415. https://doi.org/10.3390/ma14164415
103. Kudryavtsev Y, Kleiman J (2011) Fatigue life improvement of welded elements and structures by ultrasonic impact treatment. Int Conf Offshore Mech Arct Eng, ASME, : pp 629–637. https://doi.org/10.1115/OMAE2011-50310
104. Gale J, Achuhan A (2017) Application of ultrasonic peening during DMLS production of 316L stainless steel and its effect on material behavior. Rapid Prototyp J 23:1185–1194. https://doi.org/10.1108/RPJ-09-2016-0140
105. Wang Y, Shi J (2019) Microstructure and properties of Inconel 718 fabricated by directed energy deposition with in-situ ultrasonic impact peening. Metal Mater Trans B Process Metall Mater Process Sci 50:2815–2827. https://doi.org/10.1007/s11663-019-01672-3
106. Wang Y, Shi J (2020) Recrystallization behavior and tensile properties of laser metal deposited Inconel 718 upon in-situ ultrasonic impact peening and heat treatment. Mater Sci Eng A 786:139434. https://doi.org/10.1016/j.msea.2020.139434
107. Zhang M, Liu C, Shi X, Chen X, Chen C, Zuo J, Lu J, Ma S (2016) Residual stress, defects and grain morphology of Ti-6Al-4V alloy produced by ultrasonic impact treatment assisted selective laser melting. Appl Sci 6:304. https://doi.org/10.3390/APP6110304
108. Ye H, Ye K, Guo B, Le F, Wei C, Sun X, Wang G, Liu Y (2020) Effects of combining ultrasonic micro-forging treatment with laser metal wire deposition on microstructural and mechanical properties in Ti–6Al–4V alloy. Mater Charact 162:110187. https://doi.org/10.1016/j.matchar.2020.110187
109. Li Q, Zhang Y, Chen J, Guo B, Wang W, Jing Y, Liu Y (2021) Effect of ultrasonic micro-forging treatment on microstructure and mechanical properties of GH3039 superalloy processed by directed energy deposition. J Mater Sci Technol 70:185–196. https://doi.org/10.1016/j.jmst.2020.09.001
110. Xiong X, Qin X, Ji F, Hu Z, Hua L (2021) Microstructure and mechanical properties of wire + arc additively manufactured mild steel by welding with trailing hammer peening. Steel Res Int 92:1–11. https://doi.org/10.1002/srin.202100238
111. Farias FWC, Duarte VR, Felice IO, da Filho JCP, Schell N, Maawad E, Avila JA, Li JY, Zhang Y, Santos TG, Oliveira JP (2023) In situ interlayer hot forging arc-based directed energy deposition of Inconel® 625: process development and microstructure effects. Addit Manuf 66:103476. https://doi.org/10.1016/J.ADDMA.2023.103476
112. Farias FWC, Duarte VR, Felice IO, da Filho JCP, Schell N, Maawad E, Li JY, Zhang Y, Santos TG, Oliveira JP (2023) In situ interlayer hot forging arc plasma directed energy deposition of Inconel® 625: microstructure evolution during heat treatments. J Alloys Compd 952:170059. https://doi.org/10.1016/J.JALLCOM.2023.170059
113. Gao S, Liu R, Huang R, Song X, Seita M (2022) A hybrid directed energy deposition process to manipulate microstructure and properties of austenitic stainless steel. Mater Des 213:110360. https://doi.org/10.1016/j.matdes.2021.110360
114 Karunakaran KP, Kamal Gupta N, Kumar Patel A, Rakeshkumar K, Ganesan G (2022) Siddhartha MSealy, Bernard A, Multi-station multi-axis hybrid layered manufacturing (MSMA-HLM). Manuf Lett 33:630–639. https://doi.org/10.1016/j.mfglet.2022.07.078
115. Gupta NK, Ganesan GB, Karade S, Gupta NK, Ganesan GB, Karade S, Mehta AK, Karunakaran PK (2022) Effect of multiple

technologies on minimizing the residual stresses in additive manufacturing, in: 11th Int. Conf. Residual Stress
116. Ding K, Ye L (2006) Laser shock peening: performance and process simulation, 1st edn. CRC Press
117. Munther M, Martin T, Tajyar A, Hackel L, Beheshti A, Davami K (2020) Laser shock peening and its effects on microstructure and properties of additively manufactured metal alloys: a review. Eng Res Express 2:022001. https://doi.org/10.1088/2631-8695/AB9B16
118. Mahmood MA, Chioibasu D, Rehman AU, Mihai S, Popescu AC (2022) Post-processing techniques to enhance the quality of metallic parts produced by additive manufacturing. Metals (Basel) 12:77. https://doi.org/10.3390/MET12010077
119. Sealy MP, Hadidi H, Kanger CJ, Yan XL, Cui B, McGeough JA (2019) Glocal integrity in 420 stainless steel by asynchronous laser processing. CIRP Ann 68:189–192. https://doi.org/10.1016/j.cirp.2019.04.105
120. Zhou J, Zhou X, Li H, Hu J, Han X, Liu S (2022) In-situ laser shock peening for improved surface quality and mechanical properties of laser-directed energy-deposited AlSi10Mg alloy. Addit Manuf 60:103177. https://doi.org/10.1016/J.ADDMA.2022.103177
121. Sun R, Li L, Zhu Y, Guo W, Peng P, Cong B, Sun J, Che Z, Li B, Guo C, Liu L (2018) Microstructure, residual stress and tensile properties control of wire-arc additive manufactured 2319 aluminum alloy with laser shock peening. J Alloys Compd 747:255–265. https://doi.org/10.1016/j.jallcom.2018.02.353
122. Deng WW, Lu HF, Xing YH, Luo KY, Lu JZ (2022) Effect of laser shock peening on tensile properties and microstructure of selective laser melted 316L stainless steel with different build directions. Mater Sci Eng A 850:143567. https://doi.org/10.1016/J.MSEA.2022.143567
123. Hu X, Zhao J, Teng X, Nie X, Jiang Y, Zhang Y (2022) Fatigue resistance improvement on double-sided welded joints of a titanium alloy treated by laser shock peening. J Mater Eng Perform 31:1–10. https://doi.org/10.1007/s11665-022-07006-w
124. Nithin Joseph Reddy SA, Thrinadh E, Prabhakaran S, Kalainathan S, Arivazhagan N, Manikandan M (2018) Surface modification technique to enhance metallurgical and mechanical properties of alloy C-276 weldment by laser shock peening without coating. Sādhanā 43:1–8. https://doi.org/10.1007/s12046-018-0959-y
125. Varin S, Agarwal M, Chugh A, Manikandan M, Prabhakaran S, Kalainathan S, Shukla P, Lawrence J, Arivazhagan N (2019) Effect of laser shock peening on commercially pure titanium-1 weldment fabricated by gas tungsten arc welding technique. Trans Indian Inst Met 72:1569–1573. https://doi.org/10.1007/s12666-019-01704-1
126. Bhardwaj T, Shukla M, Rai AK, Biswal R, Ranganathan K, Ganesh P, Bindra KS, Kaul R (2021) Experimental investigation of multiple laser shock peening on mechanical properties of laser sintering additively manufactured maraging steel. J Mater Eng Perform 30:8515–8528. https://doi.org/10.1007/s11665-021-06049-9
127. Chi J, Cai Z, Zhang HH, Zhang HH, Guo W, Wan Z, Han G, Peng P, Zeng Z (2021) Combining manufacturing of titanium alloy through direct energy deposition and laser shock peening processes. Mater Des 203:109626. https://doi.org/10.1016/J.MATDES.2021.109626
128. Karthik D, Swaroop S (2016) Laser peening without coating induced phase transformation and thermal relaxation of residual stresses in AISI 321 steel. Surf Coatings Technol 291:161–171. https://doi.org/10.1016/J.SURFCOAT.2016.02.038
129. Lan L, Xin R, Jin X, Gao S, He B (2022) Influence of multiple laser shock peening treatments on the microstructure and mechanical properties of Ti−6Al−4V alloy fabricated by electron beam melting. Int J Miner Metall Mater 29:1780–1787. https://doi.org/10.1007/S12613-021-2322-2
130. An Z, He W, Zhou X, Zhou L, Nie X (2022) On the microstructure, residual stress and fatigue performance of laser metal deposited TC17 alloy subjected to laser shock peening. Materials (Basel) 15:6501. https://doi.org/10.3390/MA15186501
131. Zhang H, Cai Z, Chi J, Sun R, Che Z, Lin L, Peng P, Zhang H, Guo W (2022) Gradient microstructure evolution in laser shock peened Ti6Al4V titanium alloy. Surf Coatings Technol 437:128378. https://doi.org/10.1016/J.SURFCOAT.2022.128378
132. Xin R, Lan L, Bai C, Gao S, He B, Wang J (2022) Fatigue properties of selective laser melted Ti-6Al-4V alloy subjected to laser shock processing. J Mater Sci 57:9619–9630. https://doi.org/10.1007/s10853-022-07019-9
133. Lu H, Wu L, Wei H, Cai J, Luo K, Xu X, Lu J (2022) Microstructural evolution and tensile property enhancement of remanufactured Ti6Al4V using hybrid manufacturing of laser directed energy deposition with laser shock peening. Addit Manuf 55:102877. https://doi.org/10.1016/J.ADDMA.2022.102877
134. Lu J, Lu H, Xu X, Yao J, Cai J, Luo K (2020) High-performance integrated additive manufacturing with laser shock peening – induced microstructural evolution and improvement in mechanical properties of Ti6Al4V alloy components. Int J Mach Tools Manuf 148:103475. https://doi.org/10.1016/J.IJMACHTOOLS.2019.103475
135. Guo W, Sun R, Song B, Zhu Y, Li F, Che Z, Li B, Guo C, Liu L, Peng P (2018) Laser shock peening of laser additive manufactured Ti6Al4V titanium alloy. Surf Coatings Technol 349:503–510. https://doi.org/10.1016/J.SURFCOAT.2018.06.020
136. Chen L, Gu P, Ge T, Sun Y, Li L, Ren X (2022) Effect of laser shock peening on microstructure and mechanical properties of TiC strengthened inconel 625 alloy processed by selective laser melting. Mater Sci Eng A 835:142610. https://doi.org/10.1016/J.MSEA.2022.142610
137. Ola OT, Valdez RL, Oluwasegun KM, Ojo OA, Chan K, Birur A, Cuddy J (2019) Process variable optimization in the cold metal transfer weld repair of aerospace ZE41A-T5 alloy using central composite design. Int J Adv Manuf Technol 105:4827–4835. https://doi.org/10.1007/s00170-019-04584-3
138. Hsiao YF, Tarng YS, Huang WJ (2007) Optimization of plasma arc welding parameters by using the Taguchi method with the grey relational analysis. Mater Manuf Process 23:51–58. https://doi.org/10.1080/10426910701524527
139. Ni M, Qin X, Hu Z, Ji F, Yang S, Wang S (2022) Forming characteristics and control method of weld bead for GMAW on curved surface. Int J Adv Manuf Technol 119:1883–1908. https://doi.org/10.1007/s00170-021-08191-z
140. Wen Y, Wu Y, Hua L, Xie L, Wang L, Zhang LC, Lu W (2021) Effects of shot peening on microstructure evolution and mechanical properties of surface nanocrystal layer on titanium matrix composite. Mater Des 206:109760. https://doi.org/10.1016/J.MATDES.2021.109760
141. Maleki E, Unal O, Guagliano M, Bagherifard S (2022) Analysing the fatigue behaviour and residual stress relaxation of gradient nano-structured 316L steel subjected to the shot peening via deep learning approach. Met Mater Int 28:112–131. https://doi.org/10.1007/s12540-021-00995-8
142. Xie L, Wang C, Wang L, Wang Z, Jiang C, Lu W, Ji V (2016) Numerical analysis and experimental validation on residual stress distribution of titanium matrix composite after shot peening treatment. Mech Mater 99:2–8. https://doi.org/10.1016/J.MECHMAT.2016.05.005
143. Lu H, Deng W, Luo K, Chen Y, Wang J, Lu J (2023) Tailoring microstructure of additively manufactured Ti6Al4V titanium

alloy using hybrid additive manufacturing technology. Addit Manuf 63:103416. https://doi.org/10.1016/j.addma.2023.103416
144. Short AB (2013) Gas tungsten arc welding of α + β titanium alloys: a review. Mater Sci Technol 25:309–324. https://doi.org/10.1179/174328408X389463
145. Huang K, Logé RE (2016) A review of dynamic recrystallization phenomena in metallic materials. Mater Des 111:548–574. https://doi.org/10.1016/j.matdes.2016.09.012
146. Donoghue J, Antonysamy AA, Martina F, Colegrove PA, Williams SW, Prangnell PB (2016) The effectiveness of combining rolling deformation with wire–arc additive manufacture on β-grain refinement and texture modification in Ti–6Al–4V. Mater Charact 114:103–114. https://doi.org/10.1016/J.MATCHAR.2016.02.001
147. Ding R, Guo ZX (2004) Microstructural evolution of a Ti–6Al–4V alloy during β-phase processing: experimental and simulative investigations. Mater Sci Eng A 365:172–179. https://doi.org/10.1016/J.MSEA.2003.09.024
148. Davis AE, Hönnige JR, Martina F, Prangnell PB (2020) Quantification of strain fields and grain refinement in Ti-6Al-4V inter-pass rolled wire-arc AM by EBSD misorientation analysis. Mater Charact 170:151–155. https://doi.org/10.1016/j.matchar.2020.110673
149. Donoghue J, Davis AE, Daniel CS, Garner A, Martina F, Quinta da Fonseca J, Prangnell PB (2020) On the observation of annealing twins during simulating β-grain refinement in Ti–6Al–4V high deposition rate AM with in-process deformation. Acta Mater 186:229–241. https://doi.org/10.1016/j.actamat.2020.01.009
150. Davis AE, Kennedy JR, Ding J, Prangnell PB (2020) The effect of processing parameters on rapid-heating β recrystallization in inter-pass deformed Ti-6Al-4V wire-arc additive manufacturing. Mater Charact 163:110298. https://doi.org/10.1016/J.MATCHAR.2020.110298
151. Sridharan N, Noakes MW, Nycz A, Love LJ, Dehoff RR, Babu SS (2018) On the toughness scatter in low alloy C-Mn steel samples fabricated using wire arc additive manufacturing. Mater Sci Eng A 713:18–27. https://doi.org/10.1016/j.msea.2017.11.101
152. Xu X, Ganguly S, Ding J, Dirisu P, Martina F, Liu X, Williams SW (2019) Improving mechanical properties of wire plus arc additively manufactured maraging steel through plastic deformation enhanced aging response. Mater Sci Eng A 747:111–118. https://doi.org/10.1016/j.msea.2018.12.114
153. Nishioka K, Ichikawa K (2012) Progress in thermomechanical control of steel plates and their commercialization. Sci Technol Adv Mater 13:023001. https://doi.org/10.1088/1468-6996/13/2/023001
154. Ma R, Fang K, Yang JG, Liu XS, Fang HY (2014) Grain refinement of HAZ in multi-pass welding. J Mater Process Technol 214:1131–1135. https://doi.org/10.1016/J.JMATPROTEC.2013.12.017
155. Zhao H, Palmiere EJ (2018) Effect of austenite grain size on acicular ferrite transformation in a HSLA steel. Mater Charact 145:479–489. https://doi.org/10.1016/J.MATCHAR.2018.09.013
156. Seow CE, Coules HE, Wu G, Khan RHU, Xu X, Williams S (2019) Wire + arc additively manufactured Inconel 718: effect of post-deposition heat treatments on microstructure and tensile properties. Mater Des 183:108157. https://doi.org/10.1016/j.matdes.2019.108157
157. Hönnige J, Seow CE, Ganguly S, Xu X, Cabeza S, Coules H, Williams S (2021) Study of residual stress and microstructural evolution in as-deposited and inter-pass rolled wire plus arc additively manufactured Inconel 718 alloy after ageing treatment. Mater Sci Eng A 801. https://doi.org/10.1016/j.msea.2020.140368
158. Zhang T, Li H, Gong H, Wu Y, Ahmad AS, Chen X (2021) Effect of rolling force on tensile properties of additively manufactured Inconel 718 at ambient and elevated temperatures. J Alloys Compd 884:161050. https://doi.org/10.1016/j.jallcom.2021.161050
159. Gu J, Wang X, Bai J, Ding J, Williams S, Zhai Y, Liu K (2018) Deformation microstructures and strengthening mechanisms for the wire + arc additively manufactured Al-Mg4.5Mn alloy with inter-layer rolling. Mater Sci Eng A 712:292–301. https://doi.org/10.1016/j.msea.2017.11.113
160. Gu J, Ding J, Williams SW, Gu H, Bai J, Zhai Y, Ma P (2016) The strengthening effect of inter-layer cold working and post-deposition heat treatment on the additively manufactured Al-6.3Cu alloy. Mater Sci Eng A 651:18–26. https://doi.org/10.1016/j.msea.2015.10.101
161. Hai Ou Z, Rui W, Liye L, Wang GL (2016) HDMR technology for the aircraft metal part. Rapid Prototyp J 22:857–863. https://doi.org/10.1108/RPJ-05-2015-0047
162. Liao Z, Yang B, Xiao S, Yang G, Zhu T (2021) Fatigue crack growth behaviour of an Al-Mg4.5Mn alloy fabricated by hybrid in situ rolled wire + arc additive manufacturing. Int J Fatigue 151:106382. https://doi.org/10.1016/j.ijfatigue.2021.106382
163. Liu B, Zhou X, Hashimoto T, Zhang X, Wang J (2018) Machining introduced microstructure modification in aluminium alloys. J Alloys Compd 757:233–238. https://doi.org/10.1016/J.JALLCOM.2018.05.082
164. Hu Y, Lai M, Hu Z, Yao Z (2019) Effect of multiple laser peening on surface integrity and microstructure of laser additive manufactured Ti6Al4V titanium alloy. Rapid Prototyp J 25:1379–1387. https://doi.org/10.1108/RPJ-09-2018-0250
165. Jorge JCF, Souza LFGD, Mendes MC, Bott IS, Araújo LS, Santos VRD, Rebello JMA, Evans GM (2021) Microstructure characterization and its relationship with impact toughness of C-Mn and high strength low alloy steel weld metals – a review. J Mater Res Technol 10:471–501. https://doi.org/10.1016/J.JMRT.2020.12.006
166. Parvaresh B, Miresmaeili R, Yazdizadeh M (2020) Characterization of wire arc additive manufactured products: a comparison between as-deposited and inter-layer cold worked specimens. J Manuf Process 57:61–71. https://doi.org/10.1016/j.jmapro.2020.05.053
167. Fan XF, Zhou J, Qiu CJ, He B, Ye J, Yuan B, Pi Z (2011) Experimental study on surface characteristics of laser cladding layer regulated by high-frequency microforging. J Therm Spray Technol 20:456–464. https://doi.org/10.1007/s11666-010-9534-8
168. Coniglio N, Cross CE (2013) Initiation and growth mechanisms for weld solidification cracking. Int Mater Rev 58:375–397. https://doi.org/10.1179/1743280413Y.0000000020
169. Martina F, Williams SW, Colegrove P (2013) Improved microstructure and increased mechanical properties of additive manufacture produced TI-6AL-4V by interpass cold rolling, in: 24th Int. SFF Symp. - An Addit. Manuf. Conf., pp 490–496
170. Yang Y, Jin X, Liu C, Xiao M, Lu J, Fan H, Ma S (2018) Residual stress, mechanical properties, and grain morphology of Ti-6Al-4V alloy produced by ultrasonic impact treatment assisted wire and arc additive manufacturing. Metals (Basel) 8:934–943. https://doi.org/10.3390/met8110934
171. Chi J, Cai Z, Wan Z, Zhang H, Chen Z, Li L, Li Y, Peng P, Guo W (2020) Effects of heat treatment combined with laser shock peening on wire and arc additive manufactured Ti17 titanium alloy: microstructures, residual stress and mechanical properties. Surf Coatings Technol 396:125908. https://doi.org/10.1016/j.surfcoat.2020.125908

172. Huang S, Qi Z, Zhang A, Zhang X, Li Q, Li D (2022) Reducing the anisotropy of the mechanical properties of directed energy deposited Ti6Al4V alloy with inter-layer ultrasonic impact peening and heat treatment. Mater Sci Eng A 857:144123. https://doi.org/10.1016/J.MSEA.2022.144123
173. Hu Y, Ao N, Wu S, Yu Y, Zhang H, Qian W, Guo G, Zhang M, Wang G (2021) Influence of in situ micro-rolling on the improved strength and ductility of hybrid additively manufactured metals. Eng Fract Mech 253:107868. https://doi.org/10.1016/J.ENGFRACMECH.2021.107868
174. Wang F, Williams S, Rush M (2011) Morphology investigation on direct current pulsed gas tungsten arc welded additive layer manufactured Ti6Al4V alloy. Int J Adv Manuf Technol 57:597–603. https://doi.org/10.1007/S00170-011-3299-1
175. Bermingham MJ, Nicastro L, Kent D, Chen Y, Dargusch MS (2018) Optimising the mechanical properties of Ti-6Al-4V components produced by wire + arc additive manufacturing with post-process heat treatments. J Alloys Compd 753:247–255. https://doi.org/10.1016/J.JALLCOM.2018.04.158
176. Lütjering G (1998) Influence of processing on microstructure and mechanical properties of (α+β) titanium alloys. Mater Sci Eng A 243:32–45. https://doi.org/10.1016/S0921-5093(97)00778-8
177. Xiong X, Qin X, Hua L, Wan G, Hu Z, Ni M (2022) Microstructure evolution and parameters optimization of follow-up hammering-assisted hybrid wire arc additive manufacturing. J Manuf Process 84:681–696. https://doi.org/10.1016/J.JMAPRO.2022.10.031
178. Dornelas PHG, da Payão Filho JC, Farias FWC, Moraes e Oliveira VHP, de Moraes DO, Zumpano Júnior P (2020) FEM-thermodynamic simulation methodology to predict the influence of t8/5 on the coarse grain heat-affected zone of a Cr-Mo low-alloy steel pipe. J Manuf Process 60:520–529. https://doi.org/10.1016/J.JMAPRO.2020.10.082
179. Jia X, Yang Y, Ma Y, Wang B, Wang B (2022) Effect of different strains on acicular ferrite and martensite-austenite islands in oxide metallurgy steel. J Mater Res Technol 19:1777–1788. https://doi.org/10.1016/J.JMRT.2022.05.154
180. Wang C, Liu TG, Zhu P, Lu YH, Shoji T (2020) Study on microstructure and tensile properties of 316L stainless steel fabricated by CMT wire and arc additive manufacturing. Mater Sci Eng A 796:140006. https://doi.org/10.1016/J.MSEA.2020.140006
181. Kan X, Yang D, Zhao Z, Sun J (2021) 316L WAAM and pressure machining influence. Eng Res Express 3:045030. https://doi.org/10.1088/2631-8695/ac3849
182. Diao M, Guo C, Sun Q, Jiang F, Li L, Li J, Xu D, Liu C, Song H (2022) Improving mechanical properties of austenitic stainless steel by the grain refinement in wire and arc additive manufacturing assisted with ultrasonic impact treatment. Mater Sci Eng A 857:144044. https://doi.org/10.1016/J.MSEA.2022.144044
183. Xu X, Ganguly S, Ding J, Guo S, Williams S, Martina F (2018) Microstructural evolution and mechanical properties of maraging steel produced by wire + arc additive manufacture process. Mater Charact 143:152–162. https://doi.org/10.1016/J.MATCHAR.2017.12.002
184. Chen Q, Wang G, Zhang H, Li R (2022) Research on microstructure and mechanical properties of hybrid plasma arc and micro-rolling additive manufacturing of Inconel 718 superalloy. Rapid Prototyp J 28:1509–1519. https://doi.org/10.1108/rpj-09-2021-0227
185. Zhang T, Li H, Gong H, Wu Y, Ahmad AS, Chen X, Zhang X (2022) Comparative analysis of cold and warm rolling on tensile properties and microstructure of additive manufactured Inconel 718. Arch Civ Mech Eng 22:1–14. https://doi.org/10.1007/s43452-021-00356-7
186. Wang C, Li Y, Tian W, Hu J, Li B, Li P, Liao W (2022) Influence of ultrasonic impact treatment and working current on microstructure and mechanical properties of 2219 aluminium alloy wire arc additive manufacturing parts. J Mater Res Technol 21:781–797. https://doi.org/10.1016/J.JMRT.2022.09.055
187. Huang K, Marthinsen K, Zhao Q, Logé RE (2018) The double-edge effect of second-phase particles on the recrystallization behaviour and associated mechanical properties of metallic materials. Prog Mater Sci 92:284–359. https://doi.org/10.1016/J.PMATSCI.2017.10.004
188. Lloyd DJ (2006) The Work Hardening of some Commercial Al Alloys. Mater Sci Forum 519–521:55–62. https://doi.org/10.4028/WWW.SCIENTIFIC.NET/MSF.519-521.55
189. Martina F, Roy MJ, Szost BA, Terzi S, Colegrove PA, Williams SW, Withers PJ, Meyer J, Hofmann M (2016) Residual stress of as-deposited and rolled wire+arc additive manufacturing Ti–6Al–4V components. Mater Sci Technol 32:1439–1448. https://doi.org/10.1080/02670836.2016.1142704
190. Kleiman J, Kudryavtsev Y, Luhovskyi O (2017) Effectiveness of ultrasonic peening in fatigue improvement of welded elements and structures. Mech Adv Technol 3:92–98. https://doi.org/10.20535/2521-1943.2017.81.117489
191. Vázquez L, Rodríguez N, Rodríguez I, Alberdi E, Álvarez P (2020) Influence of interpass cooling conditions on microstructure and tensile properties of Ti-6Al-4V parts manufactured by WAAM. Weld World 64:1377–1388. https://doi.org/10.1007/s40194-020-00921-3
192. Wu D, Yu C, Wang Q, Niu F, Ma G, Wang H, Zhou C, Zhang B (2022) Synchronous-hammer-forging-assisted laser directed energy deposition additive manufacturing of high-performance 316L samples. J Mater Process Technol 307:117695. https://doi.org/10.1016/J.JMATPROTEC.2022.117695
193. Tan C, Li R, Su J, Du D, Du Y, Attard B, Chew Y, Zhang H, Lavernia EJ, Fautrelle Y, Teng J, Dong A (2023) Review on field assisted metal additive manufacturing. Int J Mach Tools Manuf 189:104032. https://doi.org/10.1016/j.ijmachtools.2023.104032
194. He Y, Liu J, Zhang S, Li Y, Gao X (2023) Effect of heat treatment on the microstructure and corrosion resistance of 316L stainless steel fabricated by hybrid in-situ rolled wire-arc additive manufacturing. Mater Lett 331:133398. https://doi.org/10.1016/J.MATLET.2022.133398
195. Chen C, Feng T, Sun G, Zhang H (2022) Microstructure and mechanical characteristics of 307Si stainless steel thin-wall parts in wire arc additive manufacturing hybrid interlayer high-speed friction. Manuf Lett 33:42–45. https://doi.org/10.1016/J.MFGLET.2022.07.009
196. Yu C, Zhao Y, Xu W, Dong C, Guo C, Deng J, Li Z, Miao S (2022) Trailing rotating-extrusion-assisted wire arc additive manufacturing of duplex stainless steel. Sci Technol Weld Join 27:629–637. https://doi.org/10.1080/13621718.2022.2105993
197. Kaufman JG (2000) Introduction to Aluminium Alloys and Tempers, 1st ed., ASM International. http://www.asminternational.org
198. Zhang C, Dong Y, Ye C (2021) Recent developments and novel applications of laser shock peening: a review. Adv Eng Mater 23:1–24. https://doi.org/10.1002/adem.202001216
199. Guo Y, Wang S, Liu W, Xiao T, Zhu G, Sun Z (2019) The effect of laser shock peening on the corrosion behavior of biocompatible magnesium alloy ZK60. Metals (Basel) 9:1–9. https://doi.org/10.3390/met9111237